UiO : Institute of Theoretical Astrophysics
University of Oslo

Space-based weak gravitational lensing measurements of lensing-selected clusters

Elisabeth Strøm

Master's Thesis, Spring 2019

Abstract

Weak gravitational lensing provides a way of estimating the mass and mass distribution of galaxy clusters at large radii. The clusters act as lenses, so that light emitted by background sources, is bent and distorted by the gravitational potential of the cluster. At large radii, the induced distortions in the image of the background galaxies, can be observed as a subtle systematic shift in their ellipticity. This is parametrized in the reduced gravitational shear, g. In this thesis, we perform a weak lensing analysis on three selected clusters, PSZ1 G311.65–18.48 (z=0.443), SDSS J1226+2152 (z=0.435), and SDSS J1723+3411 (z=0.443), all imaged by the Hubble Space Telescope. First, objects and their magnitudes are detected. Artifacts are filtered out by only allowing objects detected in multiple filters. By putting an upper an lower limit on their signal-to-noise ratio, and the sizes of the objects, stars and some cluster galaxies, are also rejected. Next, we remove the red sequence, formed by cluster galaxies in a color-magnitude diagram. Stars and are only affected by the point-spread-function (PSF) of the telescope optics, and most form a column in a magnitude versus radius diagram. They are used to determine the shape of the PSF. The final catalog, contains only background galaxies, and their PSF corrected reduced shear, is measured through a modified KSB method (Luppino and Kaiser 1997). The azimuthally averaged reduced shear, is found at different radii, and converted into a 2D surface mass distribution. We find that a NFW profile best fit our data, and obtain a mass estimate, M_{200}, through a best-fit analysis. The NFW profile depends on the parameters r_{200} and c_{200}, the latter of which is very difficult to determine. While keeping c_{200} fixed, and estimated from the relation found by Duffy et al. (2008), we report the following results: For PSZ1 G311.65–18.48, we find $\sigma_v \approx 1066.4\,\mathrm{km\,s^{-1}}$, and $M_{200} \approx 1.1 \times 10^{15}\,M_\odot h^{-1}$. This mass is about 1/2 of that extrapolated from Dahle et al. (2016), but well within our combined margins of error. For the SDSS clusters, we were only able to obtain an upper and lower limit of the mass. SDSS J1226+2152 is a part of a larger multi-cluster structure. This most likely biases our shear measurements to smaller values, and results in an unexpectedly small mass, $M_{200} \approx 2.1 \times 10^{13} M_\odot h^{-1}$. We suspect this is the same reason why our measured cluster galaxy velocity dispersion, $\sigma_v \approx 323.0\,\mathrm{km\,s^{-1}}$, is so much smaller than that found by Bayliss et al. (2011). For SDSS J1723+3411, we calculate a mass of $M_{200} \approx 4.5 \times 10^{14}\,M_\odot h^{-1}$, and a velocity dispersion of $\sigma_v = 518.9\mathrm{km\,s^{-1}}$. Compared to the strong lensing analysis done by Kubo et al. (2010) on the same cluster, our σ_v values are very similar. If we extrapolate their mass estimate with an SIS profile, our mass is ≈ 0.6 that of theirs.

Acknowledgments

I would like to thank my supervisor, Håkon Dahle, for providing me with such an interesting project. His guidance and patience has been very much needed, and appreciated. Also, a thanks to Øystein Elgarøy, for his good advice early on in my Masters' degree. I would also like to thank my family for their support, and my sister, Susanne, for her help in creating some figures, and for making the picture on the cover look so good. Lastly, I am grateful of the other students, here at the ITA, for being as welcoming an open as they are.

Contents

Abstract **3**

Acknowledgments **5**

List of Figures **8**

1 Introduction **13**
1.1 Thesis outline . . . 14
1.2 Historical background . . . 14
1.3 Cosmology . . . 17
1.3.1 Parameters . . . 18
1.4 Gravitational lensing basics . . . 20
1.4.1 Assumptions . . . 20
1.4.2 Deflection angle . . . 21
1.4.3 Lensing geometry . . . 22
1.4.4 Einstein radius . . . 24
1.4.5 Magnification and distortion . . . 25
1.4.6 Measurement . . . 26
1.5 Galaxy clusters . . . 27
1.5.1 Three clusters . . . 28

2 Method **33**
2.1 The Hubble Space Telescope . . . 33
2.1.1 Instruments . . . 34
2.1.2 Imaging three clusters . . . 35
2.1.3 AstroDrizzle . . . 36
2.2 Weak lensing theory . . . 38
2.2.1 The PSF . . . 39
2.3 Shear measurements . . . 40
2.3.1 Object ellipticities . . . 40
2.3.2 Shear estimates . . . 43
2.3.3 Distances . . . 45
2.3.4 Mass densitometry . . . 46
2.4 Weak lensing pipeline . . . 47

2.4.1 Image analysis 47
2.4.2 Detecting objects 48
2.4.3 Separating stars from galaxies 49
2.4.4 Removing the Red Sequence 50
2.4.5 Measuring shear and mass reconstruction 51
2.5 Fitting to density profiles 52
2.5.1 The Singular isothermal sphere 53
2.5.2 NFW density profile 55

3 Results and discussion **59**
3.1 Results 59
3.2 Discussion 70
3.2.1 Mass comparisons between models 72
3.2.2 Mass comparisons with earlier works 73
3.3 Future studies 73

4 Conclusion **75**

Bibliography **78**

List of Figures

1.1 A set-up of the lensing system. The source position is marked by S, the observed image at I, and the observer at O. The object acting as a lens is marked by the ellipse near the middle of the diagram. The optical axis runs through the lens, ending at O, and the two dimensional distance from the lens center, is marked by ξ. The angle between the optical axis and the unlensed source, is β, and θ is the angle between the optical axis and the image. α is the deflection angle, meaning the angle between the source and its image, while $\hat{\alpha}$ is the reduced deflection angle. The angular distances between the observer and the source, D_{S}, the observer and the lens, D_{l}, and the lens and the source, D_{ls}, have also been marked. This figure was made with the TikZ package (Tantau 2019). 23

1.2 A slightly cropped image of the field of PSZ1 G311.65–18.48. North is up, and east is to the left in the image. The image is in the F814W filter. The field of view here is $867'' \times 165''$, or $5900 \times 5500\,\mathrm{pix}^2$. 30

1.3 A cropped image of the field of SDSS J1226+2152. North is up, and east is to the left in the image. The image is in the F814W filter. The field of view here is $107'' \times 90''$, or $3300 \times 3000\,\mathrm{pix}^2$. 31

1.4 A cropped image of the field of SDSS J1723+3411. North is up, and east is to the left in the image. The image is in the infrared F110W filter. The field of view here is $94'' \times 69''$, or $2600 \times 2300\,\mathrm{pix}^2$. 32

2.1 Figure showing the basic idea behind drizzling. The input pixels are shrunken, then mapped onto a finer output grid. 37

2.2 e_1 versus e_2 plot of stars in the foreground of PSZ1 G311.65–18.48, in the F814W filter. The image to the left shows the stars prior to being corrected for the anisotropic PSF. The image to the right, shows the stars after the correction has been applied. We see that in the right-hand image, the stars are more centralized around the origin, but still with some scatter. The scatter is most likely due to the HST undersampling the stars, leading to uncertainty in the ellipticity measurements. 44

2.3 Close-up of the field of PSZ1 G311.65–18.48 in the F814W filter. The left-hand image shows all the initial object detections, marked in magenta. The image on the right shows the objects after we have performed `cleancat`. We see that there is now only one object per saturated star, and fewer objects on the strong lensing arc. `getshapes` have also been performed in the right image, meaning some objects, whose trace of the quadrupole moments were negative, have also been rejected. 49

2.4 A r_g versus magnitude diagram of objects detected in the field of PSZ1 G311.65–18.48. The stars in our star catalog are selected from the vertical column marked with a box in the diagram. The trailing tail of the column at low magnitudes and increasing radius, is caused by saturated stars 50

2.5 e_1 versus e_2 plot of stars in the foreground of PSZ1 G311.65–18.48, in the F814W filter. The image to the left shows our initial pick of stars from the star-column in Figure 2.4. In the figure to the right, we have excluded objects with a high ellipticity, which could be galaxies. 51

2.6 The objects detected in the field of SDSS J1226+2152 are plotted in a color magnitude diagram. We have an image in two filters, F606W (V) and F814W (I). On the x-axis we show the I magnitudes, on the y-axis, we have the subtracted magnitudes V-I. The cluster galaxies make up the red sequence, which is shown in the box. 52

3.1 Joint confidence interval for r_{200} and c_{200} for galaxy cluster PSZ1 G311.65-18.48 . First frame is for the F606W filter, while the second is for the F814W filter. The outermost contour marks values within 2σ ($\Delta\chi^2 = 6.14$), while the innermost marks values within 1σ ($\Delta\chi^2 = 2.30$).The best-fit values have been marked with a $\times$. 64

3.2 Joint confidence interval for r_{200} and c_{200} for galaxy cluster SDSS J1226+2152. First frame is for the F606W filter, while the second is for the F814W filter. Values within 2σ ($\Delta\chi^2 = 6.14$), lie below the topmost line, while the values within 1σ ($\Delta\chi^2 = 2.30$) lies below the lowest line. The other side of the contour then lies beneath the x-axis, at very low r_{200} values. The best-fit values have been marked with a $\times$. 65

3.3 Joint confidence interval for r_{200} and c_{200} for galaxy cluster SDSS J1723+3411. The filter is F775W. The outermost contour marks values within 2σ ($\Delta\chi^2 = 6.14$), while the innermost marks values within 1σ ($\Delta\chi^2 = 2.30$). The best-fit values have been marked with a $\times$. 66

3.4 The mean measured tangential shear, $\langle g_{\mathrm{T}} \rangle$ with errors for the two images in filters F606W and F814W for the cluster PSZ1 G311.65-18.48. On the x-axis is the mean radii of the annuli, r, in $h^{-1}Mpc$. Also shown are the best fit calculated mean tangential shear from the NFW profile and the SIS profile. We see that the fitted profiles fit well within the error bars of their respective images. With exception of the first point, the measured shear in both images fall within the range of each others errors, and the errors decrease as r increases. 67
3.5 The mean measured tangential shear, $\langle g_{\mathrm{T}} \rangle$ with error bars for the two images in filters F606W and F814W for the cluster SDSS J1226+2152. On the x-axis is the mean radii of the annuli, r, in $h^{-1}Mpc$. The calculated mean tangential shear according to the NFW profile and the SIS profile, is also shown. The fitted profiles fit well within the errors of the observed shear in both filters. The errors of the observed shear also overlaps, and grow smaller as r increases. 68
3.6 The mean measured tangential shear, $\langle g_{\mathrm{T}} \rangle$ with error bars for the cluster SDSS J1723+3411 in filter F775W. On the x-axis is the mean radii of the annuli, r, in $h^{-1}Mpc$. The calculated mean tangential shear according to the NFW profile and the SIS profile, is also shown. The fitted NFW profile, fits within the errors of the two final points, although not the first point. The SIS profile shear is not within any of the error bars, but lie close in the two final points. This is reflected in Table 3.2, where the χ^2_{min}-value for both profiles, is quite high. The errors of the observed shear grow smaller as r increases. 69

Chapter 1

Introduction

A hundred years ago, on May 29th 1919, the Moon passed in front of the Sun, darkening the sky for 6 minutes and 51 seconds, at the longest. It was the second longest eclipse since 1416. A total solar eclipse could be seen in a narrow band stretching from southern Peru in South America, to northern Portuguese Mozambique (Mozambique) in Africa (Espenak and Meeus 2006).

In Sobral, Brazil and on the island of Principe, off of the African west coast, scientists led by Sir Frank Watson Dyson and Sir Arthur Eddington, had assembled to observe the stars that would be made visible during the total eclipse.

Their goal was to measure the position of the stars near the Sun's limb, in order to verify or falsify Albert Einstein's newly proposed theory of general relativity. What they found, was that the stars seen near the Sun, appeared to have a different position compared to observations of the very same stars taken at night. What they had observed during the eclipse, was the bending of the light of the stars, by the gravitational field of the Sun, making them appear to be elsewhere (Dyson et al. 1920).

This was not unexpected, as it had already been predicted by Sir Isaac Newtons theory of gravity (Jaki 1978; Cavendish 1921). However, calculations done on the displacement of the stars using this theory, was off by a factor of two compared to what was observed by the 1919 expeditions (Dyson et al. 1920). Using Einstein's general theory of relativity, however, the correct value was obtained, and Einstein became famous overnight.

This is the oldest experimental test of the general theory of relativity, and it has been repeated many times since then. It took advantage of a phenomenon known as *gravitational lensing*, which is when a massive object change the path of light that is passing it by. And while used to verify one theory, it would take quite some time before gravitational lensing in itself became a popular and useful area of study in astrophysics. An article by Einstein in 1936 (Einstein 1936) has been considered the beginning of the field. There, he put down the equations describing gravitational lensing done by stars. Not a year later, Fritz Zwicky (Zwicky 1937a,b) proposed galaxies as a place to look for the phenomenon, both as a lens, and as the lensed object.

The discovery of quasars in the 1960s, eventually led to the discovery of the first

gravitational lens system, that of the twin quasars QSO 0957+561 A and B. This turned out to be only *one* quasar, lensed twice (Walsh et al. 1979) by a foreground galaxy. The advent of CCD cameras and better telescopes, such as the Hubble space telescope and the Very Large Array, made this and further discoveries possible. Giant luminous arcs produced by lensing done by galaxy clusters was found in 1986 (Lynds and Petrosian 1989; Soucail et al. 1987), and marked the discovery of the *strong lensing* regime. In contrast, the more subtle *weak gravitational lensing* effect was first detected around galaxy clusters in 1990 (Tyson et al. 1990).

Gravitational lensing has many uses, from acting as natural telescopes, determining the mass and mass distribution of the lenses, to providing insight into the growth of structures, and putting constraints on cosmological parameters. It is today an area of active research with several thousand papers being written each year (Web of Science 2018), and with many further studies sure to come in the future.

1.1 Thesis outline

In this thesis, we will obtain an estimate of the mass of three separate galaxy clusters. They are PSZ1 G311.65–18.48, SDSS J1723+3411, and SDSS J1226+2152. The mass estimate will be derived from studying the mass distribution of the clusters through the weak gravitational lensing effect, and fitting the observational data to mass density profiles.

In this chapter we go through the historical narrative behind the gravitational lensing subject. Then we give a short introduction to cosmology and the basic equations behind gravitational lensing. Lastly we have some properties of cluster lenses, and in particular about the three clusters that are the subjects of study in this thesis.

In Chapter 2 we go through the methods we use to perform a weak lensing analysis. This includes a brief description of the telescope and instruments used to obtain the images of the lens systems, along with how the images have been processed prior to our own analysis. We describe how we distinguish stars and cluster and source galaxies, and how we perform point-spread function (PSF) corrections. Lastly we show how we obtain a mass estimate of the cluster lenses, and how we fit our observational data to two different density profiles.

In chapter 3 we show the results of our weak lensing analysis. They are then discussed and compared with previous lensing studies done on these clusters. We also provide a short summary.

1.2 Historical background

The first calculations on gravitational lensing are often attributed to Johann Soldner (translation by Jaki (1978)) and Henry Cavendish (Cavendish 1921) in the early eighteen-hundreds (Valls-Gabaud 2006). Seemingly independent of one another, they were able to correctly analytically calculate the apparent displacement of the stars close to the Sun, assuming Newtonian gravity. Einstein would arrive at the same value in

1911 (Einstein 1993). Meanwhile, Einstein would calculate the *actual* correct value, using his own theory, in an unpublished notebook in 1912 (Sauer 2008).

Following the 1919 solar eclipse, and the subsequent release of the obtained results (Dyson et al. 1920), Eddington speculated that the lensing effect could give rise to fake double stars (Eddington 1921). However, he believed that the observed effect would be very small, and not possible to detect with the telescopes of their time. A few year later, Orest Chwolson would be the first to describe what he called the "halo" effect of gravitation: a perfect ring of deflected light formed by a gravitational lens, should the lens, the light source, and the observer be colinear (Chwolson 1924). We know this today as an *Einstein ring*. He too agreed that fake double stars could be a product of the lensing effect.

Despite these early queries, it would go over a decade before what has often been considered the pioneering study of gravitational lensing, was published. It was a short note in *Science*, written, quite reluctantly, by Einstein (1936). There, he presented the formulae for the optical properties of a gravitational lens, the same formulae he had written in his notebook in 1912 (Renn et al. 1997). Seeing as Einstein was only considering the lensing of individual stars, he concluded, like Eddington, that the phenomenon would be to small too be observed. This pessimistic outlook would rule this branch of astronomy right up until the 1980s. Still, some notable papers were being written every other decade or so.

Following Einsteins 1936 paper in *Science*, Fritz Zwicky suggested that the recently discovered extragalactic "nebulae" (now known as galaxies) would be better candidates as both light sources to be lensed, and as the lens itself (Zwicky 1937a). This was due to their high apparent mass, and their distance from us. He stated the probability of finding galaxies that act as lenses to be "practically a certainty" (Zwicky 1937b). He also predicted the several uses gravitational lensing could have: That it could serve as another test for the general theory of relativity; it could make galaxies, at even greater distances than what a telescope could normally see, visible; and the deflected light could aid in deciding the mass of the galaxies and galaxy clusters acting as lenses (Zwicky 1937a). In the time since Zwicky's papers, gravitational lenses has been used for all of these purposes.

It would, once again, go quite a few years before the next milestone was reached. Interest was reawakened by a number of papers written independently in 1963-64 by Yu G. Klimov (Klimov 1963), Sidney Liebes Jr. (Liebes 1964), and Sjur Refsdal (Refsdal 1964a,b). While Klimov wrote of galaxies lensing galaxies, Liebes wrote on the possibility that stars in the Milky Way could act as lenses for stars in the Andromeda galaxy M31. Refsdal, meanwhile, calculated how to use gravitationally lensed supernovae or the newly discovered quasars, to determine the mass of the lens and the value of the Hubble constant, based on the separation and time delay between lensed images.

Another 15 years, and the first extragalactic gravitational lens system had been found. In 1979, Dennis Walsh, Robert F. Carswell and Ray J. Weymann found two quasars, QSO 0957+561 A and B, lying close together, having a separation of 6 arcseconds. While unusual in itself, what was even more strange was that they appeared to have the same redshift, $z = 1.41$, and that their optical spectra were almost identical.

This led them to suspect that they were in fact only looking at *one* quasar that had been gravitationally lensed by a massive object lying along the line-of-sight, in between the quasars and the astronomers (Walsh et al. 1979). This object was later determined to be the giant elliptical galaxy YGKOW G1, lying at redshift $z = 0.39$, which belong to a small cluster of galaxies that also contribute to the lensing (Young et al. 1980; Stockton 1980).

Technology is continuously evolving, but the year 1979 was a special one in astronomy. In this year the first CCD detectors replaced photographic plates, and the Very Large Array (VLA), went into operation. These technologies made the double quasar discovery possible (Schneider 2006). CCD detectors are much more sensitive to light than traditional photographic film, having a quantum efficiency (QE) of $50\,\% - 90\,\%$ and below 5%, respectively. They also have better dynamic range and linearity (Tabbert and Goushcha 2012; Tozer 2012). CCD cameras were used to detect the foreground galaxy YGKOW G1 and its cluster acting as a lens. Meanwhile, observations using the VLA allowed for subarcsecond radio imaging, which confirmed that the double quasars where radio sources, and that both images displayed similar radio characteristics (Greenfield et al. 1980a,b).

All in all, it had gone 60 years since the 1919 eclipse, when the bending of light due to a massive body was first observed, until the first extragalactic gravitational lens was found. A number of other discoveries have since followed, such as the triple quasar PG 1115+080 (Weymann et al. 1980), the Einstein cross QSO 2237+0305 (Huchra et al. 1985), and the Einstein ring MG1131+0456 (Hewitt et al. 1988).

Giant luminous arcs where discovered in 1986 independently by Lynds and Petrosian (1989) and Soucail et al. (1987). These are the strongly elongated images of background galaxies lensed by the centers of massive clusters (Paczynski 1987). This was the discovery of what is called the strong lensing regime in galaxy clusters, and can be viewed as the beginning of studying gravitational lensing done by so called "cluster lenses". The Hubble space telescope (HST) was essential in the studying of the arcs in detail, and recognizing multiple images (Schneider 2006). One of the first images released from the refurbished Hubble after its first servicing mission, was that of the cluster lens Abell 2218 (Kneib et al. 1996).

While strong lensing can produce large, obvious arcs, weak lensing will instead introduce a subtle change in the shape of background galaxies, called *arclets*, causing a systematic alignment of galaxies at large radii, around the cluster core. The weak gravitational lensing effect was first detected by Tyson et al. (1990). This effect is often very small, thus hard to detect, so special statistical methods are used. Throughout the 1990's, the development of wide field imaging cameras, larger and better telescopes, not to mention the Hubble Space Telescope (HST), had made it easier to study gravitational lensing done by clusters, and it is today an active field of research (Kneib and Natarajan 2011; Hoekstra et al. 2013). The study of gravitational lensing done by the large-scale-structure in the universe, called the cosmic shear, was also made possible by these technologies. On to something smaller, we can also detect a gravitational lensing effect should a distant star pass directly behind a closer massive object, like a star or a star with an orbiting planet (Alcock et al. 1993). Several such so-called microlensing events

have been observed, and they have become a way of detecting exoplanets (e.g, Udalski et al. (2005)).

Like Zwicky predicted in 1937, gravitational lensing has been used to determine the mass of clusters and individual galaxies, and also to derive the density profile of dark matter at different radii. Through comparisons with simulations, this can tell us something about how clusters are formed (Hoekstra et al. 2013; Kneib and Natarajan 2011). The lensed objects have also been studied, using the lenses as natural telescopes, and thus increasing our knowledge of distant galaxies. Gravitational lensing has also been used to constrain cosmological parameters, such as the Hubble constant following Refsdal's idea, and the matter density parameter. Future studies of weak lensing done by the cosmic shear, and strong lensing done by clusters, could serve as a probe of the equation of state for dark energy (Kneib and Natarajan 2011; Schneider 2006).

This is only a brief introduction to the historical narrative of gravitational lensing. We will now continue into the more formal aspect on things, and lay down some fundamental equations.

1.3 Cosmology

The validity of the *cosmological principle* is one of the most fundamental assumptions made in cosmology. It states that, at large scales, the spatial distribution of matter in the universe is both homogeneous and isotropic. This means that wherever an observer finds themselves in the universe, and in whatever direction they observe; on large enough scales, it will all look the same. By not making our own position in the universe special, we can use observations made locally to build a model of the universe that is valid throughout the entirety of it.

Numerous such universe models exist, some describing certain epochs more accurately than others. A *metric tensor* can be defined, which characterizes the geometry of spacetime in a specific universe model. The metric then explains the way distances in spacetime should be measured in any direction.

One of the first to discover the expansion of space was Edwin Hubble (Hubble 1929). He observed that distant galaxies are moving away from us according to the relation $v = Hr$, where v is a galaxy's recessional velocity, H the *Hubble parameter*, and r its distance from us. The expansion of space is parametrized by the *scale factor* $a(t)$. It is normalized so that today, $a(t_0) = a_0 = 1$.

In the case of an isotropic and homogeneous universe, the spacetime can be described by the Friedmann–Lemaître–Robertson–Walker (FLRW) metric,

$$\mathrm{d}s^2 = -c^2\,\mathrm{d}t^2 + a(t)^2\left(\frac{\mathrm{d}r^2}{1-kr^2} + r^2\,\mathrm{d}\mathbf{\Omega}^2\right) \tag{1.1}$$

where

$$\mathrm{d}\mathbf{\Omega}^2 = \mathrm{d}\theta^2 + \sin^2\theta\,\mathrm{d}\phi^2. \tag{1.2}$$

Here, $\mathrm{d}s$ is the interval between two events in spacetime, $\mathrm{d}t$ is the coordinate time, c is the speed of light, $a(t)$ is the scale factor, r is the comoving radial coordinate, and θ

and ϕ is the azimuthal angle and the polar angle, respectively, on a unit sphere.

Another metric is the Minkowski metric of flat spacetime,

$$\mathrm{d}s^2 = -c^2\mathrm{d}t^2 + \mathrm{d}x^2 + \mathrm{d}y^2 + \mathrm{d}z^2, \tag{1.3}$$

where x, y, z are the 3-dimensional Cartesian coordinates. We will assume that around our gravitational lenses, the local space is described by the Minkowski metric perturbed by a dimensionless Newtonian potential, Φ/c^2, which approaches zero at infinity. The perturbed Minkowski metric is given by

$$\mathrm{d}s^2 = -c^2\left(1 + \frac{2\Phi}{c^2}\right)\mathrm{d}t^2 + \left(1 - \frac{2\Phi}{c^2}\right)(\mathrm{d}x^2 + \mathrm{d}y^2 + \mathrm{d}z^2). \tag{1.4}$$

Due to the expansion of space, photons will be redshifted as they move from their source towards the observer. This relative change in wavelength is called the *redshift*, z. It is related to the scale factor through

$$1 + z = \frac{a(t_\mathrm{o})}{a(t_\mathrm{e})}, \tag{1.5}$$

where t_e is the time the photons where emitted, and t_o is when they where observed. If we count our selves as the observers, $1 + z = 1/a(t)$.

We model the matter content of the universe as a homogeneous perfect fluid with density $\rho(t)$ and pressure $p(t)$. The density and the pressure are related through the equation of state

$$\rho(t) = wp(t)c^2, \tag{1.6}$$

where w is a constant depending on the species of matter (i.e, dust, radiation etc.).

When inserting the FLRW metric into the Einstein field equations from General relativity, and modelling matter as a perfect fluid, they simplify to the two independent Friedmann equations,

$$\left(\frac{\dot{a}}{a}\right)^2 = \frac{8\pi G}{3}\rho - \frac{kc^2}{a^2} + \frac{\Lambda}{3}, \tag{1.7}$$

$$\frac{\ddot{a}}{a} = -\frac{4}{3}\pi G\left(\rho + \frac{3p}{c^2}\right) + \frac{\Lambda}{3}, \tag{1.8}$$

where Λ is the cosmological constant, k is the curvature parameter, and G is the gravitational constant. The field equations relate local spacetime curvature with the local energy and momentum within spacetime. Meanwhile, the Friedmann equations relate the evolution of the scale factor to the energy and pressure of the matter content in the universe.

1.3.1 Parameters

The relative expansion rate of space is parametrized by the Hubble parameter

$$H \equiv \frac{\dot{a}}{a}, \tag{1.9}$$

where a dot, $\dot{}$, denotes a derivative with with respect to time, t. The *Hubble constant* is the value of the Hubble parameter today, $H(t_0) = H_0$, and is the current rate of expansion. The exact value of H_0 has proven difficult to determine, hence it is often written as

$$H_0 = 100\,h\,\mathrm{km\,s^{-1}\,Mpc^{-1}}, \tag{1.10}$$

with h as a dimensionless number measured to be in the range 0.6-0.8.

The *critical density* is the average density of the universe, ρ, when the universe is flat ($k = 0$). A universe with this average density will halt its expansion after an infinite time. It is defined as

$$\rho_{\mathrm{crit}}(t) = \frac{3H(t)^2}{8\pi G}. \tag{1.11}$$

If the universe has an average density larger than ρ_{crit}, then $k = 1$, and the universe's expansion will slow down until it halts, then it will collapse. If the average density is less than ρ_{crit}, $k = -1$, and the universe will expand forever.

We commonly measure densities in terms of the critical density, and define the density parameter,

$$\Omega = \frac{\rho}{\rho_{\mathrm{crit}}}, \tag{1.12}$$

where its value today at t_0, is $\Omega_0 = \rho_0/\rho_{\mathrm{crit}}$. Matter, radiation, and dark energy, contribute to the total density parameter of the universe,

$$\Omega_{\mathrm{tot}} = \Omega_{\mathrm{m}} + \Omega_{\mathrm{r}} + \Omega_\Lambda = 1 - \Omega_{\mathrm{k}}. \tag{1.13}$$

These are all time dependent quantities. Here, Ω_{m} is the matter (dark and baryonic) density, Ω_{r} is the radiation density, Ω_Λ is the vacuum density or the cosmological constant, and Ω_{k} is the spatial curvature density,

$$\Omega_{\mathrm{r}} = \frac{\rho_{\mathrm{r0}}}{\rho_{\mathrm{crit}}}a^{-4}; \quad \Omega_{\mathrm{m}} = \frac{\rho_{\mathrm{m0}}}{\rho_{\mathrm{crit}}}a^{-3}; \quad \Omega_\Lambda = \frac{\rho_\Lambda}{\rho_{\mathrm{crit}}} = \frac{\Lambda}{3H^2}; \tag{1.14}$$

$$\Omega_{\mathrm{k}} = -\frac{kc^2}{a^2H^2} = 1 - \Omega_{\mathrm{r}} - \Omega_{\mathrm{m}} - \Omega_\Lambda, \tag{1.15}$$

where a subscript 0 denotes their values of today, $t = t_0$.

We can rewrite the first Friedmann equation in terms of the Hubble parameter and the density parameters,

$$\frac{H^2}{H_0^2} = \Omega_{0,\mathrm{r}}a^{-4} + \Omega_{0,\mathrm{m}}a^{-3} + \Omega_{0,\mathrm{k}}a^{-2} + \Omega_{0,\Lambda}. \tag{1.16}$$

Where necessary, we will be using the flat ΛCDM universe model, where the dark matter is cold dark matter (CDM), spatial curvature is flat, and the density contribution of radiation can be ignored, $\Omega_{\mathrm{k}} = \Omega_{\mathrm{r}} = 0$. The vacuum density can then be written as $\Omega_\Lambda = 1 - \Omega_{\mathrm{m}}$, and the total density sums to 1, $\Omega_{\mathrm{tot}} = \Omega_\Lambda + \Omega_{\mathrm{m}} = 1$. Here, $\Omega_{0,\mathrm{m}} = 0.3$, and $\Omega_{\Lambda,0} = 0.7$ and $h = 0.7$.

1.4 Gravitational lensing basics

Here we go through some of the basic principles behind gravitational lensing. Some of this will be expanded upon in Chapter 2. Much of this material was found in Bartelmann and Maturi (2017), Narayan and Bartelmann (1996), Hoekstra et al. (2013), and Schneider (2006).

Gravitational lensing is a phenomenon that occurs when a massive foreground object acts as a lens, distorting the light emitted by more distant objects, that traverse through the lens's gravitational field. Stars, galaxies, galaxy clusters, or the large-scale structure of galaxy filaments, can all act as lenses. What the visual effect of this is, varies greatly. It depends on the relative positions between the object acting as a lens, or deflector, and the object being lensed, and the mass and mass distribution of the deflector. This distortion is a purely geometric effect, and occurs regardless of wavelength.

In the case of strong lensing, we may observe multiple images of a single source galaxy, or large, bright arcs.

For the more subtle weak lensing, we might find it difficult to see any difference at all without doing a statistical analysis. What we then tend to find, is a systematic distortion of the shape of the background sources, caused by the gravitational tidal field at large radii.

One benefit of gravitational lensing, is that it is independent of the luminosity and composition of the lens, or its dynamical state, depending only on the projected two-dimensional mass distribution of the lens, and geometrical properties such as the source and lens position (Narayan and Bartelmann 1996). It therefore offers an ideal way of studying dark matter, independent of its nature.

1.4.1 Assumptions

First we lay down some of the base assumptions that we make:

- The overall geometry of the universe is described by the FLRW metric (Equation 1.1), which assumes that space is homogeneous and isotropic. Next we assume that the inhomogeneities which cause gravitational lensing, are only local perturbations (Narayan and Bartelmann 1996).

- Close to the lens, we assume an observer co-moving with the gravitational lens, to have a locally flat Minkowskian space-time which is weakly perturbed by the Newtonian gravitational potential of the lens, Φ. This is a valid assumption if we have a weak gravitational field, $|\Phi| \ll c^2$, and if the peculiar velocity of the lens, v is small, $v \ll c$. In practically all cases of astrophysical interest, these conditions are met (Narayan and Bartelmann 1996; Bartelmann and Maturi 2017).

- We assume that the deflection angles of the lensed images are small, and that the extent of the lens along the line-of-sight is much smaller compared to the distance between the observer and the lens, and the lens and the source. The lens can then be considered thin, compared to the full length of the light path. Most deflection

angles in weak lensing, are also on the order of arcseconds or smaller. This is also expected if we assume $|\Phi|/c^2 \ll 1$ (Narayan and Bartelmann 1996; Bartelmann and Maturi 2017).

- The effects of diffraction are negligible (Deguchi and Watson 1986).

Now we will be able to make some approximations that can be more readily worked with.

1.4.2 Deflection angle

The gravitational field of the lens will alter the course of light passing trough it, affecting both the speed and direction of the photons. This is similar to what happens when light passes through a prism. But unlike a prism, where the degree of distortion depends on wavelength, in a gravitational lens all light is bent by the same degree, regardless of wavelength.

We can similarly say that the gravitational potential has an effective index of refraction(Narayan and Bartelmann 1996),

$$n = \frac{c}{c'} \approx 1 - \frac{2\Phi}{c^2}. \tag{1.17}$$

where $c' \approx c\left(1 + \frac{2\Phi}{c^2}\right)$ is the effective speed of light in the gravitational field. As $n > 1$, the the effective speed of light is reduced in the gravitational field. This means that light rays propagating through the field will be delayed relative to light rays propagating outside it.

The total time delay is called Shapiro delay (Shapiro 1964), or gravitational time delay, and is caused by spacetime dilation,

$$\Delta t = \int_{\text{source}}^{\text{observer}} \frac{2}{c^2}|\Phi|\,\mathrm{d}l, \tag{1.18}$$

which is an integral over the light path from the observer to the source.

The change in direction experienced by photons in the the gravitational field, is found by applying Fermat's principle. It states that light follows the path between two points A and B along which its optical path is extremal (Bartelmann and Maturi 2017). This leads to the angle of deflection (Narayan and Bartelmann 1996),

$$\hat{\boldsymbol{\alpha}} = \frac{2}{c^2}\int \boldsymbol{\nabla}_\perp \Phi\,\mathrm{d}l. = -\int \boldsymbol{\nabla}_\perp n\,\mathrm{d}l, \tag{1.19}$$

which is the gradient of n, or the dimension-less Newtonian potential multiplied with 2, perpendicular to the light ray integrated along its path. This integral can be difficult to calculate, but as we assume $\hat{\boldsymbol{\alpha}}$ to be small (usually a few arcseconds or less), the integration path is approximately straight.

As a first approximation to a gravitational lens, let us assume we have a point mass M at the center of the coordinate system with gravitational potential

$$\Phi(b, z) = -\frac{GM}{(b^2 + z^2)^{1/2}}, \tag{1.20}$$

where G is the gravitational constant, z is the distance parallel to the z-axis, and b is the impact parameter of the unperturbed light ray. The impact parameter is the distance between the point mass M and the unperturbed light ray.

The deflection angle of a passing ray of light, then becomes

$$\hat{\alpha} = \frac{4GM}{c^2 b} = \frac{2R_\mathrm{s}}{b}, \tag{1.21}$$

where $R_\mathrm{s} = 2GM/c^2$ is the Schwarzschild radius of the point mass.

1.4.3 Lensing geometry

One of our base assumptions was that the angular separation between the lens and the source is small. We therefore use the small angle approximation,

$$\sin\theta \approx \theta \quad \text{and} \quad \cos\theta \approx 1. \tag{1.22}$$

We also assumed that the lensing mass distribution is thin compared to the overall extension of the light path. We can then use the *thin screen approximation*, which is analogous to the *thin lens approximation* in optics.

In the thin screen approximation, instead of considering the three-dimensional mass distribution of the gravitational lens, $\rho(\xi, z)$, we use the mass distribution projected along the line-of-sight. The mass is then contained in a sheet which lies in a plane orthogonal to the line-of-sight. This sheet is called the *lens plane*, and is characterized by its surface mass density,

$$\Sigma(\boldsymbol{\xi}) = \int \rho(\boldsymbol{\xi}, z)\,\mathrm{d}z, \tag{1.23}$$

where $\boldsymbol{\xi}$ is a 2-dimensional vector in the lens plane. Likewise, we speak of the *source plane*, where the source is, and the *observer plane*.

As long as the thin screen approximation holds, the deflection angle $\hat{\alpha}$ can be found by summing the contributions of all mass elements $M_i = \Sigma(\boldsymbol{\xi})\,\mathrm{d}^2\xi$,

$$\hat{\boldsymbol{\alpha}} = \frac{4G}{c^2} \int \frac{(\boldsymbol{\xi} - \boldsymbol{\xi'})}{|\boldsymbol{\xi} - \boldsymbol{\xi'}|^2} \Sigma(\boldsymbol{\xi})\,\mathrm{d}^2\xi'. \tag{1.24}$$

In the case of an axially symmetric lens, we have that

$$\hat{\boldsymbol{\alpha}}(\boldsymbol{\xi}) = \frac{4GM(\xi)}{c^2} \frac{\boldsymbol{\xi}}{|\boldsymbol{\xi}|^2}, \tag{1.25}$$

where $M(\xi) = 2\pi \int_0^\xi \Sigma(\xi')\xi'\,\mathrm{d}\xi'$ is the mass enclosed within radius $\xi = |\boldsymbol{\xi}|$.

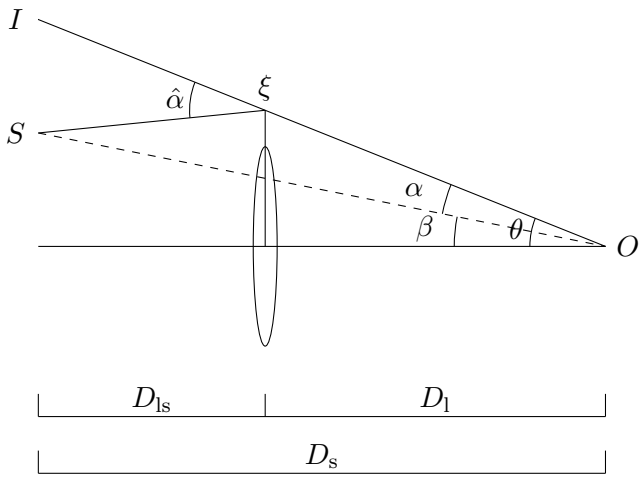

Figure 1.1: A set-up of the lensing system. The source position is marked by S, the observed image at I, and the observer at O. The object acting as a lens is marked by the ellipse near the middle of the diagram. The optical axis runs through the lens, ending at O, and the two dimensional distance from the lens center, is marked by ξ. The angle between the optical axis and the unlensed source, is β, and θ is the angle between the optical axis and the image. α is the deflection angle, meaning the angle between the source and its image, while $\hat{\alpha}$ is the reduced deflection angle. The angular distances between the observer and the source, $D_{\rm S}$, the observer and the lens, $D_{\rm l}$, and the lens and the source, $D_{\rm ls}$, have also been marked. This figure was made with the Ti*k*Z package (Tantau 2019).

When using the thin screen approximation, the light-path from the observer to the source can be approximated by straight lines, as long as we are looking at isolated structures, like galaxy clusters. A diagram of the gravitational-lens system can be seen in Figure 1.1.

The solid line is the actual path of the light coming from the source at S, reaching the observer at O. The image, at I, is where the source appears to be as seen from O, due to the deflection of the light rays done by the gravitational lens. The optical axis runs from the observer, and through the lens. As seen by the observer, the angle between the optical axis and the source is $\boldsymbol{\beta}$, and the optical axis and the image, is $\boldsymbol{\theta}$. The distances between the observer and the lens, the observer and the source, and the lens and the source, are $D_{\rm l}$, $D_{\rm s}$, and $D_{\rm ls}$, respectively. Clearly, the lensing signal depends on the redshift of both the source, and the lens. These distances are *angular diameter distances*, meaning that the relation,

$$D_{\rm s}\boldsymbol{\theta} = \boldsymbol{\beta} D_{\rm s} + \hat{\boldsymbol{\alpha}} D_{\rm ls}, \tag{1.26}$$

which is found from Figure 1.1, is valid even if space-time is not flat. In general, $D_{\rm ls} \neq D_{\rm s} + D_{\rm l}$.

From Equation 1.26, we find the *lens equation*,

$$\boldsymbol{\beta} = \boldsymbol{\theta} - \boldsymbol{\alpha}, \tag{1.27}$$

where we have introduced the *reduced deflection angle* $\boldsymbol{\alpha}$,

$$\boldsymbol{\alpha} = \frac{D_{\rm ls}}{D_{\rm s}}\hat{\boldsymbol{\alpha}}. \tag{1.28}$$

The lens equation is in general non-linear, meaning multiple images can correspond to a single source, as is the case in strong lensing.

Next we introduce the lensing potential, also called the deflection potential, which we will see, incorporates all imaging properties of a gravitational lens. The lensing potential is a two-dimensional scalar potential, which is the scaled, projected Newtonian potential of the lens,

$$\psi(\boldsymbol{\theta}) = \frac{2}{c^2}\frac{D_{\rm ls}}{D_{\rm l}D_{\rm s}}\int \Phi(D_{\rm l}\boldsymbol{\theta}, z)\,{\rm d}z. \tag{1.29}$$

Here we used that $\boldsymbol{\xi} = D_{\rm l}\boldsymbol{\theta}$. We see from this equation that the derivative of ψ with respect to the angular position $\boldsymbol{\theta}$, is the reduced deflection angle,

$$\alpha = \boldsymbol{\nabla}_\theta \psi \tag{1.30}$$

where $\boldsymbol{\nabla}_\theta = D_{\rm l}\boldsymbol{\nabla}_\perp$.

For a point mass lens, the deflection angle and lens potential becomes

$$\alpha = \frac{\partial\psi}{\partial\theta}, \quad \text{and} \quad \psi = \frac{4GM}{c^2}\frac{D_{\rm ls}}{D_{\rm l}D_{\rm s}}\ln|\theta|. \tag{1.31}$$

1.4.4 Einstein radius

Multiple images are frequently seen when background sources are viewed via a region of the lens that have a mass density equal to or larger than the *critical surface mass density*, defined as

$$\Sigma_{\rm crit} = \frac{c^2}{4\pi G}\frac{D_{\rm s}}{D_{\rm l}D_{\rm ls}}. \tag{1.32}$$

We say that a lens region is supercritical if $\Sigma > \Sigma_{\rm crit}$.

In the case of a single point mass lens, the lens equation (Equation 1.27) can be rewritten as

$$\beta = \theta - \frac{D_{\rm ls}}{D_{\rm l}D_{\rm s}}\frac{4GM}{c^2\theta}. \tag{1.33}$$

In the special case where a source lies directly behind such a lens, i.e it lies exactly on the optical axis, then $\beta = 0$, and the resulting image will be a ring if the lens is supercritical. This is called an Einstein ring, and its radius is known as the *Einstein radius*, $\theta_{\rm E}$. We can calculate it to be

$$\theta_{\rm E} = \left[\frac{4GM}{c^2}\frac{D_{\rm ls}}{D_{\rm l}D_{\rm s}}\right]^{1/2}. \tag{1.34}$$

We can see from Equations 1.32 and 1.34, that within the Einstein radius, the mean mass density is equal to the critical mass density $\Sigma_{\rm crit}$.

The Einstein radius is an important quantity. When multiple imaging occurs, the typical angular separation of the images is on the order of $2\theta_{\mathrm{E}}$. Sources that lie closer to the optical axis than θ_{E}, will experience strong lensing, while sources located well outside this radius, are not as strongly magnified. In this way, it establishes a rough boundary between sources that will be multiple- and singly-imaged (In general, $\Sigma > \Sigma_{\mathrm{crit}}$ is a sufficient condition for a source to be multiple-imaged, but it is not always a necessary one).

1.4.5 Magnification and distortion

What gravitational lensing essentially is, is a mapping from the source plane to the image plane.

The relation between the source and its image can be locally lineralized given that the source is much smaller than the scale on which the lens properties change(Schneider 2006). This case is what is referred to as weak gravitational lensing. The distortions in the image is described by the Jacobian matrix, also called the distortion matrix, of the lens mapping, $\mathcal{A}$, which has the components

$$\mathcal{A}_{ij} = \frac{\partial \beta_i(\boldsymbol{\theta})}{\partial \theta_j} = \delta_{ij} - \frac{\partial \alpha_i(\boldsymbol{\theta})}{\partial \theta_j} = \delta_{ij} - \psi_{,ij}, \tag{1.35}$$

where δ_{ij} is the Kronecker delta, and where

$$\psi_{,ij} = \frac{\partial^2 \psi(\boldsymbol{\theta})}{\partial \theta_i \partial \theta_j}, \tag{1.36}$$

are the potential derivatives, computed at the center of the lensed image.

During gravitational lensing, the surface brightness is conserved, according to Liouville's theorem from general relativity[1]. Hence, if a source has the surface brightness $f^{\mathrm{s}}(\boldsymbol{\beta})$ in the source plane, the observed surface brightness in the lens plane, is

$$f^{\mathrm{obs}}(\boldsymbol{\theta}) = f^{\mathrm{s}}[\boldsymbol{\beta}(\boldsymbol{\theta})]. \tag{1.37}$$

Written as a remapping of the surface brightness, we get

$$f^{\mathrm{obs}}(\theta_i) = f^{\mathrm{s}}(\mathcal{A}_{ij}\theta_j). \tag{1.38}$$

The Jacobi matrix can also be written in terms of the *convergence*, κ, and the *shear* γ or *reduced shear*, g,

$$\mathcal{A} = \begin{pmatrix} 1-\kappa-\gamma_1 & -\gamma_2 \\ -\gamma_2 & 1-\kappa+\gamma_1 \end{pmatrix} = (1-\kappa)\begin{pmatrix} 1-g_1 & -g_2 \\ -g_2 & 1-g_1 \end{pmatrix}. \tag{1.39}$$

The convergence perturb the source in that it is rescaled with a constant factor in all directions. To the first order, magnification, and sometimes demagnification,

[1] A full derivation of the theorem can be found in Chapter 2, p.585 in Misner et al. (2017)

depends only on κ. The overall shape of the image remains the same. The convergence is defined as

$$\kappa = \frac{\Sigma}{\Sigma_{\rm crit}} = \frac{1}{2}\boldsymbol{\nabla}^2_{\theta}\psi. \tag{1.40}$$

Shear is often written as a complex number with components

$$\gamma_1 = \frac{1}{2}(\psi_{,11} - \psi_{,22}) \tag{1.41}$$

$$\gamma_2 = \psi_{,12} = \psi_{,21} \tag{1.42}$$

with $\gamma = \gamma_1 + i\gamma_2$ and a magnitude $|\gamma| = (\gamma_1^2 + \gamma_2^2)^{1/2}$.

Shear describes the anisotropic distortion of a source caused by the tidal gravitational field. The intrinsic shape of the source is stretched along one direction according to γ_1 and γ_2.

The source image is affected by both the convergence and the shear. The distortions we observe, are a result of both. This is incorporated in the reduced shear g, defined as

$$g_i = \frac{\gamma_i}{1-\kappa}. \tag{1.43}$$

The total distortion acting on a circular source with radius R, will then result in an elliptic image with major and minor axes

$$a = \frac{R}{1-\kappa-|\gamma|} \quad \text{and} \quad b = \frac{R}{1-\kappa+|\gamma|}, \tag{1.44}$$

respectively.

The total magnification of a source as seen in its image, is the inverse of the determinant of the Jacobian:

$$\mu = \frac{1}{\det \mathcal{A}} = \frac{1}{(1-\kappa)^2 - |\gamma|^2} = \frac{1}{(1-\kappa)^2(1-|g|^2)}. \tag{1.45}$$

So the shape distortion is caused by the shear, while the magnification is caused by both the shear and the convergence.

1.4.6 Measurement

We do not usually know the size of a source prior to its magnification. What we do know, is the *ellipticity* of the image, and its orientation. For a circular source, the lensing-induced image ellipticity is defined as

$$\epsilon = \frac{1-b/a}{1+b/a} e^{2i\phi}. \tag{1.46}$$

where ϕ is the position angle with respect to our chosen center, and the magnitude of the ellipticity is $|\epsilon| = \frac{1-b/a}{1+b/a}$. This is what we actually measure when observing the background galaxy images.

In the weak lensing limit the ellipticity directly measures the reduced shear, $\epsilon = g$. Thus, we measure g rather than γ itself.

Sources are rarely ever circular. Background galaxies have an ellipticity of their own, owing to their orientation on the sky, and to their own intrinsic shape. The ellipticity we actually measure, is then the original ellipticity of the source, together with the ellipticity induced by the gravitational lens. In the weak lensing regime,

$$\epsilon_{\mathrm{I}} = \frac{\epsilon_{\mathrm{S}} + g}{1 - g^* \epsilon_{\mathrm{S}}} \approx \epsilon_{\mathrm{S}} + g, \tag{1.47}$$

where ϵ_{S} is the intrinsic ellipticity of the source, and where * denotes the complex conjugate.

We measure the mean ellipticity at $\boldsymbol{\theta}$ to get rid of the shape noise arising from the intrinsic shape of the sources, and instrument noise. We find that

$$\langle \epsilon \rangle \approx \langle g \rangle \tag{1.48}$$

This is the case for an ideal lens, where there is no signal distortion from things like atmospheric seeing, and the so called point-spread function (PSF). A more realistic measure of the ellipticity was developed by Kaiser et al. (1995). We will go through this method in Chapter 2, along with how to get a mass estimate from the measured ellipticity.

1.5 Galaxy clusters

Galaxies are not randomly distributed throughout space: They tend to cluster together, forming groups and clusters of galaxies. Groups consist of just a few galaxies, while clusters have up to a few 1000 galaxies. We can therefore observe overdensities of galaxies on the sky, and this was the original method of detecting clusters (Schneider 2006). This is how the Abell catalogs (Abell 1958; Abell et al. 1989) were made. Today, more than a hundred thousand clusters have been found.

Galaxy clusters are usually members of even larger structures called *superclusters*. Clusters and superclusters make up *filaments*, which are threadlike structures separated by voids, typically with a length of $50 - 80\,\mathrm{Mpc}$. Filaments are the largest known structures in the universe (Bharadwaj et al. 2004).

Galaxy clusters are the largest and most massive gravitationally bound structures that we know of, and they consist mostly of dark matter. The first indication of this came from Zwicky in 1933 (Andernach and Zwicky 2017), who noted that the galaxies in the Coma cluster move so fast that it would need at least 400 times the mass derived from observing the luminous matter, to keep the galaxies gravitationally bound. X-ray observations have also shown galaxy clusters to contain a very hot ($10^7 - 10^8$K) intracluster medium (ICM) emitting X-ray radiation (Bartelmann and Schneider 2001). They are the most luminous X-ray sources we have ever observed. We expect galaxy clusters to have a virial mass[1] on the order of $M_{\mathrm{vir}} \sim 10^{14} - 10^{15} M_{\odot}$, of which 80%

[1] Mass of a cluster, assuming dynamical equilibrium

is dark matter, $\sim 15\%$ is the intracluster medium, and $\sim 3\%$ is the baryons within the member galaxies (Schneider 2006). The virial radius of clusters are on the order of a few megaparsecs, $r_{\rm vir} \sim 1.5\,h^{-1}$, and the one-dimensional velocity-dispersion of the member galaxies is typically $\sigma_v \sim 1000\,{\rm km\,s^{-1}}$ (Schneider 2006).

The flux and temperature of the ICM, offers another way of estimating the mass and other properties, although we then assume the ICM to be in hydrostatic equilibrium and having a spherically symmetric potential. If we assume virial equilibrium, the velocity distribution of the member galaxies can also provide a mass estimate (Schneider 2006). These methods then confine us to dynamically stable clusters, unlike when using gravitational lensing.

There exists several subtypes of galaxy clusters, but we can divide them into two main ones: regular and irregular. The galaxies in regular clusters are mainly elliptical(E), lenticular(S0), and irregular galaxies with little star formation. Near the center, we often find a massive cD galaxy, which are the largest galaxies. The cluster is spherical in shape with a concentrated central core. They are frequently rich clusters, containing several thousand galaxies.

Irregular clusters come in many shapes, and often have fewer members than regular clusters. They can have strong substructure and no well-defined center. They contain elliptical, lenticular, and irregular galaxies, and a greater number of spiral(S) galaxies than regular clusters tend to. Many irregular clusters may have formed only recently, hence their irregularity (Schneider 2006).

Galaxy clusters are often used in gravitational lensing due to their massive size. As the lensing signal is proportional to the total mass of the cluster system, they were the first objects used in detecting the weak lensing signal (Hoekstra et al. 2013; Tyson et al. 1990).

There are multiple methods for detecting galaxy clusters. Cluster galaxies have the same redshift, and can be found using optical photometry and spectroscopic redshift surveys (e.g, Wen et al. (2012)). Cluster galaxies also tend have the same colors, forming the red sequence in a color magnitude plot, due to the high amount of red, elliptical galaxies (See Figure 2.6). Their red color is due to them consisting mainly of old, red stars, and there being little or no active star formation in these galaxies. The colors of elliptical galaxies are therefore evolving slowly with time.

As clusters are some of the brightest X-ray objects we know of, they have been identified in X-ray surveys. The Sunyaev-Zel'dovich (SZ) effect (Sunyaev and Zeldovich 1972), where the cosmic microwave background(CMB) is distorted, and low energy CMB photons are given an energy boost by high-energy electrons in galaxy clusters, has also been used (Carlstrom et al. 2000; Marriage et al. 2011).

1.5.1 Three clusters

There are three galaxy clusters that will be studied in this thesis. The images we use, are all taken by the HST, which is described in more detail in Chapter 2.

Two of the clusters were first imaged in the Sloan Digital Sky Survey (SDSS), but were only later detected as gravitational lenses. The first is the cluster SDSS

J1723+3411, detected by (Kubo et al. 2010), who also did a strong lensing study.

The second is SDSS J1226+2152, detected by Wen et al. (2009). SDSS J1226+2152 is a part of a larger complex structure consisting of several clusters. A strong lensing study of 26 clusters, including SDSS J1226+2152, has been done by Bayliss et al. (2011).

The third cluster is that of PSZ1 G311.65–18.48, which was first detected as a lens candidate in the Planck survey (Planck Collaboration et al. 2014). A previous strong lensing analysis has been done on this lens by Dahle et al. (2016).

All three of these cluster lenses have been studied in the past, using strong gravitational lensing, as they all contain bright luminous arcs. The two SDSS lenses are scheduled to be observed with the upcoming James Webb Space Telescope (JWST), as part of the TEMPLATES Early Release Science Program (Pls J. RIgby/J. Vieira). Hence we expect bigger data sets of them in the future. A weak lensing analysis of these three lenses, then seems appropriate.

In Table 1.1, some characteristics of the clusters are shown.

Table 1.1: Cluster characteristics. Here, z is the redshift, α is the right ascension, and δ is the declination and they are both listed in units of degrees. σ_v is the velocity dispersion of the clusters, and D_l is the angular diameter distance in a flat ΛCDM cosmology with $\Omega_{\mathrm{m},0} = 0.3$. A $-$ indicates that the parameter value has not been measured.

Cluster	z	α [deg]	δ [deg]	σ_v [km s^{-1}]	D_l [Mpc]
SDSS J1723+3411	0.444[a]	260.90064	34.199495	530 ± 17[a]	830.900
SDSS J1226+2152	0.435[b]	186.71543	21.873715	730^{+71}_{-119}[b]	821.127
PSZ1 G311.65–18.48	0.443[c]	237.52933	−78.19177	–	829.827

[a] from Kubo et al. (2010)
[b] from Bayliss et al. (2011)
[c] from Dahle et al. (2016)

The fields of PSZ1 G311.65–18.48, SDSS J1226+2152 and SDSS J1723+3411, can be seen in figures 1.2, 1.3, and 1.4.

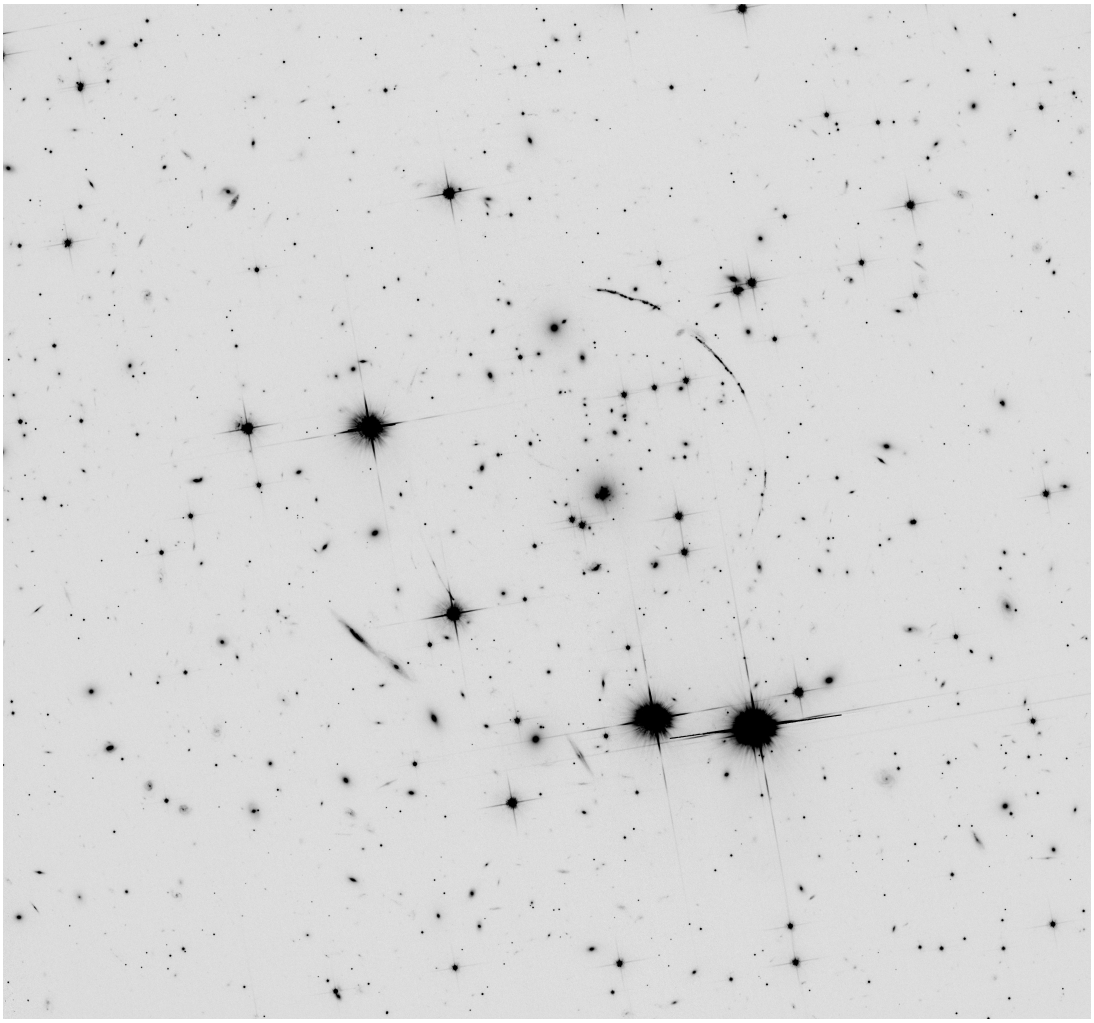

Figure 1.2: A slightly cropped image of the field of PSZ1 G311.65–18.48. North is up, and east is to the left in the image. The image is in the F814W filter. The field of view here is $867'' \times 165''$, or $5900 \times 5500\,\mathrm{pix}^2$.

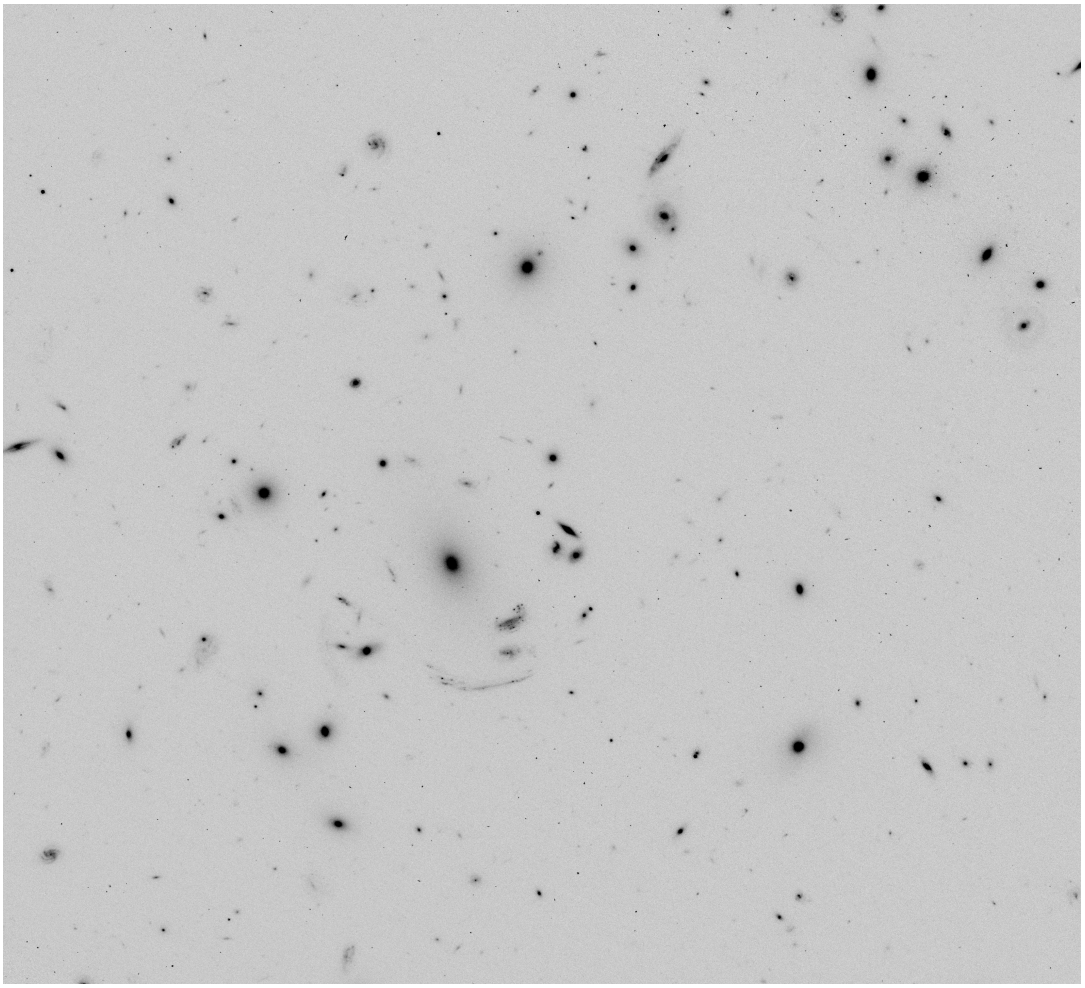

Figure 1.3: A cropped image of the field of SDSS J1226+2152. North is up, and east is to the left in the image. The image is in the F814W filter. The field of view here is $107'' \times 90''$, or $3300 \times 3000\,\mathrm{pix}^2$.

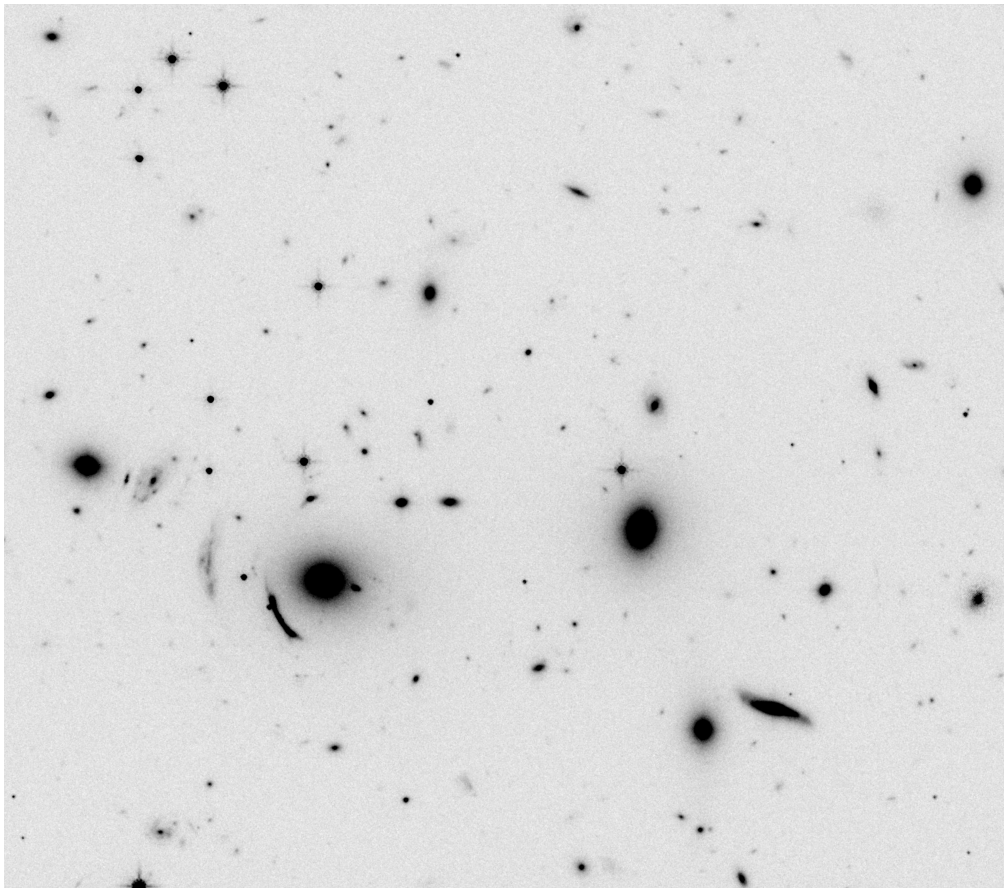

Figure 1.4: A cropped image of the field of SDSS J1723+3411. North is up, and east is to the left in the image. The image is in the infrared F110W filter. The field of view here is $94'' \times 69''$, or $2600 \times 2300\,\mathrm{pix}^2$.

Chapter 2

Method

We went through the basics of cosmology and gravitational lensing in Chapter 1. In this chapter we go more in depth on how to measure the shear of background galaxies that have been weakly gravitationally lensed by a galaxy cluster, and how we can use this to obtain a mass estimate of the gravitational lens. The images we are analyzing were taken in different filters by the Hubble Space Telescope (HST). We go through the properties of the telescope, and the specific detectors onboard that were used.

The images that we received were not the raw data taken by the HST. They had already been made ready for a scientific analysis, and so we briefly mention exactly what was done to the images prior to us receiving them.

We go through in detail how we analyze the images to obtain a shear estimate $\gamma^{\rm obs}$ by using the Kaiser-Squires-Broadhurst (KSB)(Kaiser et al. 1995) method with modifications made by Luppino and Kaiser (1997), and some corrections made by Hoekstra et al. (1998). We compare this estimate with the shear calculated from two different theoretical density profiles, that of a singular isothermal sphere (SIS), and the Navarro-Frenk-White (NFW) profile. In this way we fit the density profile to the observed data, and find an estimate of the mass of the lensing cluster.

We repeat that where necessary, we use a flat ΛCDM cosmology with $\Omega_{\rm m,0} = 0.3$ and $\Omega_{0,\Lambda} = 0.7$, and $H_0 = 100\,h\,{\rm km\,s^{-1}\,Mpc^{-1}}$, where $h = 0.7$.

The results of our weak lensing analysis are found in Chapter 3.

2.1 The Hubble Space Telescope

The images we study in this thesis were taken by different instruments and detectors onboard the Hubble Space Telescope (HST).

The HST was launched by NASA on the 24th of April, 1990, and remains in low Earth orbit. It is the only space telescope designed to undergo repairs and upgrades by astronauts, and there have been several such servicing missions (Garner 2015a). The fifth and final one was completed in 2009. Anyone, anywhere in the world can request time with the Hubble. Ultimately, it is the Space Telescope Science Institute (STScI) that decide which proposals and targets to accept, based on a process of peer

review by international panels of astronomers and technical feasibility evaluation by STScI. Meanwhile, the Goddard Space Flight Center is in control of the spacecraft itself. Should an astronomer's proposal be accepted, they have a six-month proprietary period, after which they are publicly released for anyone to see and study. This has made the Hubble a very productive telescope, with over 15 000 scientific articles published about its findings (Hille 2018).

As the telescope resides outside the atmosphere, light pollution, weather conditions, and atmospheric turbulence (seeing) does not affect its imaging, as is the case for ground-based telescopes. The HST is diffraction-limited, meaning that the angular resolution is limited only by the physics of light diffraction, and not other factors like those just mentioned. Ground-based observatories usually can not view details or separate between objects lying closer than 1 arcsecond ($''$, $1^\circ = 1/3600''$) on the sky. Meanwhile, the optimal angular resolution the HST can achieve, is $0.05''$ (Garner 2015b). The result is a telescope able to see deep into space, providing us with extremely high-resolution images.

The HST is 13.3 meters long, and has two mirrors. The primary mirror, which catches light from objects in space, has a diameter of 2.4 meters. The light is redirected to the 0.3 meter secondary mirror, which redirects the light to the focal plane where the instruments are. There are six instruments onboard the HST, consisting of cameras, spectrographs, and guidance sensors. They observe in the ultraviolet (UV), visible (V) and near-infrared (IR) part of the electromagnetic spectrum. The instruments also have built-in corrections to the spherical aberrations caused by the imperfect primary mirror. The Hubble is solar powered, having two solar arrays to power its batteries (Garner 2015b).

Numerous discoveries have been made possible due to the HST, such as determining the rate of expansion of the universe, finding extrasolar planets, studying galaxy mergers, or studying dark matter through gravitational lensing (Garner 2017a).

As no further servicing missions are planned, due to constant exposure to the radiation of space, the instruments will start to degrade, and eventually stop functioning. Still, the HST is expected to be able to continue operations into the 2020s. The infrared James Webb Space Telescope (JWST), which has a planned launch in 2021, will hopefully be able to work concurrently with the Hubble (Garner 2015b).

2.1.1 Instruments

Hubble possess cameras, spectrographs and interferometers. The two primary cameras, which are also the ones used to take our exposures, are the Wide Field Camera 3 (WFC3), and the Advanced Camera for Surveys (ACS).

The ACS replaced the Faint Object Camera (FOC) during the fourth servicing mission (Servicing Mission 3B). It detects light in the near-ultraviolet to the near-infrared wavelength range, through three independent channels. It was designed to survey large areas of the sky in great detail, and can also perform spectroscopy by use of a grism. It has a 10 times greater efficiency than the previous main camera, the Wide Field and Planetary Camera 2 (WFPC2).

Of the three channels of the ACS, the one we used was the Wide Field Channel (WFC). Its detector consists of two butted $2048 \times 4096\,\mathrm{pix}^2$ Charge Coupled Device (CCD) detectors. The field of view is $202'' \times 202''$, and the pixel size is $15\,\mu\mathrm{m} \times 15\,\mu\mathrm{m}$. Its pixel scale, which relates an object's angular size to the linear size of its image in the focal plane, is $0.05''$/pix (Ryon et al. 2019). The WFC has a number of filters, which can be found in the ACS handbook (Ryon et al. 2019). The WFC has a spectral coverage from 350 nm to 1100 nm, and is designed to be particularly sensitive to red wavelengths. This makes it an ideal tool for surveying redshifted galaxies and galaxy clusters, at moderate to large distances away (Garner 2016).

The WFC3 replaced the WFPC2 in the fifth and final servicing mission. It is therefore the most technologically advanced instrument onboard the HST, providing better resolution and a wider field of view than its predecessor. It offers a performance comparable to that of the ACS, but over a wider wavelength range, spanning from the ultraviolet to the near infrared. The WFC3 has two channels: the ultraviolet-visible (UVIS) channel, and the near-infrared (IR) channel. Their detectors are solid-state-devices (Garner 2017b; SpaceTelescope nd).

The UVIS channel detector is made up of two butted $2048 \times 4096\,\mathrm{pix}^2$ CCD detectors, with a pixel size of $15\,\mu\mathrm{m} \times 15\,\mu\mathrm{m}$. It has a field size of $160'' \times 160''$, giving it a resolution of $0.04''$/pix. It covers wavelengths from 200 nm to 1000 nm.

The IR channel detector has a single CCD detector with 1014×1014 active pixels (physical size is $1024 \times 1024\,\mathrm{pix}^2$) and a pixel size of $18\,\mu\mathrm{m}$. Its field of view is $123'' \times 136''$, resulting in a plate scale of $0.13\,''$/pix. Its spectral coverage if from 850 nm to 1700 nm, and it is designed to be insensitive to wavelengths above this, making it unnecessary to use a cryogenic cooler. Additional properties on both cameras and their channels can be found in the WFC3 (Dressel et al. 2019) and ACS (Ryon et al. 2019) instrument handbooks.

2.1.2 Imaging three clusters

For the cluster SDSS J1723+3411, the WFC3 camera was used. The images were taken between the 14th to 15th of March 2013 by Michael D. Gladders, and the proposal ID of these frames is 13003. Two images were taken by the UVIS channel with the filters F775W (775 nm) and F390W (390 nm), while two images were taken by the IR channel with the filters F160W (1600 nm) and F110W (1100 nm). Of these, only the F775W image is used in our analysis. The filters work, by allowing radiation of a certain wavelength to pass, while blocking out the rest. For instance, the F775W filter is centered at 775 nm, and allows a small range of wavelengths around this value, to pass. This image was made from combining four exposures, each with an exposure time of 595 seconds, and a total exposure time of 2380 seconds.

For the cluster SDSS J1226+2152, the WFC channel of the ACS was used to take two images: one with the F606W (606 nm) filter, and one with the F814W (814 nm) filter. We use both of these images. Four exposures were taken with each filter, with exposure time 512 seconds. The total exposure time of each image, is then 2040 seconds. The exposures were taken the 14th of April 2011. Their proposal ID is 12368.

Finally, for the cluster PSZ1 G311.65–18.48, one image was taken by the WFC channel of the ACS with the filter F814W (Proposal ID = 15101), and the other was taken by the UVIS channel of the WFC3 with the filter F606W (Proposal ID = 15377). The reason different cameras were used in the last case, is that the ACS is more sensitive than WFC3 in the F814W-band. This image is combined from eight exposures: four with an exposure time of 638 seconds, and four with an exposure time of 684 seconds, making it totally 5280 seconds. The F606W image was retaken at a later date, when the cluster was revisited. The image is combined from five exposures. Two had an exposure time of 742 seconds, and three had 994 seconds. The total is then 4466 seconds. The F814W exposures were taken the 21st to the 22nd of February 2018, and the F606W exposures were first imaged the 27th of September 2018, then re-imaged the 18th of January 2019.

2.1.3 AstroDrizzle

All data obtained by the different cameras are sent to the STScI Operational Pipeline Unified System (OPUS). Here the raw data is calibrated, and the resulting final FITS files are ready for scientific analysis.

The image calibration is done by two separate packages: `calacs` (for ACS) or `calwf3` (for WFC3), which corrects for instrumental effects, and `AstroDrizzle`, which corrects for geometric distortion, cosmic rays and hot pixels[1].

The `calacs`/`calwf3` package does the standard calibration of the data, i.e, removing the bias level, correcting for the charge transfer efficiency (CTE)[2], removing cosmic rays, subtracting the dark frames, and flat-fielding the images. The details of these processes can be found in the ACS (Lucas et al. 2018, p. 40–45) and WFC3 (Gennaro et al. 2018, p. 7–9 and 35–53) data handbooks. Remaining cosmic rays and hot pixels may be rejected by `AstroDrizzle`.

Drizzling is the informal term for linearly reconstructing undersampled data, thereby improving their resolution. It was originally developed for the HST, where the optics together with the detectors can provide excellent resolution over a small field of view, *or* it can undersample a larger field of view. Drizzling, is then a way of restoring the lost data when undersampling (Fruchter and Hook 2002). The `AstroDrizzle` package, is the one currently used for this reconstruction.

The concept behind it is straightforward enough: pixels in the input image are shrunk, then mapped onto the finer pixel grid of the output image. The shrunken pixels, are known as *drops*. This is shown in Figure 2.1. The full details can be found in the original article, Fruchter and Hook (2002).

Drizzling also can also remove geometric distortion, which the data taken by WFC3 and ACS are significantly affected by. The main reason for this is that the focal plane is tilted relative to the optical axis, which is necessary to preserve constant focus across all detectors. For the WFC3-UVIS channel and the ACS channels, the distortions runs

[1] Pixels that are damaged and experiences increased dark current (Lucas et al. 2018, p. 96).

[2] The CTE is a measurement for the fraction of electrons that are succsessfully moved from one pixel to another during read-out of the CCD.

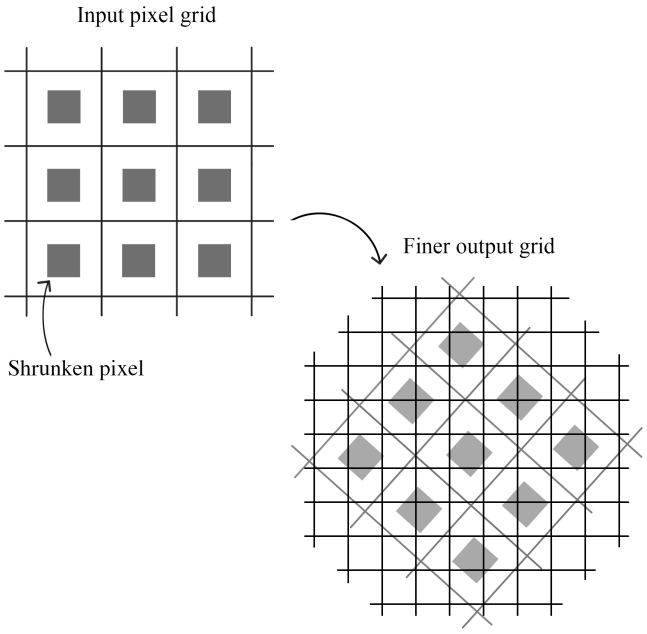

Figure 2.1: Figure showing the basic idea behind drizzling. The input pixels are shrunken, then mapped onto a finer output grid.

parallel to the diagonal of the CCD, making the projected field on the sky the shape of a rhombus (Dressel et al. (2019, Chapter 2.2); Lucas et al. (2018, p. 3)). This means that the area of the sky seen by a pixel, is not constant. The `AstroDrizzle` package is used to correct this. It also has its own cosmic ray rejection and hot pixel removal tools. More information on `Astrodrizzle` can be found in the data handbooks of the ACS (Dressel et al. 2019) and WFC (Lucas et al. 2018), or on the STScI `DrizzlePac` webpage[4].

The reduction of the images in filters F606W and F814W taken of the PSZ cluster, were conducted by Michael Florian. The observations were done using a 4-point dither pattern. Dithering are small changes in the telescope position between exposures. Celestial objects will then be shifted, while hot pixels and other artifacts will remain constant. Hence, dithering reduces the effects of bad pixels, and makes it easier to sample the point-spread function. The celestial objects are used as references when aligning the exposures.

The images in each filter, where aligned using the DrizzlePac routine `tweakreg`. The drop size was 0.8 of the original pixel, and Astrodrizzle using a Gaussian kernel, was used to drizzle the images onto a grid with a pixel size of $0.03''$ (Rivera-Thorsen et al. 2019).

[4] http://drizzlepac.stsci.edu/

2.2 Weak lensing theory

The basics behind gravitational lensing is covered in Section 1.4. We recap and expand on some of it here.

Light propagating through the gravitational field of a massive object, will experience a change in direction, and be delayed relative to light propagating through space, far outside of the field. This is what is called gravitational lensing. In the case of this thesis, the massive object is a galaxy cluster, while the source of light is background galaxies lying at a higher redshift than the cluster.

Gravitational lensing can be roughly divided into two types: *Strong gravitational lensing* occurs close to the cluster core, around the Einstein radius $\theta_{\rm E}$, and the sources can be bent and magnified into bright luminous arcs, or even be multiply imaged. *Weak gravitational lensing*, which is the subject of this thesis, happens at larger radii, and the effect causes a small but coherent distortion of the shape of background sources. To be able to measure this effect, we require a great number of sources. In Section 2.3, we go through how we can detect this effect through a statistical analysis called the Kaiser-Squires-Broadhurst (KSB) method.

A background galaxy with surface brightness $f^{\rm s}(\boldsymbol{\theta})$ will be distorted by the gravitational potential of the lens. The observed distortion will be

$$f^{\rm obs}(\theta_i) = f^{\rm s}(\mathcal{A}_{ij}\theta_j), \tag{2.1}$$

where θ is the 2D angular distance from the lens center in the lens plane, and $\theta = |\boldsymbol{\theta}|$. The distortion matrix, A_{ij} (See Equation 1.35), is the Jacobi matrix of the mapping of the source from the source plane, to its image in the lens plane.

The gravitational surface potential is denoted ψ. It is connected to the gravitational shear, γ, and the convergence, κ, through the relations,

$$\gamma_1 = \frac{1}{2}(\psi_{,11} - \psi_{,22}) \tag{2.2}$$

$$\gamma_2 = \psi_{,12} = \psi_{,21} \tag{2.3}$$

and

$$\kappa = \frac{1}{2}(\psi_{,11} + \psi_{,22}) \tag{2.4}$$

where the commas represent derivatives of Ψ with respect to the angular radius θ, in the lens plane

$$\psi_{,ij} = \frac{\partial^2 \psi(\boldsymbol{\theta})}{\partial\theta_i \partial\theta_j}. \tag{2.5}$$

The convergence is also related to the surface mass density of the gravitational lens, $\kappa = \Sigma_{\rm crit}/\Sigma$, where $\Sigma_{\rm crit}$ (see Equation 1.32) is the critical surface density. A usual condition for weak lensing, is that $\kappa \ll 1$. However, we will not be able to make this assumption in our analysis, as κ will be a significant contributor to the observed ellipticity. Both the convergence and the shear cause the distortions we see in the images of the sources. Convergence cause an isotropic magnification of the source, while

shear magnifies *and* induces ellipticity to the image, stretching it along one, privileged direction. The actual observable is thus the reduced shear, g, which parametrizes both of these effects:

$$g = \frac{\gamma}{1-\kappa}. \tag{2.6}$$

The reduced shear is then the distortion induced by the gravitational lens onto the image, as light from the source propagates through its potential. But background galaxies have an intrinsic ellipticity of their own. The ellipticity of the image we observe, $\epsilon_{\rm I}$ is therefore a result of both g *and* the intrinsic ellipticity of the sources, $\epsilon_{\rm S}$. Additionally, the measured ellipticity will be affected by the point-spread-function (PSF). The PSF is caused by the telescope optics when in space, and, in ground-based telescopes, by atmospheric seeing, telescope guiding errors, and atmosperhic dispersion as well. Hence, the equation for the image ellipticity $\epsilon_{\rm I}$ in Equation 1.47, describes a very ideal case, and not what we actually observe. Kaiser et al. (1995) developed a method of measuring the shear and ellipticity, while accounting for all these things, and some modifications and corrections to their method were made later (Luppino and Kaiser 1997; Hoekstra et al. 1998). We will go through the modified method in Section 2.3.

It can be useful to express the shear, the reduced shear, and the ellipticity in terms of a tangential component, denoted T, and a curl (or cross) component, denoted $\times$. They are rotated 45° relative to each other. The shear, for instance, is then written as

$$\gamma_{\rm T} = -(\gamma_1 \cos 2\phi + \gamma_2 \sin 2\phi) \tag{2.7}$$

$$\gamma_{\times} = -(\gamma_2 \cos 2\phi - \gamma_1 \sin 2\phi), \tag{2.8}$$

where ϕ is the azimuthal angle with respect to our chosen center, which will be the central galaxy in the cluster. In the case of a spherically symmetric density profile, like that of the singular isothermal sphere, or the NFW-profile (see Equation 2.51 and Section 2.5.2), $\gamma_{\times} = 0$, and the shear we measure is just the tangential shear.

The convergence can only be recovered up to a constant κ_0. This reflects the fact that we can add a uniform mass sheet to the lens mass without altering the shear. This is known as the *mass-sheet degeneracy*, and was initially discovered by Gorenstein et al. (1988). As we will fit our data to mass density profiles, this will not be a problem, although it will affect the *aperture mass*, which is defined in Section 2.3.4.

2.2.1 The PSF

The point-spread function (PSF) plays an important role in astrophysical imaging. We can say that the PSF is how the imaging system responds to a single, infinitely small point source.

The telescope objective captures a fraction of the light emitted, and in an ideal world, this light would get focused to an infinitely small point in the focal plane. What happens instead, is that the light waves undergo diffraction, converging and interfering with each other, resulting in the image of an Airy disk.

In ground-based telescopes, atmospheric seeing will affect the PSF. While we do not have to worry about atmospheric seeing when doing observations with the Hubble

Space telescope, the PSF will still not be perfectly isotropic. It will vary both spatially, and with time. There are various reasons for this, from the behavior of the detectors and the optical system, to the mechanics that makes the telescope move slightly while observing (Gentile et al. 2012).

The PSF is important to know and correct for: The isotropic part of the PSF will smear elliptical objects, making their shapes appear circular, while the anisotropic part will induce ellipticity in intrinsically circular objects. In gravitational lensing, the true lensing signal can then be drowned out, at the same time, we will detect "false" lensing effects. The weak gravitational lensing signal is already very low. A PSF that has not been corrected for, can easily dominate the measured ellipticity of small background galaxies, which are often smaller than the PSF itself. For bigger galaxies, the effect of the PSF will be smaller.

To determine the anisotropy in the PSF, we would need several points sources, scattered throughout our field of view. In astronomical imaging, we are lucky enough to have of point sources in the form of stars and quasars. However, the amount of points sources will depend on the target position in the sky: whether there are plenty of foreground stars or not.

We go into the practical aspect of how to determine and correct for the PSF in Section 2.3.1, and how we separate the stars from galaxies in Section 2.4.3.

2.3 Shear measurements

There are multiple ways of converting the observed ellipticity of an image, into the induced gravitational shear. We will apply the Kaiser-Squires-Broadhurst (KSB) method, which can be found in full in Kaiser et al. (1995), along with some modifications by Luppino and Kaiser (1997) and Hoekstra et al. (1998).

We use the `IMCAT` software package developed by Nick Kaiser for many of the operations needed on our way to obtaining a mass estimate. The full definition of the commands can be found on Kaisers webpage[1][2].

2.3.1 Object ellipticities

The relation between the ellipticity ϵ and reduced shear g, is not as simple as stated in the Section 1.4.6.

A more accurate parametrization of the observed ellipticity, is the *weighted ellipticity*, or *polarization* parameters, e_α. They are defined from the weighted quadrupole moments,

$$Q_{ij} = \int W(\theta)\theta_i\theta_j f(\boldsymbol{\theta})\,\mathrm{d}^2\boldsymbol{\theta}, \tag{2.9}$$

where $f(\boldsymbol{\theta})$ is the image surface brightness, and $W(\theta)$ is a Gaussian distributed weight function, or window function, with scale length r_g, equal to that of the galaxies.

[1] https://www.ifa.hawaii.edu/ kaiser/imcat/

[2] The webpage was down at the time of this writing, although the same manual can be found at http://docplayer.net/45170446-The-imcat-reference-manual.html

The polarization parameters can then be written as

$$e_\alpha \equiv \frac{Q_\alpha}{T}, \tag{2.10}$$

where

$$Q_1 \equiv Q_{11} - Q_{22}, \quad Q_2 \equiv 2Q_{21}, \quad T \equiv Q_{11} + Q_{22}. \tag{2.11}$$

Shear, induces a systematic shift in the polarization parameters. To the first order, the shift, δe_α, caused by the reduced gravitational shear, g, is

$$\delta e_\alpha = P^{\rm sh}_{\alpha\beta} g_\beta \tag{2.12}$$

where we sum over β, and $P^{sh}_{\alpha\beta}$ is the *post-seeing shear polarizability tensor*, which can be measured for each individual source image. That it is "post-seeing" means that $P^{\rm sh}_{\alpha\beta}$ measures the response of an object to the shear *before* we have made corrections for the smearing due to the seeing disk, or in our case, due to the PSF alone. Note that, despite the name, $P^{\rm sh}_{\alpha\beta}$ is not a tensor, since it transforms e_α, which has two components, but is not a vector. We therefore use greek letters to distinguish them from real vectors.

The *pre-seeing* shear polarizability tensor, $P^g_{\alpha\beta}$ (Equation 2.22) was first defined by Luppino and Kaiser (1997), and is calculated from $P^{\rm sh}_{\alpha\beta}$.

$P^{\rm sh}_{\alpha\beta}$ is defined as

$$P^{\rm sh}_{\alpha\beta} = X^{\rm sh}_{\alpha\beta} - e_\alpha e^{\rm sh}_\alpha, \tag{2.13}$$

where (Hoekstra et al. 1998)

$$X^{\rm sh}_{\alpha\beta} = \frac{1}{T}\int \begin{bmatrix} 2W\theta^2 + 2W'(\theta_1^2-\theta_2^2)^2 & 4W'(\theta_1^2-\theta_2^2)\theta_1\theta_2 \\ 4W'(\theta_1^2-\theta_2^2)\theta_1\theta_2 & 2W\theta^2 + 8W'\theta_1^2\theta_2^2 \end{bmatrix} f(\boldsymbol{\theta})\,{\rm d}^2\boldsymbol{\theta}, \tag{2.14}$$

and

$$e^{\rm sh}_\alpha = 2e_\alpha + \frac{2}{T}\int \begin{pmatrix} \theta_1^2-\theta_2^2 \\ 2\theta_1\theta_2 \end{pmatrix} \theta^2 W'\,{\rm d}^2\boldsymbol{\theta}. \tag{2.15}$$

Here, $'$ denotes the derivative with respect to θ^2.

The objects will experience a smearing because of the anisotropic PSF. Kaiser et al. (1995) assumed that the PSF can be modeled as a convolution of a circularly smeared image, with a small and highly anisotropic kernel $k(\boldsymbol{\theta})$. The kernel has the unweighted quadrupole moments, q_{lm},

$$q_{lm} \equiv \int \theta_l\theta_m k(\boldsymbol{\theta})\,{\rm d}^2\boldsymbol{\theta}. \tag{2.16}$$

While this is a good assumption for ground based data, the PSF of the HST cameras are more complicated. This can, however, be rectified somewhat by using the galaxy scale length, $r_{\rm g}$ in the window function, $W(\theta)$, when determining the PSF (Hoekstra et al. 1998), which we go into detail on in the next subsection.

The shift in polarization due to the PSF, is then

$$\delta e_\alpha = P^{\rm sm}_{\alpha\beta} p_\beta, \tag{2.17}$$

where p_β is a measure of the anisotropy of the PSF, given by

$$p_\alpha = \begin{pmatrix} q_{11} - q_{22} \\ 2q_{12} \end{pmatrix}, \tag{2.18}$$

and where the *smear polarizability tensor*, $P^{\rm sm}_{\alpha\beta}$ of an object, is defined as

$$P^{\rm sm}_{\alpha\beta} = X^{\rm sm}_{\alpha\beta} - e_\alpha e^{\rm sm}_\alpha \tag{2.19}$$

where (Hoekstra et al. 1998)

$$X^{\rm sm}_{\alpha\beta} = \frac{1}{T} \int \begin{bmatrix} W + 2W'\theta^2 + W''(\theta_1^2 - \theta_2^2)^2 & 2W''(\theta_1^2 - \theta_2^2)\theta_1\theta_2 \\ 2W''(\theta_1^2 - \theta_2^2)\theta_1\theta_2 & W + 2W'\theta^2 + 4W''\theta_1^2\theta_2^2 \end{bmatrix} f(\boldsymbol{\theta})\, {\rm d}^2\boldsymbol{\theta}, \tag{2.20}$$

and

$$e^{\rm sm}_\alpha = \frac{1}{T} \int \begin{pmatrix} \theta_1^2 - \theta_2^2 \\ 2\theta_1\theta_2 \end{pmatrix} (2W' + W''\theta^2) f(\boldsymbol{\theta})\, {\rm d}^2\boldsymbol{\theta}. \tag{2.21}$$

Here, $''$ is the double derivative with respect to θ^2.

What we want to measure is the pre-seeing shear. Luppino and Kaiser (1997) present in their appendix A, a useful way of calculating the pre-seeing polarization tensor $P^g_{\alpha\beta}$, and a full derivation can be found there,

$$P^g_{\alpha\beta} = P^{\rm sh}_{\alpha\beta} \left(1 - \frac{e^2}{2}\right) - P^{\rm sm}_{\alpha\delta} \frac{P^{\rm sh\star}_{\delta\mu}}{P^{\rm sm\star}_{\mu\beta}}, \tag{2.22}$$

where * denotes the tensors applied to stellar objects. This tensor can then be measured directly from the observations. Hoekstra et al. (1998) notes, that it is important that the weight function W that is used when measuring $\frac{P^{\rm sh\star}_{\delta\mu}}{P^{\rm sm\star}_{\mu\beta}}$, is the same one used when measuring $e^{\rm obs}_\alpha$ for a galaxy, as $\frac{P^{\rm sh\star}_{\delta\mu}}{P^{\rm sm\star}_{\mu\beta}}$ vary with $r_{\rm g}$. We choose to add the $(1 - e^2/2)$ factor as a correction to the $P^{sh}_{\alpha\beta}$ tensor, as, while testing different ways of measuring shear, Heymans et al. (2006) found this correction to reconstruct the shear the best.

Accounting for the smearing by the PSF, and having found the pre-seeing shear polarizability, the observed ellipticity of an image is then

$$e^{\rm obs}_\alpha = e^{\rm s}_\alpha + P^g_{\alpha\beta} g_\beta + P^{\rm sm}_{\alpha\beta} p_\beta, \tag{2.23}$$

where $e^{\rm s}_\alpha$ is the intrinsic ellipticity of the galaxy. $P^g_{\alpha\beta}$, $P^{\rm sm}_{\alpha\beta}$, and $e^{\rm obs}_\alpha$ are calculated by the `IMCAT` command `getshapes`.

Determining the PSF anisotropy

To calculate the shift in the polarization, δe_α (Equation 2.17), due to the PSF anisotropy, we need to find p_β. One way of doing so, is by applying Equation 2.23 to stellar objects. Stars are intrinsically circular ($e_\alpha^{s\star}$=0), and lie in front of the lens, so they are not sheared ($g_\beta^\star = 0$), hence stars are only affected by the PSF. We find

$$p_\alpha = \frac{e_\beta^{\mathrm{obs}\star}}{P_{\beta\alpha}^{\mathrm{sm}\star}}. \tag{2.24}$$

If we use this in Equation 2.17, the galaxy ellipticities can be corrected with an amount $-\delta e_\alpha$.

When we have a catalog of stars, we can use the `IMCAT` command `efit` to find the PSF anisotropy. `efit` uses a Taylor expansion, up to the sixth order, where the coefficients are fitted to the p_α values of the stars. As the stars are so bright, photon counting noise is negligible. We can then run `ecorrect` on our galaxy catalog, and are left with objects with an ellipticity only affected by the isotropic PSF, and reduced shear g. In Figure 2.2 we see the ellipticity of the stars before and after having been corrected for the PSF.

While drizzling helps reconstruct lost data when undersampling (see Section 2.1.3), stars are so small that they can still remain unresolved. This is true for the images we are analyzing in this thesis. We see this when correcting the stars for the anisotropic PSF: While they do lie closer to the origin in the second e_α plot, they can still remain quite scattered due to the uncertainty of the ellipticity measurements. We try to fit the PSF to the best of our abilities, regardless.

The fields of PSZ1 G311.65-18.48 and SDSS J1723+3411 have the highest number of foreground stars, 159-304 and 60, respectively. We are therefore able, in both cases, to fit a 6th order polynomial to the PSF. SDSS J1226+2152 lie further away from the plane of Milky Way. Its field has therefore very few foreground stars, only between 9 and 16. A 3rd order polynomial, then seems to fit the PSF the best.

2.3.2 Shear estimates

We rewrite Equation 2.23 to an expression for the reduced shear g,

$$g_\alpha = \frac{e_\beta^{\mathrm{obs}} - e_\beta^{\mathrm{s}} - P_{\beta\alpha}^{\mathrm{sm}} p_\alpha}{P_{\beta\alpha}^{g}} = \frac{e_\beta^{\mathrm{psm}} - e_\beta^{\mathrm{s}}}{P_{\beta\alpha}^{g}}. \tag{2.25}$$

In the last equality, $e_\alpha^{\mathrm{psm}} = e_\alpha^{\mathrm{obs}} - P_{\alpha\beta}^{\mathrm{sm}} p_\beta$ is the observed ellipticities corrected for the anisotropic PSF using the `efit` and `ecorrect` commands described in the previous subsection.

Assuming the PSF is now close to circular, the off-diagonal elements of the polarizability tensors will be small compared to the diagonal elements. Ideally, they would be zero, but due to the various sources of noise in the data, they will instead have some low value. We can then approximate the polarizabilities with $P = \frac{1}{2}(P_{11} + P_{22})$ (Wold

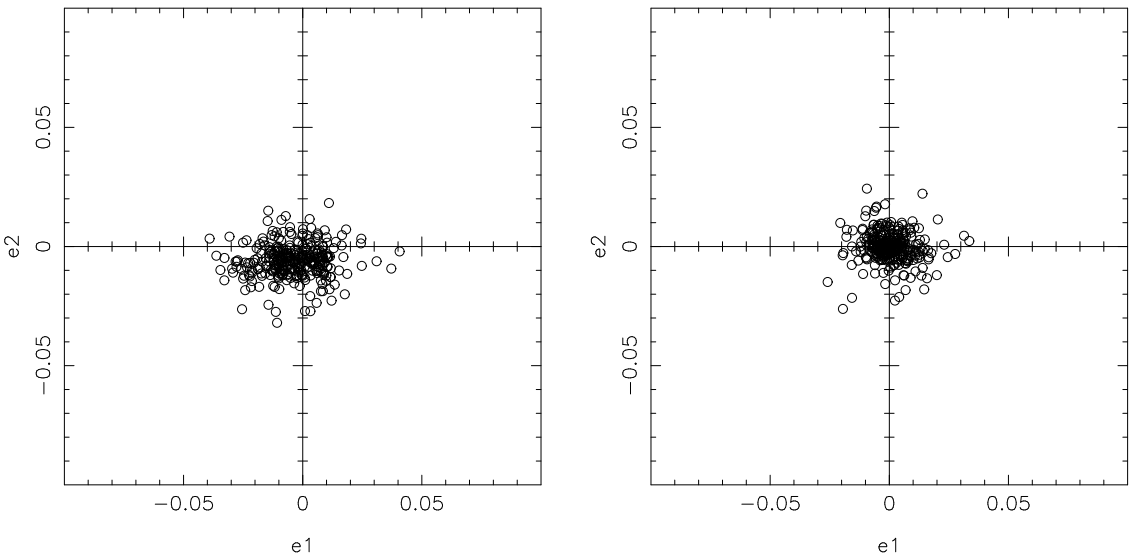

Figure 2.2: e_1 versus e_2 plot of stars in the foreground of PSZ1 G311.65–18.48, in the F814W filter. The image to the left shows the stars prior to being corrected for the anisotropic PSF. The image to the right, shows the stars after the correction has been applied. We see that in the right-hand image, the stars are more centralized around the origin, but still with some scatter. The scatter is most likely due to the HST undersampling the stars, leading to uncertainty in the ellipticity measurements.

et al. 2002). The mean $P^{\rm sh\star}/P^{\rm sm\star}$ across all the stars, $N_{\rm stars}$, can then be calculated as

$$\left\langle \frac{P^{\rm sh}}{P^{\rm sm}} \right\rangle^{\star} = \frac{1}{N_{\rm stars}} \sum_{\rm stars} \frac{P_{11}^{\rm sh\star} + P_{22}^{\rm sh\star}}{P_{11}^{\rm sm\star} + P_{22}^{\rm sm\star}}. \tag{2.26}$$

The pre-seeing shear polarizability is then

$$P^{g} = \frac{1}{2}(P_{11}^{\rm sh} + P_{22}^{\rm sh}) \left(1 - \frac{e^2}{2}\right) - \frac{1}{2}(P_{11}^{\rm sm} + P_{22}^{\rm sm}) \left\langle \frac{P^{\rm sh}}{P^{\rm sm}} \right\rangle^{\star}. \tag{2.27}$$

We use the `IMCAT` command `getshapes` to find $e_\alpha^{\rm obs}$ $P^{\rm sh}$ and $P^{\rm sm}$ for every object. We can then find the reduced shear according to Equation 2.29.

Now, we *can* correct for the PSF in each individual galaxy, and each galaxy has a P^g associated with it. As this tends to introduce additional noise, it is not what we will do to find the reduced shear. Instead, we separate the background galaxies into bins based on their magnitude and $r_{\rm g}$. The bins have a spacing so that we have approximately the same number of galaxies in each, although there is a scatter of about 20 galaxies, for every cluster.

The mean $r_{\rm g}$ of a bin is used in the weight function W to calculate the weighted quadrupole moments Q_{ij} (Equation 2.9), used in finding the polarizabilities and the anisotropic PSF.

In each bin, we find the reduced shear g, by calculating the median P^g, $\tilde{P}^g$, and applying it to the galaxies in that bin.

$$g_\alpha = \frac{e_\alpha^{\rm psm} - e_\alpha^{\rm s}}{\tilde{P}^g}. \tag{2.28}$$

We can say that $1/\tilde{P}^g$ is a correction factor, applied to each galaxy to find the reduced shear. But we are not quite there yet, since g_α in the above equation is still contaminated by the "shape noise" intrinsic to each galaxy prior to being lensed.

As we assume galaxies to be randomly oriented, the mean intrinsic ellipticity of background galaxies should average out to zero, $\langle e_\alpha^{\rm s} \rangle \approx 0$, provided we have a sufficient sample of sources. Using this, the mean reduced shear, $\langle g \rangle$, becomes

$$\langle g_\alpha \rangle = \left\langle \frac{e_\alpha}{\tilde{P}^g} \right\rangle. \tag{2.29}$$

We will use this fact to find a mass estimate of the cluster in Section 2.3.4

Weights

As stated in Section 2.2.1, small and faint (low S/N=signal-to-noise ratio) objects are more heavily affected by the PSF, resulting in a larger $1/P^g$. For large and bright objects, this correction factor is close to unity. Objects having a low S/N increases the uncertainty in their ellipticity measurements. We therefore choose to assign weights to the galaxies, making faint objects matter less in determining the reduced shear. We calculate weights, w_i for each galaxy in bin i,

$$w_i = \frac{1}{\sigma_{g,i}^2} \left(\frac{\sum_i N_i}{\sum_i (N_i/\sigma_{g,i}^2)} \right). \tag{2.30}$$

Here, $\sigma_{g,i}$ is the dispersion in the reduced shear g in bin i and the term inside the parenthesis is a normalization constant, where N_i is the number of background galaxies in each bin, and $\sum_i N_i$ is the total number of background galaxies in the catalog.

The weighted shear of each galaxy j in bin i, is then $g_{{\rm w},j} = w_i g_j$.

2.3.3 Distances

The ratio of the angular diameter distance between the source and the lens, $D_{\rm ls}$, and the observer and the source, $D_{\rm s}$, is given by

$$\beta = \frac{D_{\rm ls}}{D_{\rm s}}. \tag{2.31}$$

The redshift of the source galaxies are unknown, but we will assume that they lie in the same source plane, at $z_{\rm s} \approx 1$.

The angular diameter distance can be calculated from the luminosity distance, $D_{\rm A} = D_{\rm L}/(1+z)^2$. For flat cosmologies with a cosmological constant Λ, Pen (1999) provides a good approximation to the luminosity distance from redshift $z = 0$, to some redshift z. We use this approximation to calculate $D_{\rm l}$ and $D_{\rm s}$. We then use $D_{\rm l}$ and $D_{\rm s}$ to approximate β in the same way as Wilson et al. (2001).

Finally, for each galaxy, j, we calculate the weighted β,

$$\beta_{{\rm w},j} = w_i \beta_j, \tag{2.32}$$

where w_i are the same weights as in Equation 2.30. We use the mean $\beta_{\rm w}$ value of our galaxies, $\langle\beta_{\rm w}\rangle$, to calculate $\Sigma_{\rm crit} = \frac{c^2}{4\pi G D_{\rm l}\langle\beta_{\rm w}\rangle}$.

By using the analytical expression for the angular diameter distance in an Einstein-de Sitter universe (EdS)($\Omega_{m,0} = 1$),

$$D_{\rm A}^{\rm EdS} = \frac{2c}{H_0}(1-(1+z)^{-1/2})\frac{1}{1+z}, \tag{2.33}$$

we can correct for the small error using Pen's approximation induces in $D_{\rm l}$,

$$D_{\rm l} = D_{\rm l}^{\rm approx}\frac{D_{\rm l}^{\rm EdS}}{D_{\rm l}^{\rm EdS,approx}}. \tag{2.34}$$

2.3.4 Mass densitometry

As briefly mentioned in section 1.4.6, we can use the shear γ to find the convergence, κ, which can be converted into an estimate of the projected mass of a gravitational lens.

One way to make an estimate of the surface mass density of the cluster, is by using the ζ-statistic (Fahlman et al. 1994) which estimates the mean convergence within radius θ_1,

$$\zeta(\theta_1,\theta_2) = 2\left(1-\frac{\theta_1^2}{\theta_2^2}\right)^{-1}\int_{\theta_1}^{\theta_2}\langle\gamma_T\rangle\,{\rm d}\ln\theta = \bar{\kappa}(\theta<\theta_1) - \bar{\kappa}(\theta_1<\theta<\theta_2). \tag{2.35}$$

Here, $\bar{\kappa}(\theta<\theta_1)$ is the mean convergence within angular radius θ_1, and $\bar{\kappa}(\theta_1<\theta<\theta_2)$ is the mean convergence within an annulus bounded by θ_1 and θ_2. Meanwhile, $\langle\gamma_{\rm T}\rangle$ is the azimuthally averaged tangential shear defined as

$$\langle\gamma_{\rm T}\rangle = \int\gamma_T\frac{{\rm d}\phi}{2\pi}, \tag{2.36}$$

where $\gamma_{\rm T} = -\gamma_1\cos 2\phi - \gamma_2\sin 2\phi$, and ϕ is the azimuthal angle with respect to our chosen center.

This provides us with a lower bound on the mean convergence interior to radius θ_1, $\bar{\kappa}(\theta<\theta_1)$, without actually measuring the shear inside this radius. We only measure the galaxy ellipticities in an annulus just outside θ_1, bounded by θ_1 and θ_2.

We can say that the *aperture mass*, $M_{\rm ap}$, is the estimated projected mass of our cluster when not making any assumptions as to the cluster's real density profile. Due

to the mass-sheet degeneracy, this estimate is only accurate up to a constant. To get an as accurate value of the aperture mass as possible, we put $\theta_1 = \theta_{\rm inner}$, and $\theta_2 = \theta_{\rm outer}$ in Equation 2.35, where these radii are the innermost radius in our analysis, and the outer radius of our field, respectively. We only have a single annulus, but one that has a lower mean convergence than if θ_2 had some smaller value. In terms of the physical 2D radius $\xi = D_{\rm l}\theta$, the aperture mass is then defined as

$$M_{\rm ap}(< \xi_{\rm inner}) = \pi \xi_{\rm inner}^2 \zeta(\xi_{\rm inner}, \xi_{\rm outer}) \Sigma_{\rm crit} \tag{2.37}$$

Our choice of $\theta_{\rm inner}$ and $\theta_{\rm outer}$, will affect our mass estimate. If $\theta_{\rm outer}$ is too small, only a few background galaxies will be present in the annulus, generating uncertainty in the measurements (Poisson noise). If $\theta_{\rm outer}$ is too large, we risk that our shear measurements are contaminated by other nearby clusters' gravitational fields. We must also make $\theta_{\rm inner}$ large enough, so that we do not measure any strong lensing effects: the weak lensing approximation must hold. We do the latter by ensuring that our inner radius is larger than the Einstein radius, $\theta_{\rm inner} = \frac{3}{2}\theta_{\rm E}$. This particular value arises from the fact that, when using a SIS density profile, $\kappa = \gamma$ and $g = 1$ at the Einstein radius. We wish to avoid any strong lensing effects, and so want to only measure shear where $g < 1/2$, resulting in the given minimum radius through the relation $g = \gamma/(1-\kappa)$.

We do not use the average shear $\langle \gamma_{\rm T} \rangle$ in Equation 2.35, but rather the average reduced shear $\langle g_{\rm T} \rangle$, given by Equation 2.29. The `IMCAT` command `etprofile` accepts $\theta_{\rm inner}$, $\theta_{\rm outer}$, $g_{\rm w}$ and a log bin size. `etprofile` then divides the field into radial bins, or annuli, with the provided size, and calculates then outputs the ζ-statistic and measured mean tangential reduced shear $\langle g_{\rm T} \rangle$ (provided we already did all the previous steps in this section, otherwise, it returns $\langle e_{\rm T} \rangle$) in the annuli, along with error estimates. We also get the inner radii and mean radii of the annuli, the number of galaxies in each bin, and the S/N of each bin. We can now estimate the aperture mass, Equation 2.37, and also fit the measured shear to a density profile.

To decrease the noise arising from the intrinsic shape of the galaxies, prior to their lensing, we have a minimum of 10 galaxies in each bin. This is not an issue as the radius increases, and the number of galaxies in each bin reaches the hundreds, but in the innermost annulus, the number tends to be smaller. For instance, for SDSS J1226+2152, we end up with only 16 galaxies in the innermost bin.

2.4 Weak lensing pipeline

This section can be viewed as a summary of the weak lensing analysis. We start with how we calibrate our images, and how we can detect objects in them. We end with a short recap of how to obtain a mass estimate of the cluster by measuring the shear.

2.4.1 Image analysis

Before we can start detecting objects, the images need some additional work.

The first thing we do is remove corrupt data, such as bad pixels, or areas outside the camera aperture. The pixels outside the aperture are valued as NaN (Not a Number) in

our image, or 0. In either case these pixel values are converted into a very low value by using the `IMCAT` command `ic` coupled with the `MAGIC` argument. This gives the pixel the `MAGIC` value, which is the largest negative value available in the pixel format, and is used by `IMCAT` for masking bad pixels which are ignored in subsequent calculations.

Ideally, our exposures would only contain the signals of stars and galaxies and other astrophysical phenomena of interest. But we do in fact record radiation from the background sky as well. We set the background to zero, by subtracting the median pixel value from the image. The median value, along with other statistical properties of the `fits` image, is found by the `stats` command.

2.4.2 Detecting objects

Objects were detected by use of the `hfindpeaks` command from the `IMCAT` software.

It works by smoothing the image with Mexican hat filters with different radii, then detecting the objects with the highest significance. The smoothing reduces the noise in the image, and thereby also false detections. The trade-off is that we may lose some very faint objects. We choose a significance threshold of $\nu = S/N = 10$. We then get a catalog of stars, galaxies, and some artifacts due to noise and cosmic rays. We also get some parameters, like ν, and the smoothing radius r_{g}.

Next we use `apphot` to perform an aperture photometry. We then measure the flux, magnitude, half-light radius r_{h}, and other related quantities. As the images have already been corrected for the background, `apphot` calculates the growth curve for the integrated light as a function of radius,

$$l(< r) \equiv 2\pi \int \theta f(\boldsymbol{\theta})\, \mathrm{d}\theta, \tag{2.38}$$

where $f(\boldsymbol{\theta})$ is the background corrected surface brightness. This is done by placing an aperture over the object, and summing the pixel values. The radius of the aperture should be large enough to contain all the light from the object without being contaminated by neighboring objects, `apphot` therefore uses a radius of $3r_{\mathrm{g}}$. The luminosity and the half-light radius r_{h}, which is the radius at which intensity is halved, is estimated from this aperture.

We use the command `getsky` to determine the local background around objects.

Some of the objects detected are artifacts created by strong lensing effects, noise, bleeding pixels due to saturated foreground stars, or cosmic rays that slipped through the `Astrodrizzle` software. The `cleancat` command will put a limit on how close bright neighboring objects are allowed to be to one another, thereby filtering out a lot of the bleeding pixels and arcs produced by strong lensing, which we have in all of our fields. This can be seen in picture 2.3.

The noise and cosmic rays can be removed in several ways. If we have multiple exposures of the same field, in different filters for instance, we can use the commands `mergecats` together with `unmergecat`, to only select objects that are detected in both filters. Both noise and artifacts, which can vary between exposures, will then be reduced. As far as it is possible, this is the best way. Another way is by putting a limit

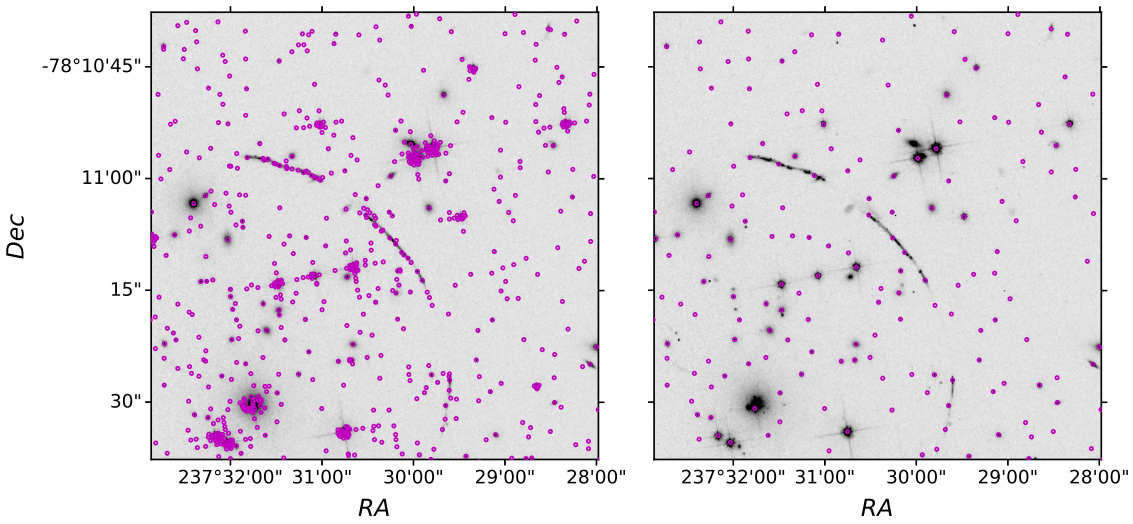

Figure 2.3: Close-up of the field of PSZ1 G311.65–18.48 in the F814W filter. The left-hand image shows all the initial object detections, marked in magenta. The image on the right shows the objects after we have performed `cleancat`. We see that there is now only one object per saturated star, and fewer objects on the strong lensing arc. `getshapes` have also been performed in the right image, meaning some objects, whose trace of the quadrupole moments were negative, have also been rejected.

on the measured polarizability parameters, $e_\alpha^{\max} = 0.99$. This will remove trailing lines of cosmic rays in the field, which have an ellipticity close to 1.

2.4.3 Separating stars from galaxies

In order to differentiate between galaxies and stars, we create a diagram showing the magnitudes of the detected objects, versus their radius, r_h (or r_g). The stars can be faint or bright, and have a very similar, small radius. In the diagram, this makes them lie in a vertical column. They have been marked in Figure 2.4.

The trailing tail of the star-column at bright magnitudes and increasing radius, is caused by saturated stars in the exposure, making their radii blow up. Faint stars blend easily with small galaxies, hence our initial pick of stars are the obvious ones that lie in the column. We use `getshapes` to measure the polarization parameters e_α, $P_{\alpha\beta}^{\mathrm{sm}}$ and $P_{\alpha\beta}^{\mathrm{sh}}$ in our object catalog, prior to selecting the stars. We can then do an additional filtering by plotting e_1 against e_2, in our star catalog. This can be seen in Figure 2.5. As stars are intrinsically circular, we expect them to lie close to the origin, even when affected by the PSF. Galaxies, we expect to have an ellipticity, and so should lie further from the center.

Now that we have found stars, we put them in a separate catalog. These will be used to estimate the PSF, described in Section 2.3.1.

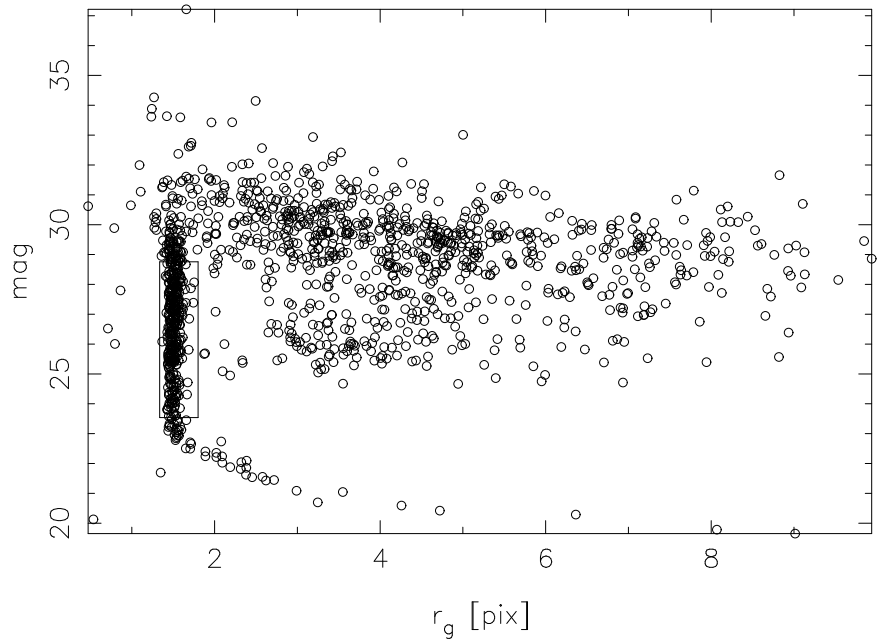

Figure 2.4: A r_g versus magnitude diagram of objects detected in the field of PSZ1 G311.65–18.48. The stars in our star catalog are selected from the vertical column marked with a box in the diagram. The trailing tail of the column at low magnitudes and increasing radius, is caused by saturated stars

2.4.4 Removing the Red Sequence

It is very important that the cluster galaxies does not contribute to the shear measurements we make. If they do, the shear will be biased towards lower values.

A galaxy cluster tends to consist of red elliptical galaxies. Because they lie closer to us, they will also appear brighter, resulting in a high $\nu = S/N$. This provides us with a way of distinguishing cluster galaxies from background galaxies.

As we have images with bandpasses centered at 814 nm (V) and 606 nm (I) for two of our clusters (PSZ1 G311.65–18.48 and SDSS J1226+2152), we can plot a color-magnitude diagram, showing V-I against I. The Red sequence will then lie on an approximately straight horizontal line, which has been marked in Figure 2.6. We remove these objects, and make additional cuts in ν. As saturated stars are very bright, these cuts will also weed them out. We are then left with a catalog of only background galaxies, and moderately bright to faint stars. For the cluster SDSS J1723+3411 we find that attempting to filter it with images in infrared filters (F110W and F160W), leaves us with very few objects, too few to run a proper weak lensing analysis. We therefore decide to settle with only making cuts in ν.

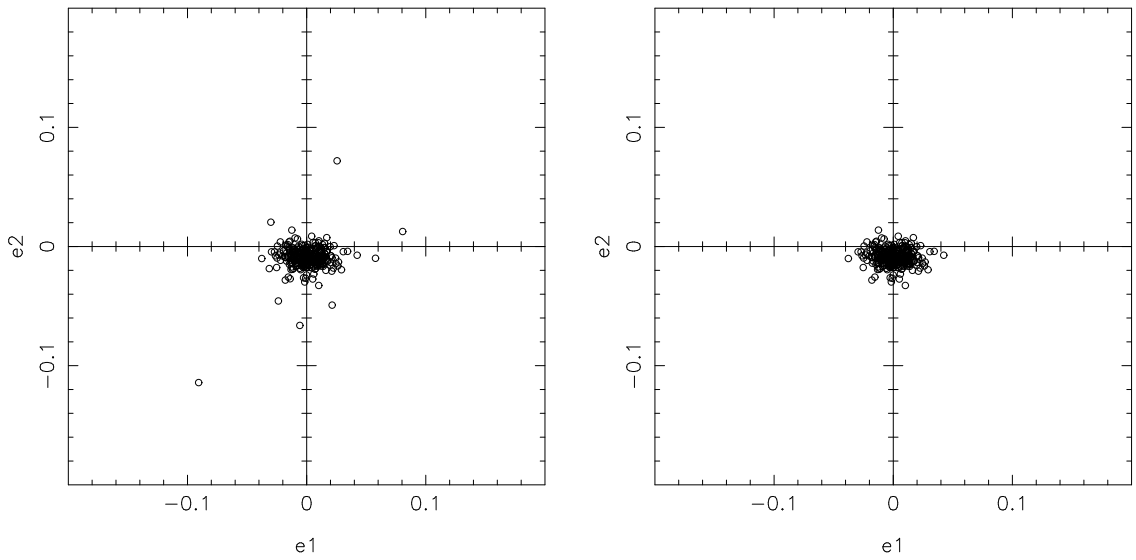

Figure 2.5: e_1 versus e_2 plot of stars in the foreground of PSZ1 G311.65–18.48, in the F814W filter. The image to the left shows our initial pick of stars from the star-column in Figure 2.4. In the figure to the right, we have excluded objects with a high ellipticity, which could be galaxies.

2.4.5 Measuring shear and mass reconstruction

We now have a catalog of stars and a catalog of stars + background galaxies. The first step is to estimate the anisotropy of the PSF, as described in Section 2.3.1. We use the star catalog for this.

The mean radius in the star catalog is used to mark the lower limit in radius of the grid we separate the background galaxies into. We then make sure to not include stars when estimating $P^{\rm sm}$ and $P^{\rm sh}$ of the sources, which would bias our shear estimates towards smaller values.

Once we have corrected for the PSF anisotropy with `efit` and `ecorrect`, we calculate the reduced weighted shear $g_{\rm w}$, and the mean weighted angular diameter distance ratio $\beta_{\rm w}$ in each bin, according to Section 2.3.2 and 2.3.3.

Next, we use `etprofile` to separate our field into radial bins, and calculate the mean reduced tangential shear, $\langle g_{\rm w,T} \rangle$, and ζ-statistic, which gives us a lower bound estimate of the convergence within some radius. From this, we can calculate the 2D projected aperture mass of the field. This is described in Section 2.3.4. The boundaries of the fields of our three clusters, can be found in Table 2.1.

The last thing to do, is to fit our data to a theoretical density profile, and obtain a mass estimate according to this. This is the subject of the next section, Section 2.5.

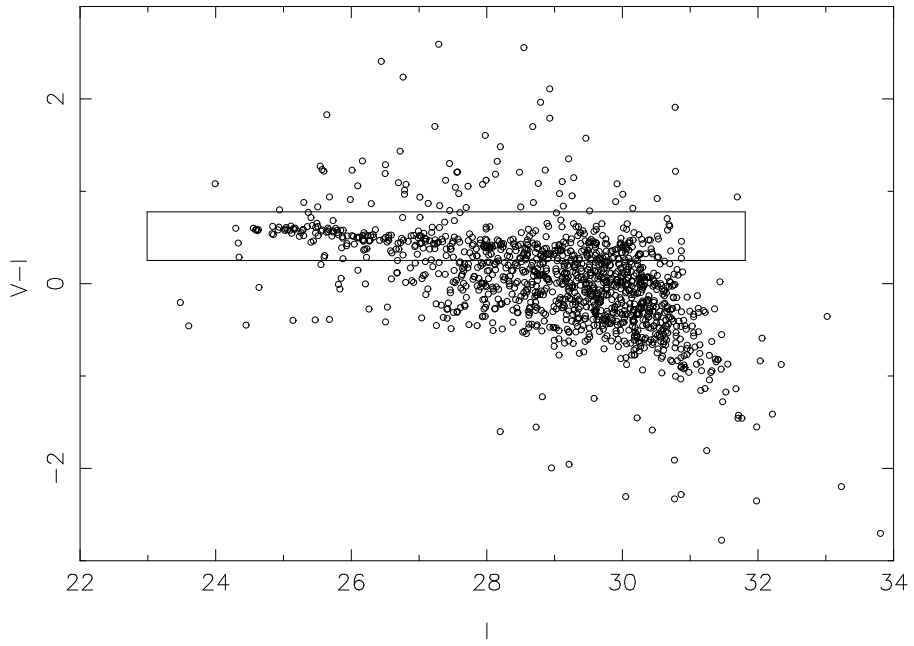

Figure 2.6: The objects detected in the field of SDSS J1226+2152 are plotted in a color magnitude diagram. We have an image in two filters, F606W (V) and F814W (I). On the x-axis we show the I magnitudes, on the y-axis, we have the subtracted magnitudes V-I. The cluster galaxies make up the red sequence, which is shown in the box.

Table 2.1: The parameter values that we feed to `etprofile` to calculate the tangential shear, and the statistic ζ within several annuli, along with error estimates and the mean radius of each annuli. The innermost annulus has an inner radius of $r_{\rm inner} = \frac{3}{2}\theta_{\rm E}$, while the outermost annulus has an outer radius of $r_{\rm outer}$. Hence, these radii mark the boundaries of our field. The width of the annuli is log spaced. `etprofile` also needs the center of our fields, found in Table 1.1.

	$r_{\rm inner}$ [arcsec]	$r_{\rm outer}$ [arcsec]	width
PSZ1 G311.65–18.48	43.937	88.525	0.18
SDSS J1226+2152	17.290	72.180	0.50
SDSS J1723+3411	13.631	82.494	0.70

2.5 Fitting to density profiles

Now that we have found the observed mean reduced tangential shear, $\langle g_{\rm w,T}\rangle$, over several annuli in our fields, we can fit the data points to the theoretical reduced shear,

$g_{\rm T}^{\rm model}$, calculated from different density profiles.

While different density profiles have been used to describe galaxy clusters and dark matter halos, we will focus on two: The Navarro-Frenk-White profile, and the singular isothermal sphere density profile.

We do the fitting by calculating the χ^2- statistic, where we compare $\langle g_{\rm w,T}\rangle$ at the mean radius of the annuli, for each annulus bin obtained from our data, with $g_{\rm T}^{\rm model}$ from the density profiles at the same radius,

$$\chi^2 = \frac{(\langle g_{\rm T}\rangle - g_{\rm w,T}^{\rm model})^2}{\sigma_g^2}. \tag{2.39}$$

Here, σ_g are the errors in the $\langle g_{\rm T}\rangle$ estimates from `etprofile`.

The parameter(s) that minimize χ^2, are the ones we use to calculate the mass of the clusters. The way this is done depends on the density profile we employ, and is expanded upon in the next two subsections 2.5.1 and 2.5.2. We also calculate the aperture mass, $M_{\rm ap}$ at the inner radius $\theta_{\rm inner}$, according to equation 2.37.

2.5.1 The Singular isothermal sphere

The simplest lens model used in gravitational lensing, is that of a singular isothermal sphere (SIS). It provides a good fit with the lensing properties of galaxies and galaxy clusters, and it also yields flat rotation curves, as those observed in spiral galaxies.

In this model, we assume that stars and gas behave as particles in an ideal gas, confined by their combined spherically symmetric gravitational potential. The particles have a Maxwellian velocity distribution at all radii, with a one-dimensional velocity dispersion, σ_v.

The mass density of a singular isothermal sphere at radius r, is given by

$$\rho_{\rm SIS}(r) = \frac{\sigma_v^2}{2\pi G}\frac{1}{r^2}. \tag{2.40}$$

The projected surface mass density is

$$\Sigma_{\rm SIS}(\xi) = \frac{\sigma_v^2}{2G}\frac{1}{\xi}, \tag{2.41}$$

which is circularly symmetric. We repeat that $\xi = D_{\rm l}\theta$ is the projected two-dimensional radius in the lens plane, where $D_{\rm l}$ is the angular diameter distance between the observer and the lens, and θ is the angular radius from the center of the lens in the lens plane.

The projected mass along the line-of-sight is

$$M_{\rm 2D}(\xi) = \frac{\pi\sigma^2}{G}\xi \tag{2.42}$$

while the mass enclosed within the 3D-radius r is

$$M_{\rm 3D}(r) = \frac{2\sigma^2}{G}r. \tag{2.43}$$

The Einstein radius then becomes

$$\theta_{\rm E} = 4\pi \left(\frac{\sigma_v}{c}\right)^2 \frac{D_{\rm ls}}{D_{\rm s}}, \tag{2.44}$$

where c is the speed of light, $D_{\rm ls}$ and $D_{\rm s}$ are the angular diameter distance between the lens and the source, and the observer and the source, respectively.

In the case of a SIS profile, the convergence and the shear have the same magnitude;

$$\kappa_{\rm SIS}(\theta) = \gamma_{\rm SIS}(\theta) = \frac{\theta_{\rm E}}{2\theta} = \frac{1}{2\Sigma_{\rm crit}} \frac{\sigma_v^2}{G\xi} \tag{2.45}$$

The reduced shear is found in the normal way, $g = \gamma/(1-\kappa)$. As the SIS is a spherically symmetric model, these expressions for shear and reduced shear, are also the *tangential* shear, $\gamma_{\rm T}$, and reduced shear, $g_{\rm T}$. We see that at the Einstein radius, $\kappa_{\rm SIS} = \gamma_{\rm SIS} = \frac{1}{2}$, and $g_{\rm SIS} = 1$.

The deflection angle becomes

$$\hat{\alpha} = 4\pi \frac{\sigma_v^2}{c^2}, \tag{2.46}$$

which is independent of ξ, and thereby constant. This makes the reduced deflection angle equal to the Einstein radius

$$\alpha = \frac{D_{\rm ls}}{D_{\rm s}} \hat{\alpha} = \theta_{\rm E}. \tag{2.47}$$

Numerical fitting

We have two different ways of fitting the SIS-profile to our data. The first is by calculating the $\zeta(\theta_1, \theta_2)$-statistic and calculate the mass directly from that. In which case, we have a formula for how much ζ underestimates the true mean dimensionless surface mass density, $\bar{\kappa}(\theta < \theta_1)$.

If we assume a surface density profile that goes as $\Sigma \propto \xi^{-\tau}$ where $\tau > 0$, the underestimation made by the ζ-statistic, of the actual mean surface density within θ_1, is

$$k^{-1} = \frac{\zeta(\theta_1, \theta_2)\Sigma_{\rm crit}}{\overline{\Sigma}(\theta < \theta_1)} = \frac{a^2 - a^{-\tau+2}}{a^2 - 1}, \tag{2.48}$$

where $a = \frac{\theta_2}{\theta_1}$ (Kaiser et al. 1994). If we assume a surface density profile that goes as the profile of a singular isothermal sphere, $\Sigma \propto \xi^{-1}$, then $\tau = 1$, and

$$k^{-1} = \frac{\zeta\Sigma_{\rm crit}}{\overline{\Sigma}} = \frac{a^2 - a}{a^2 - 1}. \tag{2.49}$$

The projected 2D mass within $\xi_1 = D_{\rm l}\theta_1$, is then

$$M(\xi_1) = k \cdot \pi\xi^2 \zeta(\xi_1, \xi_2)\Sigma_{\rm crit} \tag{2.50}$$

while the 3D mass is $M(r_1) = M(\xi_1) \cdot 2/\pi$.

The other way of doing it, is by using the χ^2-test. The SIS model only has one free parameter; the velocity dispersion σ_v. To fit the model to our data, we compare the reduced shear obtained from the data with the reduced shear calculated from the density profile for different σ_v values, with a spacing of $\Delta\sigma_v = 0.1$. We then calculate the χ^2-statistic, and go forward with the σ_v value that minimizes χ^2.

Errors may arise when fitting a circular mass density profile to ζ, as the true density profile of the cluster, need not be circular. Nevertheless, when fitting a circular profile, where ζ has been measured from irregular clusters, or clusters undergoing a merger, this effect has been measured to be less than 10% (King et al. 2004).

2.5.2 NFW density profile

By studying numerical N-body simulations, Navarro et al. (1997) found that within the virial radius, $r_{\rm vir}$, cold dark matter halos over a wide range in mass (from that of a globular cluster, to that of large galaxy clusters), appear to have a universal density profile. This density profile provides a much better fit than that of an isothermal sphere. The Navarro–Frenk–White (NFW) profile goes as $\rho \propto r^{-1}$ at small radii and $\rho \propto r^{-3}$ at large radii, so it approaches the form of an isothermal sphere when r gets large.

Given that galaxy clusters are thought to be dominated by dark matter, it seems reasonable to think that their spherically averaged density profiles will be well approximated by the Navarro–Frenk–White (NFW) profile.

It is given by

$$\rho_{\rm NFW}(r) = \frac{\delta_{\rm c}\rho_{\rm crit}(z_{\rm l})}{(r/r_{\rm s})(1+r/r_{\rm s})^2}, \tag{2.51}$$

where $\rho_{\rm crit} = \frac{3H^2(z_{\rm l})}{8\pi G}$ is the critical density of the Universe at the halo redshift, here the lens redshift, $z_{\rm l}$. The scaled radius

$$r_s = \frac{r_\Delta}{c_\Delta} \tag{2.52}$$

and the dimensionless density

$$\delta_{\rm c} = \frac{\Delta}{3}\frac{c_\Delta^3}{\ln(1+c_\Delta) - c_\Delta/(1+c_\Delta)}, \tag{2.53}$$

are both characteristic quantities of the halo. The dimensionless number c_Δ is called the concentration parameter, and depends on the mass of the halo, being smaller for high-mass halos. The virial radius, $r_{\rm vir}$, is the radius of a sphere, here centered on a galaxy cluster, within which virial equilibrium holds. As this can be difficult to determine, a common approximation is to use the radius r_Δ, at which the mean density is some constant, Δ, times the critical density, $\rho_{\rm crit}(z_{\rm l})$. This constant depends on the cosmology of our universe model, but a much used choice is $\Delta = 200$, which is what we will use. The historical reason for this, is that in an Einstein-de Sitter universe, the virial overdensity, $\Delta = \Delta_{\rm vir}$, is well approximated by $\Delta_{\rm vir} \approx 200$. For other universe models, $\Delta_{\rm vir}$ is generally different from 200. Then, $c_\Delta = c_{200}$ and $r_\Delta = r_{200}$, which is the radius at which the mean mass density of the halo is $200\rho_{\rm crit}(z_{\rm l})$, independent of cosmology. The scaled radius is then $r_{\rm s} = r_{200}/c_{200}$.

The mass of a NFW cluster at radius r_{200} is then,

$$M_{200} = M(r_{200}) = 200\rho_{\text{crit}}(z_{\text{l}})\frac{4\pi r_{200}^3}{3}. \tag{2.54}$$

The shear of a NFW halo is

$$\gamma_{\text{NFW}}(x) = \frac{\overline{\Sigma}_{\text{NFW}}(x) - \Sigma_{\text{NFW}}(x)}{\Sigma_{\text{crit}}}, \tag{2.55}$$

where $x = \frac{\xi}{r_{\text{s}}}$ is a dimensionless radius, and $\xi = D_{\text{l}}\theta$ is the projected two-dimensional radius in the lens plane. Due to the spherical symmetry of the NFW model, $\gamma = \gamma_{\text{T}}$. Σ_{NFW} is still the surface mass density, and $\overline{\Sigma}_{\text{NFW}}$ is the mean surface mass density inside a radius x. The full expressions for Σ_{NFW} and $\overline{\Sigma}_{\text{NFW}}$, can be found in Wright and Brainerd (2000).

The convergence is found in the normal way,

$$\kappa_{\text{NFW}}(x) = \frac{\Sigma_{\text{NFW}}(x)}{\Sigma_{\text{crit}}}, \tag{2.56}$$

and the reduced shear is still $g = \gamma/(1-\kappa)$.

The $c - M$ relation

The mass of a galaxy cluster is correlated with the concentration parameter c_Δ. What the exact relation between them has been found to be, have varied between studies (Bullock et al. 2001; Duffy et al. 2008; Bhattacharya et al. 2013), but it depends also on the redshift of the cluster.

We have chosen to use the relation found by Duffy et al. (2008), given by

$$c_\Delta = A\left(\frac{M_\Delta}{M_{\text{pivot}}}\right)^B (1+z)^C. \tag{2.57}$$

For a full halo model, which includes halos that are both relaxed and dynamically unstable, with $M_\Delta = M_{200}$, $c_\Delta = c_{200}$ and a redshift z between 0 and 2, $A = 5.71 \pm 0.12$, $B = -0.084 \pm 0.006$, and $C = -0.47 \pm 0.04$. Also, $M_{\text{pivot}} = 2 \cdot 10^{12} h^{-1} M_\odot$.

We see that this requires some prior knowledge of the approximate mass of the cluster, M_{200}. What we will do is run two analyses per image and filter: One where both c_{200} and r_{200} are free parameters, and one where we use the mass obtained from the previous run, as M in Equation 2.57. In the second analysis we keep c_{200} fixed, leaving r_{200} as the only free parameter. In general, galaxy clusters have a mass around $M_{200} \sim 10^{14} - 10^{15} M_\odot$. From this, we find that for redshifts $z \approx 0.44$, we should expect a concentration parameter around $c_{200} \approx 3.5 \pm 0.2 - 2.9 \pm 0.2$.

Numerical fitting

We have maximum two free parameters, the virial radius r_{200}, and the concentration parameter c_{200}. We need to find the appropriate values of r_{200} and c_{200} that makes the

NFW profile best fit our data. We do this by first setting up a grid of r_{200} and c_{200} values.

Initially, the distance between grid values is $\Delta r_{200} = \Delta c_{200} = 0.1$, but as we narrow down the search area, we make the grid finer by putting $\Delta r_{200} = 0.01$. The fields we are working on are not that large, making it difficult to determine c_{200} with greater precision, so we do not make a finer grid for c_{200} (see figures 3.1-3.3).

We then find the tangential shear, $\gamma_{\rm NFW}$, the surface density, $\Sigma_{\rm NFW}$, and the characteristic density δ_c which correspond to the chosen pair of parameter values.

These values have been pre-calculated for different $x = \frac{\xi}{r_{\rm s}}$ and c_{200} values, and for a general halo profile with different inner slopes α (Jing and Suto 2000),

$$\rho(r) = \frac{\delta_{\rm c}\rho_{\rm crit}}{(\frac{r}{r_{\rm s}})^{\alpha}(1+\frac{r}{r_{\rm s}})^{3-\alpha}} \quad \text{and} \quad \delta_{\rm c} = \frac{20}{3}\left[\int_0^1 x^2(cx)^{-\alpha}(1+cx)^{\alpha-3}\,{\rm d}x\right]^{-1}, \tag{2.58}$$

where $\alpha = 1$ reduces these expressions to those of the NFW profile.

For every combination of r_{200} and c_{200} pairs in the grid, the statistic χ^2 is calculated. The best-fit values of these parameters are found by minimizing χ^2. As stated previously, once found, we make the grid smaller but finer around these values, and find the r_{200} and c_{200} pair that minimizes χ^2 again.

Once r_{200} and c_{200} are found, we can calculate the mass of the cluster at the virial radius by using the expression for M_{200} found in Equation 2.54.

When this is done, we use M_{200} in Equation 2.57 to find an estimate of c_{200}, and run the analysis again, this time with only r_{200} as a free parameter.

SIS profile comparison

We can compare the mass of the cluster found when assuming a NFW density profile to be correct, with that found if we use a SIS density profile instead. We use the expression in Equation 2.51 to calculate $\rho_{\rm NFW}(r)$ at a radius used in the SIS profile calculations, which is usually smaller than r_{200}, and then finding the 3D mass in the usual fashion,

$$M_{\rm NFW}(r) = \frac{4\pi}{3}r^3\rho_{\rm NFW}(r). \tag{2.59}$$

We then calculate the mass ratio, $M_{\rm NFW}(r)/M_{\rm SIS}(r)$.

Typically, we expect the virial mass found in a NFW halo to be smaller than the virial mass found in a SIS halo. In general, the lower the mass of a NFW halo, the larger the systematic error if it is assumed to be an isothermal sphere. The size of the error is also dependent on the concentration parameter c_{200}, where a large c_{200}, results in a large error (Wright and Brainerd 2000).

However, when dealing with rich galaxy clusters, $M \sim 10^{15}M_{\odot}$, the error in the mass estimate is small, due to the NFW profile and the SIS profile being very similar at large radii.

Chapter 3

Results and discussion

Here, we present the results of our weak lensing analysis of the three clusters, PSZ1 G311.65–18.48, SDSS J1226+2152, and SDSS J1723+3411. We measure the ellipticity of background sources in their fields, in accordance with the KSB method (Kaiser et al. 1995), with the corrections of Luppino and Kaiser (1997). From this ellipticity, we find the mean reduced gravitational shear, $\langle g \rangle$ in increasing radial bins, centered on the central cluster galaxy.

Next, we fit our data to the theoretical reduced shear calculated from two density profiles: the Navarro-Frenk-White (NFW) profile (1997), and the Singular Isothermal Sphere (SIS) profile. We then obtain an estimate of the 3 dimensional mass density distribution, $\rho(r)$ of our clusters, implicitly assuming $\rho(r)$ to be spherically symmetric. The fitting is done by finding the parameters that minimize the χ^2-statistic. We then calculate the best-fit mass, with uncertainty estimates. We compare the mass estimated from these two profiles, with each other, but also with mass estimates calculated for the clusters, in previous studies. We then discuss our results, with our conclusions found in Chapter 4.

As before, where necessary, we use a flat ΛCDM cosmology with $\Omega_{\mathrm{m},0} = 0.3$ and $\Omega_{0,\Lambda} = 0.7$, and $H_0 = 100\,h\,\mathrm{km\,s^{-1}\,Mpc^{-1}}$, where $h = 0.7$.

3.1 Results

The results of our weak lensing analysis of the three clusters PSZ1 G311.65–18.48, SDSS J1226+2152, and SDSS J1723+3411 can be found in tables 3.1 and 3.2. The tables include the two-dimensional projected aperture mass, M_{ap}, and the three-dimensional mass found by fitting our data to the SIS density profile ($M_\chi(r_1)$ and $M_\kappa(r_1)$), and the NFW density profile (M_{200} and $M_{\mathrm{NFW}}(r_1)$). The best-fit parameter values that give us these estimates, (σ_v for the SIS profile, c_{200} and r_{200} for the NFW profile), along with the minimum χ^2 for each model, is also shown. As promised, we run two analyses when fitting the NFW profile to our data: One where c_{200} is a free parameter, and one where the mass obtained in the first analysis, is used to calculate a fixed c_{200}, following Duffy et al. (2008), in the second analysis.

For the two SDSS clusters, we have two additional analysis results for a fixed c_{200}. Here, c_{200} is calculated while assuming $M_{200} = 10^{14}h^{-1}M_{\odot}$, and $M_{200} = 10^{15}h^{-1}M_{\odot}$. The reason being that the c_{200} parameter, calculated for the F606W filter of SDSS J1226+2152, and for the F775W filter of SDSS J1723+3411, is unrealistically small. We call these the third, and fourth analyses.

We have also calculated the ratios between the mass according to the NFW model ($M_{\rm NFW}$), and the two masses found from the SIS profile. They are calculated at the same radius, r_1, which differs according to cluster. This is the mean radius of the innermost annulus in our fields. The value of r_1, is found in tables 3.1 and 3.2. The ratios $\varsigma = M_{\rm NFW}/M_{\rm SIS}$ (where $M_{\rm SIS}$ is M_{χ} or M_{κ}), are found in tables 3.3 and 3.4.

The joint confidence interval for our three clusters, are shown in figures 3.1, 3.2, and 3.3. The contour lines are drawn at one and two σ confidence. For two parameters, this means $\Delta\chi^2 = \chi^2 - \chi^2_{\rm min} = 2.30$ for 1σ, and $\Delta\chi^2 = 6.14$ for 2σ.

The measured, and the theoretical, mean reduced tangential shear $\langle g_{\rm T}\rangle$ as a function of the mean radius r in the annuli, are shown in figures 3.4, 3.5, and 3.6.

Table 3.1: Results of the weak lensing analysis of the PSZ1 G311.65–18.48 cluster. $M_{\rm ap}$ is the 2D projected aperture mass, $\theta_{\rm E}$ is the Einstein radius, and r_1 the mean radius of the innermost annulus. σ_v is the velocity dispersion, while M_{κ} and M_{χ} are the 3D SIS masses according to the ζ-statistic, and the χ^2-statistic, respectively. The concentration parameter c_{200}, and the radius r_{200}, are quantities of the NFW profile. M_{200} is the 3D mean mass at r_{200}. All limits are calculated from the maximum and minimum of the parameter values, within 1σ ($\chi^2_{\rm min}+1$). $M_{\rm NFW}(r_1)$ is the 3D mass from the NFW profile, calculated at r_1, where the limits are found from the maximum and minimum mass within 1σ.

Cluster	PSZ1 G311.65–18.48		
Filter	F606W		F814W
$M_{\rm ap}\,[10^{13}h^{-1}{\rm M}_{\odot}]$	9.963 ± 1.769		9.291 ± 1.374
$\theta_{\rm E}$ [arcsec]		29.291	
$r_1\,[h^{-1}{\rm Mpc}]$		0.192	
SIS			
$\sigma_v\,[{\rm km\,s^{-1}}]$	$1066.4^{+67.2}_{-74.7}$		$1010.7^{+36.1}_{-38.2}$
$M_{\kappa}(r_1)\,[10^{13}h^{-1}{\rm M}_{\odot}]$	16.127 ± 2.790		13.253 ± 2.189
$M_{\chi}(r_1)\,[10^{13}h^{-1}{\rm M}_{\odot}]$	$15.950^{+2.072}_{-2.155}$		$14.329^{+1.042}_{-1.063}$
$\chi^2_{\rm min}$	1.0613		1.2202
NFW, free c_{200}			
c_{200}	$24.2^{+0.5}_{-20.7}$		$2.4^{+14.9}_{-2.2}$
$r_{200}\,[h^{-1}{\rm Mpc}]$	$0.87^{+0.52}_{-0.06}$		$1.55^{+2.18}_{-0.69}$
$M_{200}\,[10^{14}h^{-1}{\rm M}_{\odot}]$	$2.432^{+7.488}_{-0.469}$		$13.755^{+177.936}_{-11.406}$
$M_{\rm NFW}(r_1)\,[10^{13}h^{-1}{\rm M}_{\odot}]$	$2.539^{+2.433}_{-0.450}$		$4.661^{+0.608}_{-2.140}$

$\chi^2_{\rm min}$	0.8543	0.5320
NFW, fixed c_{200}		
c_{200}	3.1	2.8
$r_{200}\,[h^{-1}{\rm Mpc}]$	$1.44^{+0.15}_{-0.12}$	$1.45^{+0.11}_{-0.12}$
$M_{200}\,[10^{14}h^{-1}{\rm M}_\odot]$	$11.030^{+3.818}_{-2.534}$	$11.261^{+2.762}_{-2.571}$
$M_{\rm NFW}(r_1)\,[10^{13}h^{-1}{\rm M}_\odot]$	$4.813^{+0.808}_{-0.627}$	$4.602^{+0.544}_{-0.580}$
$\chi^2_{\rm min}$	1.9770	0.5481

Table 3.2: The results of our weak lensing analysis of the clusters SDSS J1226+2152 and SDSS J1723+3411. c^{14}_{200} and c^{15}_{200}, are the concentration parameter calculated from $M_{200} = 10^{14}M_\odot$, and $M_{200} = 10^{15}M_\odot$, respectively. For further explanation of the parameters, look in the description of Table 3.1. Note the different units of the masses $M_{\rm ap}$ and $M(r_1)$ (SIS and NFW), in this table compared to in Table 3.1.

Cluster	SDSS J1226+2152		SDSS J1723+3411
Filter	F606W	F814W	F775W
$M_{\rm ap}\,[10^{12}h^{-1}{\rm M}_\odot]$	3.726 ± 4.259	3.010 ± 4.387	10.324 ± 3.551
$\theta_{\rm E}$ [arcsec]	11.527		9.087
$r_1\,[h^{-1}{\rm Mpc}]$	0.087		0.074
SIS			
$\sigma_v\,[{\rm km\,s^{-1}}]$	$301.2^{+163.4}_{-300.2}$	$323.0^{+158.0}_{-322.0}$	$518.9^{+92.2}_{-121.4}$
$M_\kappa(r_1)\,[10^{12}h^{-1}{\rm M}_\odot]$	4.309 ± 10.075	7.618 ± 9.932	15.056 ± 8.001
$M_\chi(r_1)\,[10^{12}h^{-1}{\rm M}_\odot]$	$5.761^{+7.942}_{-5.761}$	$6.625^{+8.066}_{-6.625}$	$14.510^{+5.614}_{-5.995}$
$\chi^2_{\rm min}$	0.5323	0.0172	4.8029
NFW, free c_{200}			
c_{200}	$0.2^{+24.6}_{-0.0}$	$21.8^{+3.0}_{-21.6}$	$0.4^{+3.9}_{-0.0}$
$r_{200}\,[h^{-1}{\rm Mpc}]$	$0.99^{+0.75}_{-0.90}$	$0.29^{+1.41}_{-0.20}$	$2.18^{+0.11}_{-1.48}$
$M_{200}\,[10^{14}h^{-1}{\rm M}_\odot]$	$3.551^{+15.727}_{-3.548}$	$0.089^{+17.890}_{-0.087}$	$38.314^{+6.097}_{-37.045}$
$M_{\rm NFW}(r_1)\,[10^{12}h^{-1}{\rm M}_\odot]$	$2.259^{+2.126}_{-2.223}$	$1.031^{+3.086}_{-0.996}$	$4.501^{+1.839}_{-1.123}$
$\chi^2_{\rm min}$	0.2478	0.0002	1.8167
NFW, fixed c_{200}			
c_{200}	3.1	4.3	2.6
$r_{200}\,[h^{-1}{\rm Mpc}]$	$0.40^{+0.23}_{-0.39}$	$0.36^{+0.19}_{-0.35}$	$0.92^{+0.18}_{-0.21}$
$M_{200}\,[10^{14}h^{-1}{\rm M}_\odot]$	$0.234^{+0.681}_{-0.234}$	$0.171^{+0.438}_{-0.171}$	$2.880^{+2.043}_{-1.556}$
$M_{\rm NFW}(r_1)\,[10^{12}h^{-1}{\rm M}_\odot]$	$1.935^{+2.254}_{-1.935}$	$1.727^{+2.160}_{-1.723}$	$5.126^{+1.365}_{-1.545}$
$\chi^2_{\rm min}$	0.4216	0.0350	2.2430

NFW, fixed c_{200}^{14}			
c_{200}		3.5	3.5
$r_{200}\,[h^{-1}\mathrm{Mpc}]$	$0.39^{+0.21}_{-0.29}$	$0.38^{+0.21}_{-0.29}$	$0.82^{+0.12}_{-0.20}$
$M_{200}\,[10^{14}h^{-1}\mathrm{M}_\odot]$	$0.217^{+0.573}_{-0.214}$	$0.201^{+0.551}_{-0.198}$	$2.039^{+1.033}_{-1.158}$
$M_{\mathrm{NFW}}(r_1)\,[10^{12}h^{-1}\mathrm{M}_\odot]$	$1.917^{+2.199}_{-1.844}$	$1.825^{+2.176}_{-1.752}$	$5.379^{+1.183}_{-1.875}$
χ^2_{min}	0.4427	0.0487	2.5145
NFW, fixed c_{200}^{15}			
c_{200}		2.9	2.9
$r_{200}\,[h^{-1}\mathrm{Mpc}]$	$0.38^{+0.27}_{-0.37}$	$0.37^{+0.26}_{-0.36}$	$0.87^{+0.17}_{-0.19}$
$M_{200}\,[10^{14}h^{-1}\mathrm{M}_\odot]$	$0.201^{+0.804}_{-0.201}$	$0.185^{+0.730}_{-0.185}$	$2.435^{+1.725}_{-1.272}$
$M_{\mathrm{NFW}}(r_1)\,[10^{12}h^{-1}\mathrm{M}_\odot]$	$1.935^{+2.254}_{-1.935}$	$1.646^{+2.397}_{-1.646}$	$5.135^{+1.420}_{-1.530}$
χ^2_{min}	0.4156	0.0586	2.3400

Table 3.3: Comparison of the SIS masses (M_{SIS}) $M_\kappa(r_1)$ and $M_\chi(r_1)$, with $M_{\mathrm{NFW}}(r_1)$. $\varsigma = M_{\mathrm{NFW}}/M_{\mathrm{SIS}}$ is the ratio between the NFW mass and the SIS mass. The subscript, κ or χ, indicates the ratio with respect to $M_\kappa(r_1)$, or $M_\chi(r_1)$, respectively. The superscript "fr", indicates that the values are for a free c_{200}. The superscript "fix" indicates the values are for a fixed c_{200}

Cluster	PSZ1 G311.65–18.48	
Filter	F606W	F814W
$\varsigma_\kappa^{\mathrm{fr}}(r_1)$	$0.192^{+0.449}_{-0.135}$	$0.352^{+0.476}_{-0.163}$
$\varsigma_\chi^{\mathrm{fr}}(r_1)$	$0.159^{+0.360}_{-0.116}$	$0.325^{+0.397}_{-0.164}$
$\varsigma_\kappa^{\mathrm{fix}}(r_1)$	$0.363^{+0.508}_{-0.271}$	$0.347^{+0.465}_{-0.261}$
$\varsigma_\chi^{\mathrm{fix}}(r_1)$	$0.302^{+0.407}_{-0.232}$	$0.321^{+0.388}_{-0.262}$

Table 3.4: Comparison of the SIS masses ($M_{\rm SIS}$) $M_\kappa(r_1)$ and $M_\chi(r_1)$, with $M_{\rm NFW}(r_1)$. $\varsigma = M_{\rm NFW}/M_{\rm SIS}$ is the ratio between the NFW mass and the SIS mass. The subscript, κ or χ, indicates the ratio with respect to $M_\kappa(r_1)$, or $M_\chi(r_1)$, respectively. The superscript "fr", indicates that the values are for a free c_{200}. The superscript "fix" indicates the values are for a fixed c_{200}. The superscript 14 or 15 means the ratio is calculated for c_{200}^{14} or c_{200}^{15}, respectively.

Cluster	SDSS J1226+2152		SDSS J1723+3411
Filter	F606W	F814W	F775W
$\varsigma_\kappa^{\rm fr}(r_1)$	$0.296^{+57547.381}_{-0.002}$	$0.135^{+54050.198}_{-0.002}$	$0.299^{+0.899}_{-0.147}$
$\varsigma_\chi^{\rm fr}(r_1)$	$0.392^{+69043.804}_{-0.003}$	$0.156^{+64847.977}_{-0.002}$	$0.310^{+0.745}_{-0.168}$
$\varsigma_\kappa^{\rm fix}(r_1)$	$0.254^{+54989.074}_{-0.000}$	$0.227^{+51020.894}_{-0.000}$	$0.340^{+0.920}_{-0.155}$
$\varsigma_\chi^{\rm fix}(r_1)$	$0.336^{+65974.415}_{-0.000}$	$0.261^{+61213.499}_{-0.000}$	$0.353^{+0.762}_{-0.178}$
$\varsigma_\kappa^{14}(r_1)$	$0.252^{+54016.835}_{-0.004}$	$0.240^{+52515.267}_{-0.004}$	$0.357^{+0.930}_{-0.152}$
$\varsigma_\chi^{14}(r_1)$	$0.333^{+64807.949}_{-0.005}$	$0.276^{+63006.408}_{-0.005}$	$0.371^{+0.771}_{-0.174}$
$\varsigma_\kappa^{15}(r_1)$	$0.227^{+55742.173}_{-0.000}$	$0.216^{+53080.005}_{-0.000}$	$0.341^{+0.929}_{-0.156}$
$\varsigma_\chi^{15}(r_1)$	$0.300^{+66877.965}_{-0.000}$	$0.249^{+63683.965}_{-0.000}$	$0.354^{+0.770}_{-0.179}$

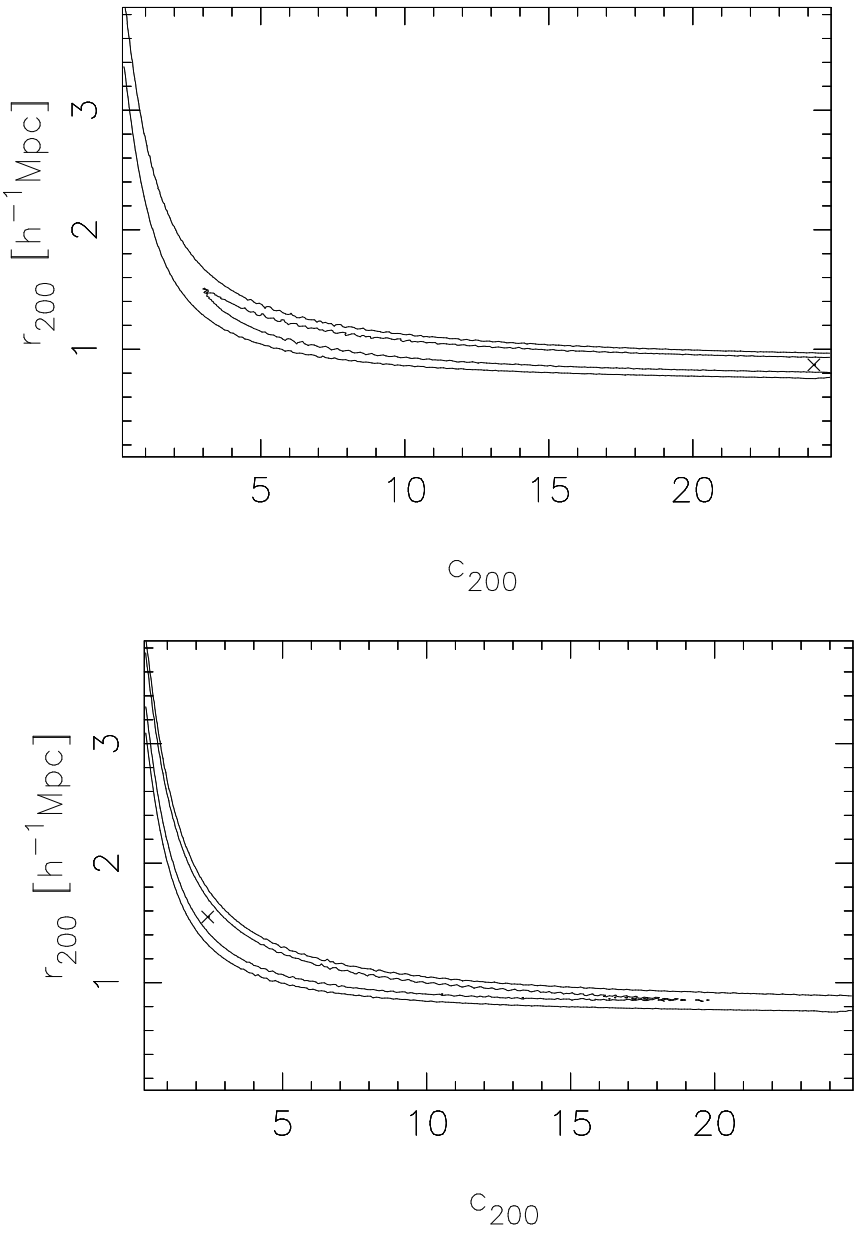

Figure 3.1: Joint confidence interval for r_{200} and c_{200} for galaxy cluster PSZ1 G311.65-18.48 . First frame is for the F606W filter, while the second is for the F814W filter. The outermost contour marks values within 2σ ($\Delta\chi^2 = 6.14$), while the innermost marks values within 1σ ($\Delta\chi^2 = 2.30$).The best-fit values have been marked with a $\times$.

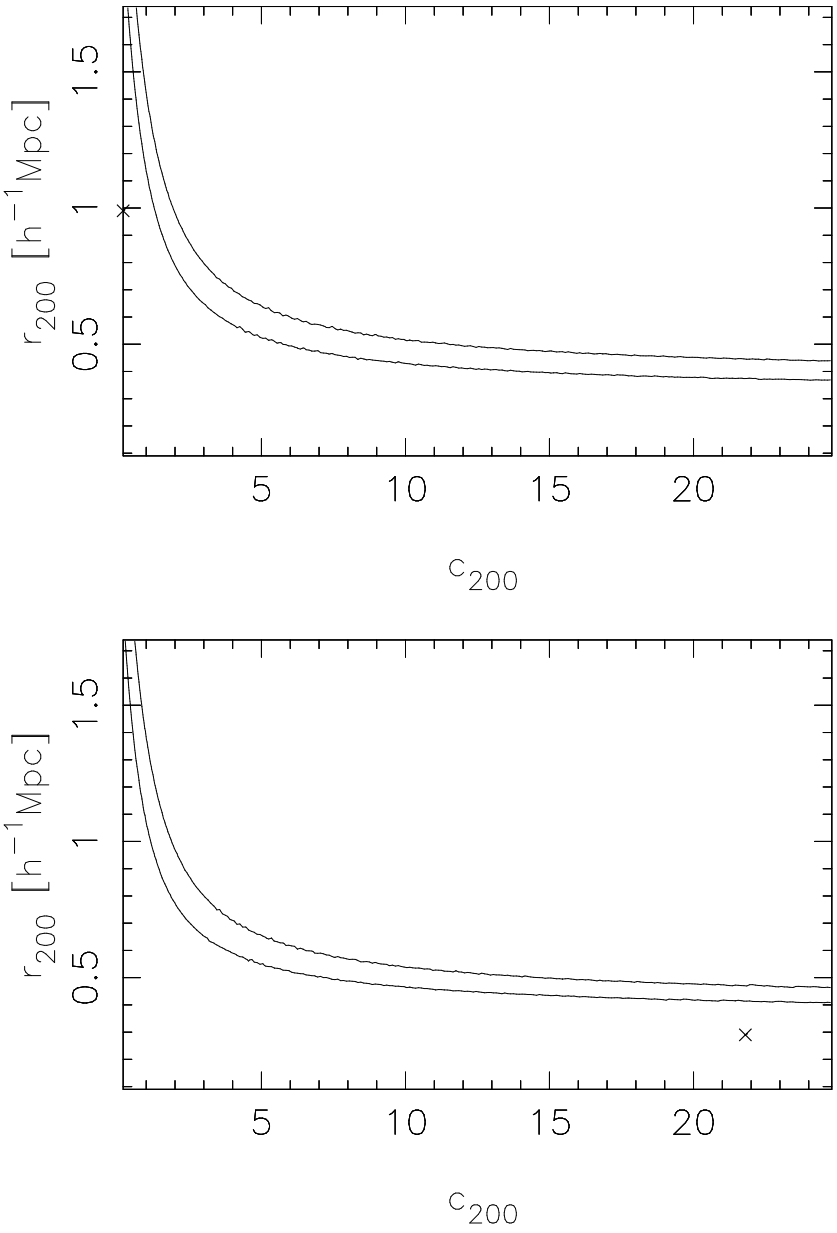

Figure 3.2: Joint confidence interval for r_{200} and c_{200} for galaxy cluster SDSS J1226+2152. First frame is for the F606W filter, while the second is for the F814W filter. Values within 2σ ($\Delta\chi^2 = 6.14$), lie below the topmost line, while the values within 1σ ($\Delta\chi^2 = 2.30$) lies below the lowest line. The other side of the contour then lies beneath the x-axis, at very low r_{200} values. The best-fit values have been marked with a $\times$.

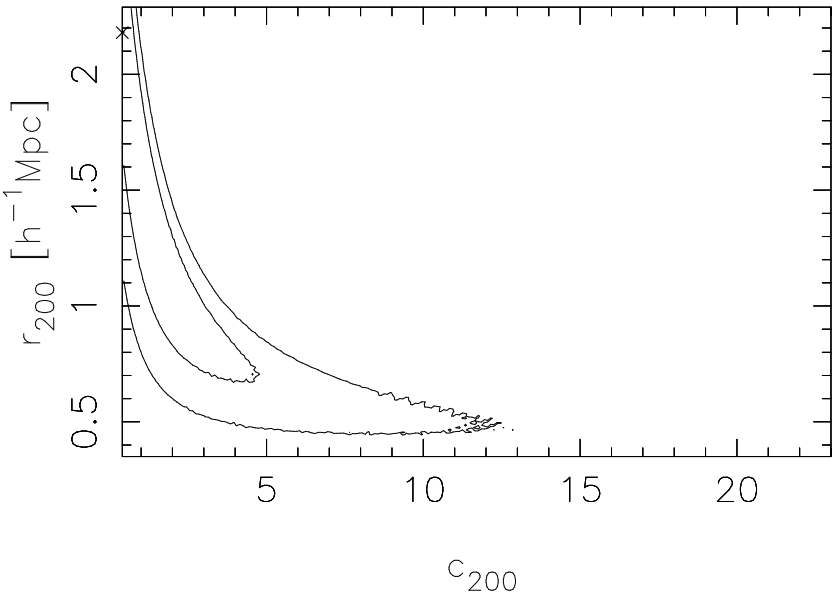

Figure 3.3: Joint confidence interval for r_{200} and c_{200} for galaxy cluster SDSS J1723+3411. The filter is F775W. The outermost contour marks values within 2σ ($\Delta\chi^2 = 6.14$), while the innermost marks values within 1σ ($\Delta\chi^2 = 2.30$). The best-fit values have been marked with a $\times$.

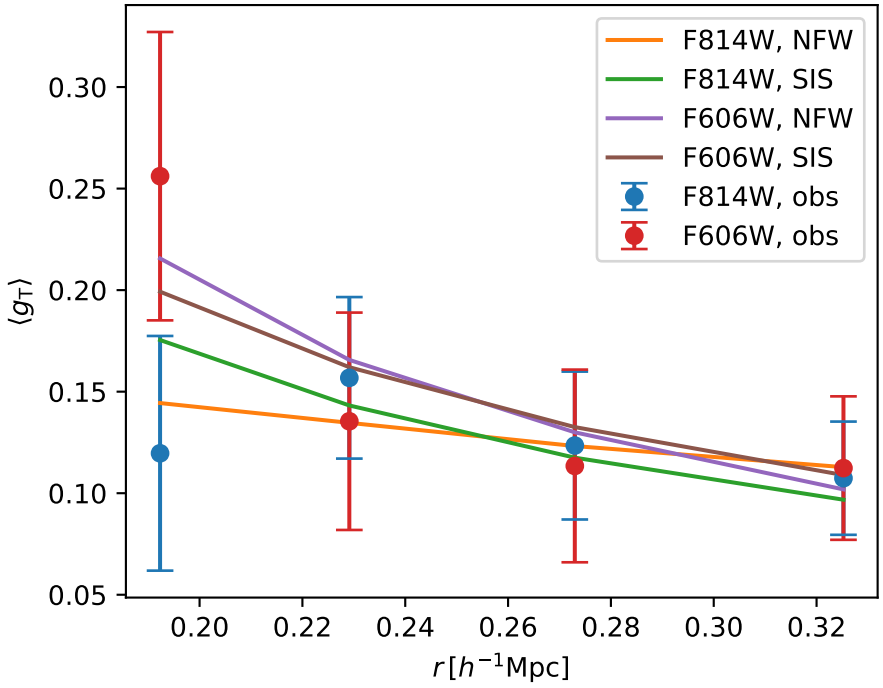

Figure 3.4: The mean measured tangential shear, $\langle g_{\mathrm{T}} \rangle$ with errors for the two images in filters F606W and F814W for the cluster PSZ1 G311.65-18.48. On the x-axis is the mean radii of the annuli, r, in $h^{-1}Mpc$. Also shown are the best fit calculated mean tangential shear from the NFW profile and the SIS profile. We see that the fitted profiles fit well within the error bars of their respective images. With exception of the first point, the measured shear in both images fall within the range of each others errors, and the errors decrease as r increases.

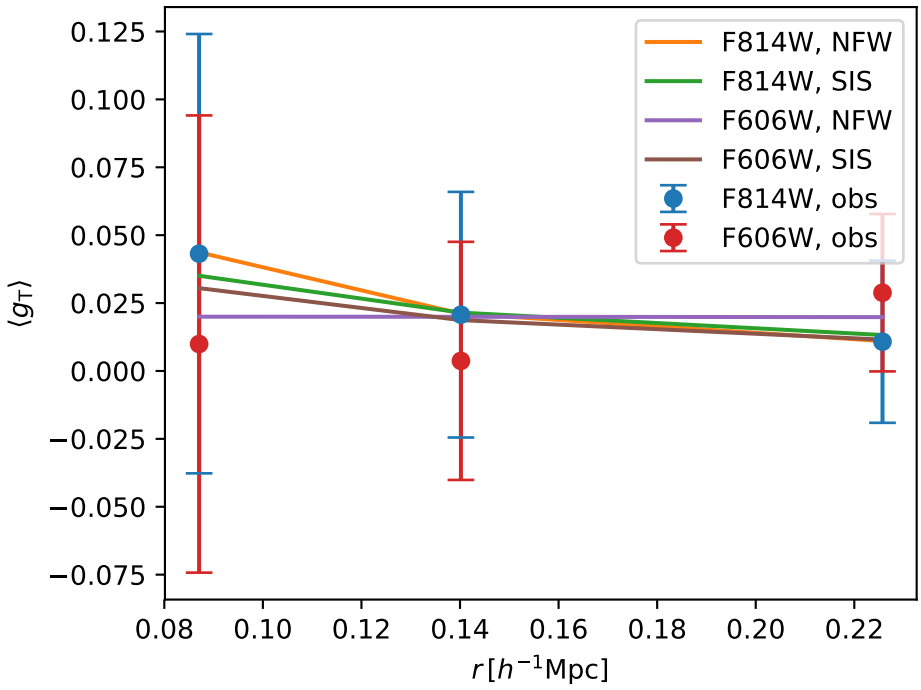

Figure 3.5: The mean measured tangential shear, $\langle g_T \rangle$ with error bars for the two images in filters F606W and F814W for the cluster SDSS J1226+2152. On the x-axis is the mean radii of the annuli, r, in $h^{-1}Mpc$. The calculated mean tangential shear according to the NFW profile and the SIS profile, is also shown. The fitted profiles fit well within the errors of the observed shear in both filters. The errors of the observed shear also overlaps, and grow smaller as r increases.

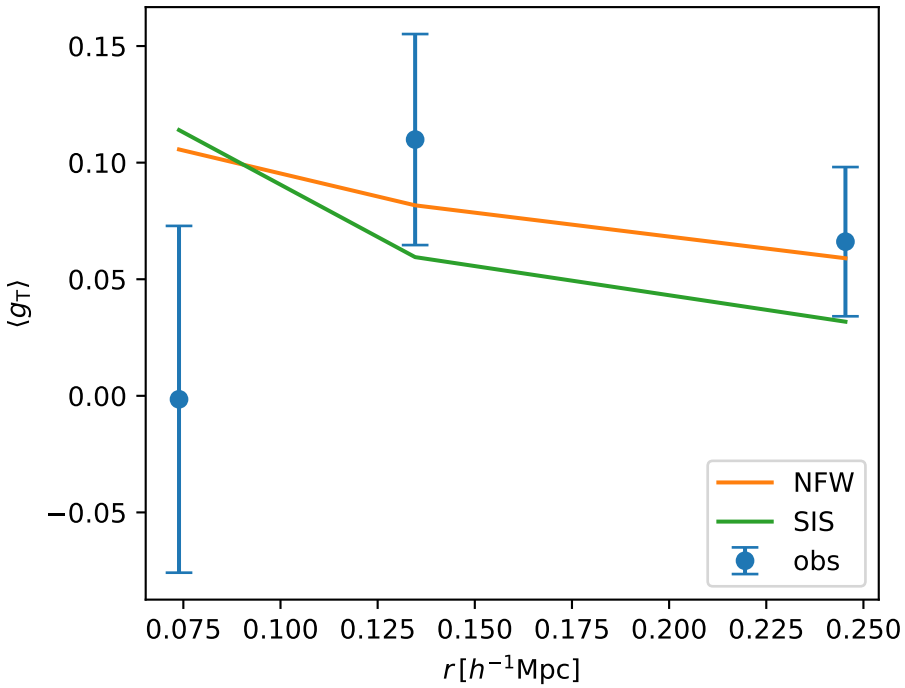

Figure 3.6: The mean measured tangential shear, $\langle g_{\mathrm{T}} \rangle$ with error bars for the cluster SDSS J1723+3411 in filter F775W. On the x-axis is the mean radii of the annuli, r, in $h^{-1}Mpc$. The calculated mean tangential shear according to the NFW profile and the SIS profile, is also shown. The fitted NFW profile, fits within the errors of the two final points, although not the first point. The SIS profile shear is not within any of the error bars, but lie close in the two final points. This is reflected in Table 3.2, where the χ^2_{min}-value for both profiles, is quite high. The errors of the observed shear grow smaller as r increases.

3.2 Discussion

We begin with the SIS model fit. The calculated SIS mass for the two methods, M_κ and M_χ, vary little within, and between, filters. This goes for all clusters, with the masses lying well within each others limits of uncertainty.

For SDSS J1226+2152, we can see from Table 3.1, that there is very large uncertainty in the σ_v and mass estimates of the SIS model: The lower limit is so large, as to make σ_v, M_κ, and M_χ, almost equal to 0 at the lowest. There are several sources of error that could contribute to this uncertainty. The extremely small number of foreground stars, only 9, makes it difficult to determine the anisotropic PSF. In addition, the fields in our images are not very large, meaning we get very few measuring points to run statistics on. For the PSZ cluster, `etprofile` returns four annuli, while for the SDSS clusters, we only get three. Increasing the number of annuli, would increase the noise of the innermost annuli, as we would end up with very few galaxies in these bins. For this cluster, the number is already only 16. So the small field, and a badly determined PSF, can in turn give rise to very large uncertainty in the ellipticity measurements. However, in the case of SDSS J1226+2152, the largest source of this uncertainty, is most likely the larger, multiple-cluster structure that SDSS J1226+2152 is a part of. These other structures will contaminate the shear measurements. We see this also in the plot of mean reduced shear versus radius in Figure 3.5: The curve of the measured $\langle g_T \rangle$, stays very flat, over large radii, were normally we would expect it to fall as r increases. This is most likely also the reason the velocity dispersion is found to be as small as it is, between $\sigma_v = 301.2^{+163.4}_{-300.2}\,\mathrm{km\,s^{-1}}$ and $323.0^{+158.0}_{-322.0}\,\mathrm{km\,s^{-1}}$. For a galaxy cluster, we would expect a value around $\sigma_v \approx 1000\,\mathrm{km\,s^{-1}}$. In comparison, Bayliss et al. (2011) found through spectroscopic measurements of the cluster galaxies, that $\sigma_v = 730^{+71}_{-119}\,\mathrm{km\,s^{-1}}$. As our methods differ, and the gravitational shear will be impacted by nearby structure, the discrepancy in our results, is not unexpected.

The small velocity dispersion, in turn, cause the obtained mass to be small. While the values of M_κ and M_χ lie within each others error range, they are slightly smaller in the F606W filter than the F814W filter. These large errors, will propagate down to where we calculate the mass ratios, ς, in Table 3.4. There, the low-end mass estimate of M_χ and M_κ, makes the positive limits very large.

SDSS J1723+3411 has more foreground stars than the other SDSS cluster, and so the anisotropic PSF, could be fitted to a 6th order polynomial. The uncertainties in σ_v, are smaller than for SDSS J1226+2152. The same goes for the two masses, although the error estimates are larger for M_κ, than for M_χ. Here, $\chi^2_{\mathrm{min}} = 4.8029$, which is the largest out of all the different analyses we run. This is true for the NFW model fit as well, where $\chi^2_{\mathrm{min}} = 1.8167$. This can also be seen in Figure 3.6 as well, which shows the observed and calculated mean reduced shear, $\langle g_T \rangle$ against radius r. The fitted SIS model does not actually fit within the error-bars of the observed mean reduced shear, but it is still the closest fit we are able to find. The velocity dispersion is $518.9^{+92.2}_{-121.4}\,\mathrm{km\,s^{-1}}$. This is very close to what was found in the strong lensing analysis done by Kubo et al. (2010), where $\sigma_v = 530 \pm 17\,\mathrm{km\,s^{-1}}$.

For the last cluster, PSZ1 G311.65–18.48, we measure a velocity dispersion ly-

ing between $1010.7^{+36.1}_{-38.2}\,\mathrm{km\,s^{-1}}$, and $1066.4^{+67.2}_{-74.7}\,\mathrm{km\,s^{-1}}$. The errors of σ_v and the two masses, are quite small as well. The masses in both filters, and with both methods, lie within each others error ranges. As no previous measurements of σ_v has been done, we have nothing to compare our results with. However, for a rich galaxy cluster such as this, a $\sigma_v \approx 1000\,\mathrm{km\,s^{-1}}$, is what we would expect.

When fitting our data to the NFW profile, we find that the best-fit parameters are difficult to determine, for all three clusters. This applies in particular, to the concentration parameter c_{200}, which is highly uncertain, due to the smallness of our fields. In figures 3.1, 3.2, and 3.3, the joint confidence interval of r_{200} and c_{200} for the three clusters and their various filters, can be seen. In all three cases, there is a wide range in c_{200} values, lying within 1σ.

The pre-calculated values γ_{NFW}, Σ_{NFW}, and δ_c (see Section 2.5.2), depend on both c_{200} and r_{200}. In the F606W filter of SDSS J1226+2152, and the F775W filter of SDSS J1723+3411, we can se from figures 3.3 and 3.2, that best-fit c_{200} value, is extremely low, while having a high r_{200} best-fit value. As we deem such a low concentration parameter to be unrealistic, we choose not to calculate γ_{NFW}, Σ_{NFW}, and δ_c, for any lower c_{200} and higher r_{200} pair. This is also why, in the NFW (free c_{200}) section of Table 3.2, the lower limit of c_{200}, is 0 for SDSS J1226+2152, filter F606W, and SDSS J1723+3411. Galaxy clusters typically have a mass on the order of $M_{200} \sim 10^{14} - 10^{15} M_\odot$. We therefore calculate c_{200} for the SDSS clusters (see Section 2.5.2) at $10^{15}\,h^{-1}M_\odot$ and $10^{14}\,h^{-1}M_\odot$, and use this to estimate M_{200}. We have then, a lower and higher bound mass estimate.

In our free concentration parameter analysis of SDSS J1226+2152, c_{200} have widely different values in the two filters, $c_{200} = 0.2^{+24.6}_{-0.0}$ for F606W, and $c_{200} = 21.8^{+3.0}_{-21.6}$ for F814W. The error estimates are also enormous, spanning almost the entirety of the c_{200} range we tested. The same is true for the first analysis of PSZ1 G311.65–18.48. r_{200}, while different in the two filters, lie within each others lower and higher limit, and are of the same order. However, the best-fit value in the F606W filter, $r_{200} = 0.99^{+0.75}_{-0.9}\,h^{-1}$Mpc, lies closer to the expected value of $r_{200} \sim 1\,h^{-1}$Mpc, compared to $r_{200} = 0.29^{+1.41}_{-0.20}\,h^{-1}$Mpc in the F814W filter. Due to the difference in r_{200}, between the filters, the mass, M_{200} vary greatly as well. For filter F606W, $M_{200} = 3.551^{+15.727}_{-3.548} \times 10^{14}\,h^{-1}M_\odot$, while for filter F814W, $M_{200} = 0.089^{+17.890}_{-0.2} \times 10^{14}\,h^{-1}M_\odot$.

In our second analysis, we kept c_{200} fixed. We see that the fixed c_{200}, based on Duffy et al. (2008), is quite different than the c_{200} found to be the best fit to the data. While r_{200} and M_{200} are now more similar in both filters, the latter quantity is still only on the order of $\sim 10^{13}\,h^{-1}M_\odot$. This remains true, for the third and fourth analysis as well. As stated, this is most likely due to the surrounding structure of the cluster, biasing the shear measurements towards lower values.

For SDSS J1723+3411, c_{200} in the first analysis, is very small. Meanwhile, r_{200} and M_{200} is quite large. The second analysis, gives a much more realistic concentration parameter, $c_{200} = 2.6$, and r_{200}, and M_{200} values. Still, c_{200} and r_{200} are smaller than the lower bound estimate found in the third analysis, where $c_{200} = 2.9$. However, this difference is small, and the mass and radius in the second, third, and fourth analysis,

all fit within each others error range. The lower and higher bound limits on the mass (from the third and fourth analysis), are $M_{200} = 2.039^{+1.033}_{-1.158} \times 10^{14}\, h^{-1} M_{\odot}$ and $M_{200} = 2.435^{+1.725}_{-1.272} \times 10^{14}\, h^{-1} M_{\odot}$, respectively.

In the first analysis of PSZ1 G311.65–18.48, we find that the concentration parameter varies quite a bit between the two filters. They still fit within each others limits, due to the limits being so large. For F606W, $c_{200} = 24.2^{+0.5}_{-20.7}$, while for F814W, $c_{200} = 2.4^{+14.9}_{-2.2}$. The r_{200} values are also a little different. This results in the mass being on the order of $M_{200} \sim 10^{14}\, h^{-1} M_{\odot}$ in filter F606W, but $M_{200} \sim 10^{15}\, h^{-1} M_{\odot}$ in filter F814W.

For the second analysis, we find $c_{200} = 3.1$ and $c_{200} = 2.8$, for filters F606W and F814W, respectively. Both r_{200}, and M_{200}, are now very similar across filters. The mass is $M_{200} = 11.030^{+3.818}_{-2.534} \times 10^{14}\, h^{-1} M_{\odot}$ and $M_{200} = 11.261^{+2.762}_{-2.571} \times 10^{14}\, h^{-1} M_{\odot}$, for filters F606W and F814W, respectively. This appears to be the most massive out of our three clusters.

3.2.1 Mass comparisons between models

The ratio $\varsigma = M_{\mathrm{NFW}}(r_1)/M_{\mathrm{SIS}}(r_1)$, has been calculated for our three clusters. This can be seen in Table 3.3 for PSZ1 G311.65–18.48, and Table 3.4 for the two SDSS clusters. The upper bound estimates, are found by dividing the maximum M_{NFW}, with the minimum M_{SIS}. Similarly, the lower bound estimates are found by dividing the minimum mass of M_{NFW} with the maximum mass of M_{SIS}. For M_{κ}, where the negative limit is so large, as to suggest negative mass, we put the lower limit at $M_{\kappa} \times 10^{-5}$.

For the SDSS clusters, we have included the ratios for all four analyses, but as the results are so uncertain for the two first analyses, we will focus on the last two. This gives us a maximum lower and upper boundary for the mass ratios.

For SDSS J1226+2152, the ratios vary between 0.240 and 0.333. The huge positive-, and small negative error estimates, come from the very small lower bound mass in Table 3.2, which is only on the order of $10^7\, h^{-1} M_{\odot}$.

For SDSS J1723+3411, the ratios seem to lie between 0.357, and 0.371. They are slightly larger for M_{κ}, than M_{χ}.

The ratios of PSZ1 G311.65–18.48, have a similar value. For a fixed c_{200}, $\varsigma_{\kappa} = 0.347^{+0.465}_{-0.261} - 0.365^{+0.508}_{-0.271}$, and $\varsigma_{\chi} = 0.302^{+0.407}_{-0.232} - 0.321^{+0.388}_{-0.262}$.

As expected, we derive a larger mass from the SIS profile, than from the NFW profile. By showing the shear for both models, as a function of radius, as seen in figures 3.4-3.6, we find that the NFW profile, seem to fit our data the best, regardless of filter and cluster. From looking at the tables 3.3 and 3.4, we therefore say that the SIS model, errors included, may underestimate the mass by a factor of 0.78 at the most, or overestimate it at most, by a factor of 7.4. We here exclude the enormous positive limit of the ratios for SDSS J1226+2152. If we only consider the ratios for the third and fourth analysis of the SDSS clusters, and the second analysis of the PSZ cluster, the best-fit NFW profile mass estimate values, are, approximately, 0.4 to 0.3 that of the SIS profile estimates.

3.2.2 Mass comparisons with earlier works

Our three clusters, have all previously undergone strong lensing analyses, by different authors.

For SDSS J1226+2152, Bayliss et al. (2011) did not calculate the mass of this individual cluster, but rather found the mean mass of a larger cluster sample. Meanwhile, Wen et al. (2009) did a study of the larger cluster structure that SDSS J1226+2152 is a part of. For this cluster, we can therefore not compare our mass estimates with previous studies.

For SDSS J1723+3411, the Einstein radius is larger than the one found by Kubo et al. (2010). There is a bright arc at their Einstein radius, $\theta_{\rm E}^{\rm K10} = 4.7''$ (note that the value depends on the redshift of the arc), but there is also a fainter arc at $\theta_{\rm E} = 9.087''$, seen clearer with an infrared filter (see Figure 1.4). They performed a strong lensing analysis, and found the enclosed mass to be $M^{\rm K10}(\theta_{\rm E}) = (3.5 \pm 0.5) \times 10^{12}\, h^{-1} M_\odot$. As they do not state if this mass is 2D or 3D, we assume it to be 2D. We extrapolate this value out to r_1 while assuming a SIS profile, $M^{\rm K10}(r_1) = 1.370^{+0.196}_{-0.196} \times 10^{13}\, h^{-1} M_\odot$. We use a SIS profile, because, at this radius, its behavior should be similar to the NFW profile. The ratios are $M^{14}_{NFW}/M^{\rm K10} = 0.617^{+0.878}_{-0.351}$, and $M^{15}_{NFW}/M^{\rm K10} = 0.589^{+0.877}_{-0.362}$ for a NFW profile. We see that our mass estimates is about 0.6 times that found by Kubo et al..

In the case of a SIS profile, the ratios are $M_\chi/M^{\rm K10} = 1.663^{+2.691}_{-0.854}$, and $M_\kappa/M^{\rm K10} = 1.726^{+3.084}_{-0.708}$. This indicates that the mass we found, is around 1.7 times that found by Kubo et al. (2010). For both the NFW profile, and the SIS profile, we find that the error estimates are quite large.

Dahle et al. (2016) have done a strong lensing analysis of PSZ1 G311.65–18.48. They found the same Einstein radius as us, and that the 2D enclosed mass at $r_E = 0.169 \pm 0.025$ Mpc, is $M^{\rm D16}(\theta_{\rm E}) = 1.8^{+0.6}_{-0.5} \times 10^{14} M_\odot$, with $h = 0.7$. Again, we extrapolate this mass out to r_1 for this cluster, while assuming a SIS profile. The mass is then $M^D(r_1) = 2.048^{+0.331}_{-0.312} \times 10^{14}\, M_\odot$. The ratios become, $M^{\rm fix}_{\rm NFW}/M^{\rm D16} = 0.527^{+0.726}_{-0.395}$ for F606W, and $M^{\rm fix}_{\rm NFW}/M^{\rm D16} = 0.504^{+0.665}_{-0.379}$ for F814W. In both cases, our mass is almost half the value found by Dahle et al.. When using the SIS model, $M^{\rm fix}_\chi/M^{\rm D16} = 1.747^{+2.329}_{-1.301}$ and $M^{\rm fix}_\kappa/M^{\rm D16} = 1.452^{+1.996}_{-1.044}$ for F606W, and $M^{\rm fix}_\chi/M^{\rm D16} = 1.570^{+1.987}_{-1.251}$ and $M^{\rm fix}_\kappa/M^{\rm D16} = 1.452^{+1.996}_{-1.044}$ and for F814W. This discrepancy between what has been previously found, and our estimates, might be partially due to us assuming a SIS model when extrapolating, as a NFW profile seem to fit our data the best. As found in Section 3.2.1, there is a difference between these two models, when just doing a fitting to our own data. However, we note again, that the errors are quite significant.

3.3 Future studies

Any future analyses of these clusters, would benefit from getting better constraints on the concentration parameter, c_{200}. As seen in our results, it varies wildly for the same cluster, just depending on the filter applied to the image, and with large margins

of error. Weak lensing studies at larger radii, would reduce the uncertainty in c_{200}. Both SDSS J1226+2152, and SDSS J1723+3411 are candidates up for imaging with the James Webb Space Telescope. Its considerably larger field of view, compared to the Hubble, should be able to help providing these constraints.

For the cluster SDSS J1723+3411, we only use one one image, with filter F775W. Getting additional deep exposures in other filters, would help decrease the risk of our shear measurements being contaminated by the cluster galaxies.

Chapter 4

Conclusion

In this thesis, we have performed a weak lensing analysis on three separate galaxy clusters. These are PSZ1 G311.65–18.48, SDSS J1226+2152, and SDSS J1723+3411. They were imaged by two different wide-field cameras onboard the Hubble Space Telescope; the wide-field channel of ACS, and the UVIS channel of WFC3. For PSZ1 G311.65–18.48, and SDSS J1226+2152, we had one image, combined from multiple exposures, each in two filters, the F606W filter, and the F814W filter. For the cluster SDSS J1723+3411, we had one image, combined from multiple exposures, in the F775W filter.

We measured the reduced shear in the fields of our clusters, by using the KSB method with corrections (Kaiser et al. 1995; Luppino and Kaiser 1997; Hoekstra et al. 1998). We then fitted the data to two different density profiles, the NFW, and the SIS, by minimizing the χ^2-statistic.

We found that the velocity dispersion of the PSZ cluster, was around the value we would expect from a rich cluster, from $1010.7^{+36.1}_{-38.2}\,\mathrm{km\,s^{-1}}$ to $1066.4^{+67.2}_{-74.7}\,\mathrm{km\,s^{-1}}$.

For SDSS J1723+3411 the velocity dispersion was $518.9^{+92.2}_{-121.4}\,\mathrm{km\,s^{-1}}$, which is very close to the value found in the strong lensing analysis done by Kubo et al. (2010), on the same cluster.

For the last cluster, SDSS J1226+2152, σ_v was very small, in the range of $\sigma_v = 301.2^{+163.4}_{-300.2} - 323.0^{+158.0}_{-322.0}\,\mathrm{km\,s^{-1}}$. This value, together with the large error estimates, was most likely due to contamination of the shear measurements, from the larger surrounding structure that this cluster is a part of. Hence, the curve of the measured and calculated mean reduced shear, $\langle g \rangle$, as a function of radius, r, stayed quite flat, when we would normally expect it to fall with increasing radii. Our obtained σ_v value, did not fit with the one found by Bayliss et al. (2011). This is, perhaps, not unexpected, considering Bayliss et al. found their σ_v value through a spectroscopic study of the velocities of the cluster galaxies, and not through a gravitational lensing analysis. Our obtained mass, is therefore also small.

When fitting the NFW model to our data, the concentration parameter, c_{200} varied greatly between filters of the same cluster. As the size of our fields are not that large, we did not expect to be able to estimate c_{200}, with any great precision. The joint

confidence intervals of r_{200}, and c_{200}, supported this, as a wide range of c_{200} values, from > 0.1 to $24 <$, could fit within 1σ confidence. We therefore also did an analysis for a fixed concentration parameter, using the $c - M$ relation found by Duffy et al. (2008). For the PSZ cluster, we found that $c_{200} = 2.8 - 3.1$. The mass then became $M_{200} \approx 1.1 \times 10^{15}\, h^{-1} M_{\odot}$, making this a rich cluster.

In the case of the two SDSS clusters, the best-fit c_{200} was found to be unrealistically small. We therefore did two additional analyses for these two clusters, where c_{200} was calculated from $M_{200} = 10^{14}\, h^{-1} M_{\odot}$ and $M_{200} = 10^{15}\, h^{-1} M_{\odot}$. We ended up with $c = 3.5$, and $c = 2.9$, respectively, for both clusters. This way, we obtain a maximum upper and lower bound estimate of r_{200}, and M_{200}.

For SDSS J1226+2152, the upper and lower bound mass estimates, were $M_{200} = 1.185^{+0.730}_{-0.185} - 0.201^{+0.804}_{-0.201} \times 10^{14}\, h^{-1} M_{\odot}$, for $c_{200} = 2.9$, and $M_{200} = 0.201^{+0.551}_{-0.198} - 0.217^{+0.573}_{-0.214} \times 10^{14}\, h^{-1} M_{\odot}$, for $c_{200} = 3.5$. These masses were lower than what we would usually expect, and the uncertainties in the measurements were also large. This was most likely due to the larger structure surrounding the cluster, biasing the gravitational shear towards lower values, and making it so that the mass density profile, is not entirely spherical.

For SDSS J1723+3411 the upper and lower bound mass estimates, were $M_{200} = 2.435^{+1.725}_{-1.272} \times 10^{14}\, h^{-1} M_{\odot}$, for $c_{200} = 2.9$, and $M_{200} = 2.039^{+1.033}_{-1.158} \times 10^{14}\, h^{-1} M_{\odot}$, for $c_{200} = 3.5$. Despite these masses being of the expected order, the minimum χ^2, was the largest out of all our clusters. We could only divide our field into three annuli, which might be the reason for the poor fit.

By comparing the measured shear with the shear calculated from the NFW and SIS model, we found that the NFW model proved the better fit, for all of our clusters. However, at these radii, the two profiles behave very similarly, $\rho \propto r^{-2}$. This was mirrored in our comparison of the mass estimates from the two models: While the SIS model gave a higher best-fit mass, both models lie within each others margins of error. We conclude that the NFW model provides the best estimate to the "true" mass of the cluster. For the best-fit mass estimates, the NFW profile mass, were approximately 0.4 to 0.3 times the SIS profile mass estimates.

All three clusters display luminous arcs around their cores. They have all been subjected to a strong lensing analysis in the past, but only PSZ1 G311.65–18.48 (Dahle et al. 2016), and SDSS J1723+3411 (Kubo et al. 2010), had had an individual mass estimated at their Einstein radius, θ_{E}. While assuming a SIS profile, we extrapolated these measurements to a larger radius r_1, which vary depending on the cluster, for a comparison. Our obtained mass estimates were smaller than what was found by Dahle et al. (2016) and Kubo et al. (2010), when we use the mass calculated from a NFW profile. Our mass estimates were generally larger than theirs, when we assumed a SIS profile instead. For SDSS J1723+3411, our best-fit mass was approximately 0.6 times the value found by Kubo et al., when we used our NFW profile estimates, but almost 1.7 times larger when we used a SIS profile. Similarly, for PSZ1 G311.65–18.48, our mass estimates where approximately 0.5, and 1.5 times the mass found by Dahle et al., for a NFW and SIS profile, respectively. However, the estimated errors were large, so

there may well be overlap between *our* mass values, and those found by Dahle et al., and Kubo et al..

Bibliography

Abell, G. O. (1958). The Distribution of Rich Clusters of Galaxies. *Astrophysical Journal, Supplement*, 3:211.

Abell, G. O., Corwin, Jr., H. G., and Olowin, R. P. (1989). A catalog of rich clusters of galaxies. *Astrophysical Journal, Supplement*, 70:1–138.

Alcock, C., Akerlof, C. W., Allsman, R. A., et al. (1993). Possible gravitational microlensing of a star in the Large Magellanic Cloud. *Nature*, 365(6447):621.

Andernach, H. and Zwicky, F. (2017). English and Spanish Translation of Zwicky's (1933) The Redshift of Extragalactic Nebulae. *arXiv:1711.01693 [astro-ph]*. arXiv: 1711.01693.

Bartelmann, M. and Maturi, M. (2017). Weak gravitational lensing. *Scholarpedia*, 12(1):32440.

Bartelmann, M. and Schneider, P. (2001). Weak gravitational lensing. *Physics Reports*, 340(4):291–472.

Bayliss, M. B., Hennawi, J. F., Gladders, M. D., et al. (2011). Gemini/GMOS Spectroscopy of 26 Strong-lensing-selected Galaxy Cluster Cores. *Astrophysical Journal, Supplement*, 193:8.

Bharadwaj, S., Bhavsar, S. P., and Sheth, J. V. (2004). The Size of the Longest Filaments in the Universe. *The Astrophysical Journal*, 606(1):25–31.

Bhattacharya, S., Habib, S., Heitmann, K., and Vikhlinin, A. (2013). Dark Matter Halo Profiles Of Massive Clusters: Theory Versus Observations. *The Astrophysical Journal*, 766(1):32.

Bullock, J. S., Kolatt, T. S., Sigad, Y., et al. (2001). Profiles of dark haloes: evolution, scatter and environment. *Monthly Notices of the RAS*, 321:559–575.

Carlstrom, J. E., Joy, M. K., Grego, L., et al. (2000). Imaging the Sunyae-Zel'dovich Effect. *Physica Scripta*, T85(1):148.

Cavendish, H. (1731-1810/1921). To find the bending of a ray of light wich passes near the surface of any body by the attraction of that body. In Thorpe, E., editor,

The scientific papers of the Honourable Henry Cavendish, FRS, volume II, page 437. Cambridge University Press. Original work written 1731-1810.

Chwolson, O. (1924). Über eine mögliche Form fiktiver Doppelsterne. *Astronomische Nachrichten*, 221:329.

Dahle, H., Aghanim, N., Guennou, L., et al. (2016). Discovery of an exceptionally bright giant arc at z = 2.369, gravitationally lensed by the planck cluster psz11.65-18.48. *A&A*, 590:L4.

Deguchi, S. and Watson, W. D. (1986). Wave effects in gravitational lensing of electromagnetic radiation. *Physical Review D*, 34:1708–1718.

Dressel, L. et al. (2019). *Wide Field Camera 3 Instrument Handbook*. STScI, Baltimore, 11.0 edition.

Duffy, A. R., Schaye, J., Kay, S. T., and Dalla Vecchia, C. (2008). Dark matter halo concentrations in the Wilkinson Microwave Anisotropy Probe year 5 cosmology. *Monthly Notices of the Royal Astronomical Society: Letters*, 390(1):L64–L68.

Dyson, F. W., Eddington, A. S., and Davidson, C. (1920). A Determination of the Deflection of Light by the Sun's Gravitational Field, from Observations Made at the Total Eclipse of May 29, 1919. *Philosophical Transactions of the Royal Society of London Series A*, 220:291–333.

Eddington, A. S. (1921). Chapter 8: Other tests of the theory. In *Space, Time, and Gravitation*, pages 133–135. The University Press.

Einstein, A. (1911/1993). On the Influence of Gravitation on the Propagation of Light. In *The Collected Papers of Albert Einstein, Volume 3 (English) The Swiss Years: Writings, 1909-1911*, pages 379–387. Princeton University Press, Princeton, New Jersey. Original work published 1911.

Einstein, A. (1936). Lens-Like Action of a Star by the Deviation of Light in the Gravitational Field. *Science*, 84(2188):506–507.

Espenak, F. and Meeus, J. (2006). NASA Technical Publication, TP-2006-214141.

Fahlman, G., Kaiser, N., Squires, G., and Woods, D. (1994). Dark matter in MS 1224 from distortion of background galaxies. *The Astrophysical Journal*, 437:56–62.

Fruchter, A. S. and Hook, R. N. (2002). Drizzle: A method for the linear reconstruction of undersampled images. *Publications of the Astronomical Society of the Pacific*, 114(792):144–152.

Garner, R. (2015a). Hubble Servicing Missions Overview.

Garner, R. (2015b). Observatory.

Garner, R. (2016). Hubble Space Telescope – Advanced Camera for Surveys.

Garner, R. (2017a). Highlights of Hubble's Exploration of the Universe.

Garner, R. (2017b). Hubble Space Telescope – Wide Field Camera 3.

Gennaro, M. et al. (2018). Chapter 2: WFC3 Data Structure. In *WFC3 Data Handbook*, pages 7–9. STScI, Baltimore, 4.0 edition.

Gentile, M., Courbin, F., and Meylan, G. (2012). Interpolating point spread function anisotropy. *Astronomy and Astrophysics*, 549.

Gorenstein, M. V., Falco, E. E., and Shapiro, I. I. (1988). Degeneracies in parameter estimates for models of gravitational lens systems. *The Astrophysical Journal*, 327:693–711.

Greenfield, P. E., Burke, B. F., and Roberts, D. H. (1980a). The double quasar 0957+561 as a gravitational lens: further VLA observations. *Nature*, 286(5776):865–866.

Greenfield, P. E., Roberts, D. H., and Burke, B. F. (1980b). The Double Quasar 0957+561: Examination of the Gravitational Lens Hypothesis Using the Very Large Array. *Science*, 208(4443):495–497.

Hewitt, J. N., Turner, E. L., Schneider, D. P., et al. (1988). Unusual radio source MG1131+0456: a possible Einstein ring. *Nature*, 333(6173):537–540.

Heymans, C., Van Waerbeke, L., Bacon, D., et al. (2006). The Shear Testing Programme - I. Weak lensing analysis of simulated ground-based observations. *Monthly Notices of the Royal Astronomical Society*, 368(3):1323–1339.

Hille, K. (2018). The Hubble Story.

Hoekstra, H., Bartelmann, M., Dahle, H., et al. (2013). Masses of Galaxy Clusters from Gravitational Lensing. *Space Science Reviews*, 177:75–118.

Hoekstra, H., Franx, M., Kuijken, K., and Squires, G. (1998). Weak Lensing Analysis of CL 1358+62 Using Hubble Space Telescope Observations. *The Astrophysical Journal*, 504(2):636–660.

Hubble, E. (1929). A Relation between Distance and Radial Velocity among Extra-Galactic Nebulae. *Proceedings of the National Academy of Science*, 15:168–173.

Huchra, J., Gorenstein, M., Kent, S., et al. (1985). 2237 + 0305: A new and unusual gravitational lens. *The Astronomical Journal*, 90:691–696.

Jaki, S. L. (1978). Johann Georg von Soldner and the gravitational bending of light, with an English translation of his essay on it published in 1801. *Foundations of Physics*, 8(11):927–950.

Jing, Y. P. and Suto, Y. (2000). The density profiles of the dark matter halo are not universal. *The Astrophysical Journal*, 529(2):L69–L72.

Kaiser, N., Squires, G., and Broadhurst, T. (1995). A Method for Weak Lensing Observations. *The Astrophysical Journal*, 449:460.

Kaiser, N., Squires, G., Fahlman, G., and Woods, D. (1994). Mapping the dark matter in clusters. (I). In Durret, F., Mazure, A., and Tran Thanh Van, J., editors, *Clusters of Galaxies*, volume 14, page 269.

King, L., Clowe, D., and De Lucia, G. (2004). Effects of asphericity and substructure on the determination of cluster mass with weak gravitational lensing. *Monthly Notices of the Royal Astronomical Society*, 350(3):1038–1048.

Klimov, Y. G. (1963). The Use in Extragalactic Astronomy of the Deviation of Light Rays in Galactic Gravitational Fields. *Soviet Physics Doklady*, 8:431.

Kneib, J.-P., Ellis, R. S., Smail, I., Couch, W. J., and Sharples, R. M. (1996). Hubble Space Telescope Observations of the Lensing Cluster Abell 2218. *The Astrophysical Journal*, 471(2):643.

Kneib, J.-P. and Natarajan, P. (2011). Cluster lenses. *Astronomy and Astrophysics Review*, 19:47.

Kubo, J. M., Allam, S. S., Drabek, E., et al. (2010). The Sloan Bright Arcs Survey: Discovery of Seven New Strongly Lensed Galaxies from z = 0.66-2.94. *Astrophysical Journal, Letters*, 724:L137–L142.

Liebes, S. (1964). Gravitational Lenses. *Phys. Rev.*, 133:B835–B844.

Lucas, R. A., Desjardins, T., et al. (2018). Chapter 3: ACS Calibration Pipeline. In *ACS Data Handbook*, pages 40–45. STScI, Baltimore, 9.0 edition.

Luppino, G. A. and Kaiser, N. (1997). Detection of Weak Lensing by a Cluster of Galaxies at z = 0.83. *The Astrophysical Journal*, 475(1):20.

Lynds, R. and Petrosian, V. (1989). Luminous Arcs in Clusters of Galaxies. *The Astrophysical Journal*, 336:1.

Marriage, T. A., Acquaviva, V., Ade, P. A. R., et al. (2011). The Atacama Cosmology Telescope: Sunyaev-Zel'dovich-Selected Galaxy Clusters at 148 GHz in the 2008 Survey. *Astrophysical Journal*, 737:61.

Misner, C. W., Thorne, K. S., and Wheeler, J. A. (2017). *Gravitation*. Princeton University Press. Google-Books-ID: zAAuDwAAQBAJ.

Narayan, R. and Bartelmann, M. (1996). Lectures on Gravitational Lensing. *arXiv:astro-ph/9606001*. arXiv: astro-ph/9606001.

Navarro, J. F., Frenk, C. S., and White, S. D. M. (1997). A Universal Density Profile from Hierarchical Clustering. *The Astrophysical Journal*, 490(2):493–508. arXiv: astro-ph/9611107.

Paczynski, B. (1987). Giant luminous arcs discovered in two clusters of galaxies. *Nature*, 325(6105):572–573.

Pen, U.-L. (1999). Analytical Fit to the Luminosity Distance for Flat Cosmologies with a Cosmological Constant. *The Astrophysical Journal Supplement Series*, 120:49–50.

Planck Collaboration, Ade, P. A. R., Aghanim, N., et al. (2014). Planck 2013 results. XXIX. The Planck catalogue of Sunyaev-Zeldovich sources. *Astronomy and Astrophysics*, 571:A29.

Refsdal, S. (1964a). The gravitational lens effect. *Monthly Notices of the Royal Astronomical Society*, 128:295.

Refsdal, S. (1964b). On the possibility of determining Hubble's parameter and the masses of galaxies from the gravitational lens effect. *Monthly Notices of the Royal Astronomical Society*, 128:307.

Renn, J., Sauer, T., and Stachel, J. (1997). The Origin of Gravitational Lensing: A Postscript to Einstein's 1936 Science Paper. *Science*, 275(5297):184–186.

Rivera-Thorsen, T. E., Dahle, H., Chisholm, J., et al. (2019). Hubble captures multiply-imaged ionizing radiation from strongly lensed galaxy at z=2.4. *arXiv e-prints*, page arXiv:1904.08186.

Ryon, J. E. et al. (2019). *ACS Instrument Handbook*. STScI, Baltimore, 18.0 edition.

Sauer, T. (2008). Nova Geminorum 1912 and the origin of the idea of gravitational lensing. *Archive for History of Exact Sciences*, 62(1):1–22.

Schneider, P. (2006). Introduction to Gravitational Lensing and Cosmology. In Schneider, P., Kochanek, C. S., and Wambsganss, J., editors, *Gravitational Lensing: Strong, Weak and Micro*, Saas-Fee Advanced Courses, pages 1–89. Springer Berlin Heidelberg, Berlin, Heidelberg.

Shapiro, I. I. (1964). Fourth Test of General Relativity. *Phys. Rev. Lett.*, 13:789–791.

Soucail, G., Fort, B., Mellier, Y., and Picat, J. P. (1987). A blue ring-like structure in the center of the A 370 cluster of galaxies. *Astronomy and Astrophysics*, 172:L14.

SpaceTelescope (n.d). Hubble's Instruments: WFC3 - Wide Field Camera 3.

Stockton, A. (1980). The lens galaxy of the twin QSO 0957+561. *The Astrophysical Journal Letters*, 242:L141–L144.

Sunyaev, R. A. and Zeldovich, Y. B. (1972). The Observations of Relic Radiation as a Test of the Nature of X-Ray Radiation from the Clusters of Galaxies. *Comments on Astrophysics and Space Physics*, 4:173.

Tabbert, B. and Goushcha, A. (2012). Optical Detectors. In Träger, F., editor, *Springer Handbook of Lasers and Optics*, pages 543–619. Springer Berlin Heidelberg, Berlin, Heidelberg.

Tantau, T. (2019). *The TikZ and PGF Packages*.

Tozer, E. P. J. (2012). 3.3 Optical sensors. In *Broadcast Engineer's Reference Book*, page 422. CRC Press. Google-Books-ID: 8YDOAwAAQBAJ.

Tyson, J. A., Valdes, F., and Wenk, R. A. (1990). Detection of systematic gravitational lens galaxy image alignments - Mapping dark matter in galaxy clusters. *The Astrophysical Journal Letters*, 349:L1–L4.

Udalski, A., Jaroszyński, M., Paczyński, B., et al. (2005). A Jovian-Mass Planet in Microlensing Event OGLE-2005-BLG-071. *The Astrophysical Journal*, 628(2):L109–L112.

Valls-Gabaud, D. (2006). The conceptual origins of gravitational lensing. In Alimi, J.-M. and Füzfa, A., editors, *Albert Einstein Century International Conference*, volume 861 of *American Institute of Physics Conference Series*, pages 1163–1163.

Walsh, D., Carswell, R. F., and Weymann, R. J. (1979). 0957 + 561 A, B: twin quasistellar objects or gravitational lens? *Nature*, 279(5712):381–384.

Web of Science (2018). Web of Science [v.5.30] - Web of Science Core Collection Result Analysis.

Wen, Z. L., Han, J. L., and Liu, F. S. (2012). A CATALOG OF 132,684 CLUSTERS OF GALAXIES IDENTIFIED FROM SLOAN DIGITAL SKY SURVEY III. *The Astrophysical Journal Supplement Series*, 199(2):34.

Wen, Z.-L., Han, J.-L., Xu, X.-Y., et al. (2009). Discovery of four gravitational lensing systems by clusters in the SDSS DR6. *Research in Astronomy and Astrophysics*, 9(1):5–10.

Weymann, R. J., Latham, D., Angel, J. R. P., et al. (1980). The triple QSO PG1115 + 08: another probable gravitational lens. *Nature*, 285(5767):641–643.

Wilson, G., Kaiser, N., and Luppino, G. A. (2001). Mass and light in the universe. *The Astrophysical Journal*, 556(2):601–618.

Wold, M., Lacy, M., Dahle, H., Lilje, P. B., and Ridgway, S. E. (2002). AGN-selected clusters as revealed by weak lensing. *Monthly Notices of the Royal Astronomical Society*, 335(4):1017–1036.

Wright, C. O. and Brainerd, T. G. (2000). Gravitational Lensing by NFW Halos. *The Astrophysical Journal*, 534(1):34–40.

Young, P., Gunn, J. E., Kristian, J., Oke, J. B., and Westphal, J. A. (1980). The double quasar Q0957 + 561 A, B - A gravitational lens image formed by a galaxy at Z = 0.39. *The Astrophysical Journal*, 241:507–520.

Zwicky, F. (1937a). Nebulae as Gravitational Lenses. *Phys. Rev.*, 51:290–290.

Zwicky, F. (1937b). On the Probability of Detecting Nebulae Which Act as Gravitational Lenses. *Phys. Rev.*, 51:679–679.